OBSERVATIONAL AND NUMERICAL STUDY OF ATLANTIC TROPICAL INSTABILITY WAVES

A Dissertation

by

QIAOYAN WU

Submitted to the Office of Graduate Studies of
Texas A&M University
in partial fulfillment of the requirements for the degree of

DOCTOR OF PHILOSOPHY

August 2007

Major Subject: Atmospheric Sciences

OBSERVATIONAL AND NUMERICAL STUDY OF ATLANTIC TROPICAL INSTABILITY WAVES

A Dissertation

by

QIAOYAN WU

Submitted to the Office of Graduate Studies of
Texas A&M University
in partial fulfillment of the requirements for the degree of

DOCTOR OF PHILOSOPHY

Approved by:

Chair of Committee,	Kenneth P. Bowman
Committee Members,	Gerald R. North
	Courtney Schumacher
	Ping Chang
	Marc Genton
Head of Department,	Richard Orville

August 2007

Major Subject: Atmospheric Sciences

ABSTRACT

Observational and Numerical Study of Atlantic Tropical
Instability Waves . (August 2007)
Qiaoyan Wu, B.S., Nanjing University, China;
M.S., Texas A&M University
Chair of Advisory Committee: Dr. Kenneth P. Bowman

This study uses high resolution satellite measurements from the Tropical Rainfall Measuring Mission (TRMM), Quick Scatterometer (QuikSCAT) and Special Sensor Microwave Imager (SSM/I) to investigate the variability of sea surface temperature (SST), surface wind velocity, water vapor, cloud liquid water and precipitation associated with westward moving tropical instability waves (TIWs) in the Atlantic Ocean from 1998 to 2005. On interannual scales, TIWs in the Pacific Ocean are strongest during the cold phase of El Niño Southern Oscillation (ENSO), when the cold tongue is most pronounced. The waves are weak during the warm phase of ENSO. A low-frequency Atlantic air-sea coupled mode influences the TIW activity in the Atlantic Ocean as ENSO does in the Pacific Ocean. The characteristics of TIWs are largely associated with the background oceanographic states.

Coherent ocean-atmosphere patterns are shown in the Atlantic Ocean during eight years. Southeasterly trades strengthen and water vapor increases over warm SST anomalies associated with TIWs. The opposite is true over cold TIW SST anomalies. The cloud liquid water and rain response to the SST follows a very similar pattern, appearing to be roughly in phase with wind convergence and divergence in the central tropical Atlantic. The atmospheric response to the TIW SST anomalies extends north of the TIW active region, suggesting a remote response to the TIWs. The atmospheric response to the Atlantic TIWs shows interannual variability. In 1999, the rainfall response to the TIW SST anomalies

is much larger than in other years, which is due to the southward movement of Atlantic ITCZ (Intertropical Convergence Zone). When the Atlantic ITCZ moves south, it is more susceptible to TIW influence.

One regional climate model and one global climate model are applied to study the mechanism of atmospheric response to the Atlantic TIWs with daily TMI satellite SST forcing. Both models successfully simulated the wind velocity, wind convergence and precipitation as observed. While the satellite observations support the vertical mixing mechanism for the surface wind response to TIWs, both models show the pressure gradient mechanism is dominant in the Atlantic.

ACKNOWLEDGMENTS

In completing this dissertation, there are many people to whom I must give acknowledgment. First of all, I would like to thank my committee chair Dr. Kenneth P. Bowman for his extraordinary support during my PhD study. His patience and responsible attitude towards scientific research have impressed me and benefited me a lot. Dr. Gerald R. North directed me through my first two years at TAMU. Dr. North is not only a great advisor for academics but also a great advisor for life. Both of them have enormous influence on me and help to make me what I am today. Special thanks go to my committee member Ping Chang. Without his perceptive insight into the topic of this project, this dissertation might never have come into being. My committee members, Dr. Courtney Schumacher and Dr. Marc Genton also offered generous help and advice to me.

I owe an intellectual debt to Jen-Shan Hsieh in Oceanography Department and my colleague, Salil Mahajan, for this dissertation. The MM5 model data came from Dr. Hsieh's simulation. Salil Mahajan helped me with the CAM model simulation. Salil Mahajan also helped me to learn how to run CAM simulation. Dr. R. Saravanan also has been an incredible help to me.

Finally, I want to thank my parents and my brother for their understanding and support in my PhD study.

TABLE OF CONTENTS

CHAPTER Page

LIST OF TABLES

LIST OF FIGURES

FIGURE Page

FIGURE Page

FIGURE Page

CHAPTER I

INTRODUCTION

Tropical instability waves (TIWs) appear in the tropical Pacific and Atlantic oceans as westward-propagating oscillations of the temperature front between cold upwelling equatorial water and warmer water to the north (Legeckis 1977; Düing et al. 1975, see Figure 1) . The existence of TIWs is generally attributed to the instability of meridional shears associated with the equatorial undercurrent (EUC), south equatorial current (SEC) and north equatorial countercurrent (NECC) and density gradients between the equatorial cold tongue and warm water north of it (Philander 1978; Cox 1980).

While TIWs have oceanic origin, several recent studies have presented evidence that the SST variations associated with TIWs can induce atmospheric variability. Halpern et al. (1988) first indicated a possible relationship between surface wind and SST. Hayes et al. (1989) also found a significant correlation between wind speeds and SST perturbations associated with TIWs from an array of moored sensors. Xie et al. (1998) used satellite data to show that TIW SST variations induce wind perturbations. They further noted that the southeasterly trade winds are enhanced over the warm SST anomalies and reduced over the colder anomalies when the data are filtered to isolate TIW variability. Using satellite observations of visible cloudiness and SST, Deser et al. (1993) found strong association between visible cloud and the SST waves, with enhanced cloudiness in the warm troughs of the waves and reduced cloudiness in the cold crests of the waves. Using high-resolution satellite data from the Tropical Rainfall Measuring Mission (TRMM) and Quick Scatterometer (QuikSCAT) from 1999, Hashizume et al. (2001) analyzed the co-variability of SST, surface wind velocity, column-integrated water vapor, cloud liquid water and precipitation

---

The format and style follow that of *Journal of Climate*.

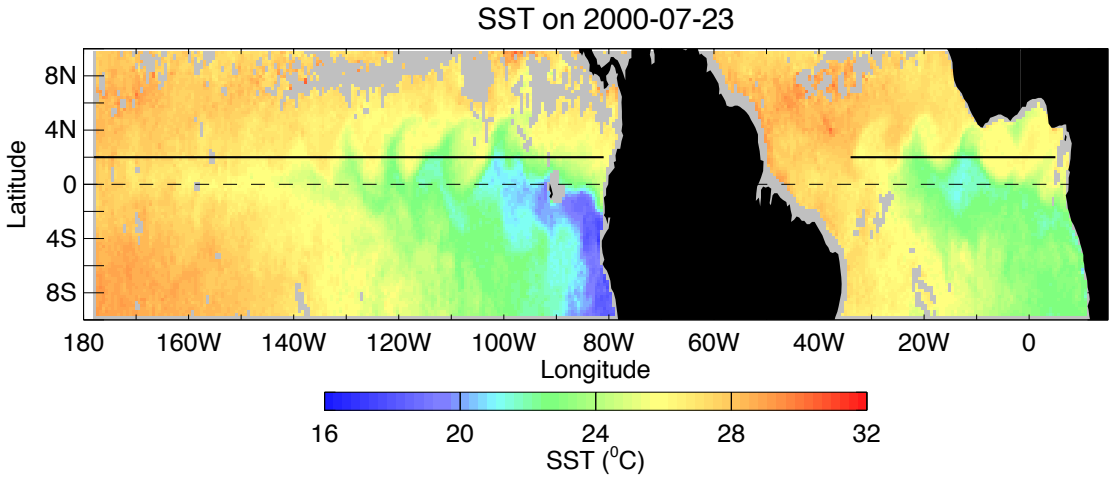

Fig. 1. TIWs as seen in TMI SST for a 3-day period ending on 2000-07-23. The grey spots in the ocean represent missing TMI SST data. The heavy lines at 2°N represent the location chosen for longitude-time plots in the Pacific and Atlantic Oceans.

associated with TIWs. The association of clouds and rain with TIWs indicates that the atmospheric response is not limited to the surface, but extends at least through the boundary layer.

TIWs induce wind changes by boundary layer mechanisms operating over comparatively cold ocean surface. The atmosphere's thermal feedback to the ocean can affect the stability of the atmospheric boundary layer (Hayes et al. 1989), the distribution of cloudiness (Deser et al. 1993) and the latent heat flux (Zhang and McPhaden 1995). TIWs are an important aspect of equatorial ocean dynamics and thermodynamics, as TIWs transport a substantial amount of heat and momentum across the equatorial front (Hansen and Paul 1984; Baturin and Niiler 1997; Bryden and Brady 1989; Wang and McPhaden 1999). Thus, this TIW-induced ocean-atmosphere interaction could have an effect on the tropical climate (Xie et al. 1998).

Until the late 1990s only limited in situ and satellite data were available to study the co-

variability of SST and wind. The new generation of satellites observing the tropical oceans contributed greatly to an improved understanding of coupled ocean-atmosphere variability in the Tropics. The SeaWinds scatterometer on the National Aeronautics and Space Administor's Quick Scatterrometer (QuikSCAT) satellite, launched in 1999, provides nearly global daily surface wind fields. The TRMM Microwave Imager (TMI) gives global tropical rainfall measurements and at the same time offers a tropical SST field on a daily basis that is nearly free of cloud contamination (Wentz et al. 2000; Chelton et al. 2000a). With these high-resolution products, Liu et al. (2000) and Hashizume et al. (2001) confirmed the finding of Xie et al. (1998). Hashizume et al. (2001) further show that significant variability of wind, water vapor, cloud liquid water, and precipitation can be observed in the Intertropical Convergence Zone (ITCZ), which is rather distant from the TIW region. They hypothesize that TIWs can have a remote influence on the ITCZ.

Numerical modeling studies have proven to be very useful for understanding physical mechanisms governing tropical ocean-atmosphere feedbacks. So far there have been few numerical studies of the planetary boundary layer (PBL) response to TIW-induced SST variation. Xie et al. (1998) used a global general circulation model to investigate the physical processes that occur in the atmospheric response to SST driving in the Tropical Pacific. Small et al. (2003) used a high-resolution regional model climate model to study the PBL response to SST variations in the tropical Pacific cold region. To our knowledge, there are no numerical studies of atmospheric PBL response to TIW-induced SST variations in the Tropical Atlantic. Compared with the tropical Pacific, our current understanding of atmosphere-ocean feedback mechanisms in the tropical Atlantic is still in its early stages.

It is critical that we develop a more comprehensive understanding of the underlying physics involved in regional atmosphere-ocean feedbacks in Atlantic Ocean because of its potential importance for climate. A Regional Climate Model (RegCM) with detailed physical processes and complex topography and a General Circulation Model (GCM) with

coarse spatial and temporal resolutions are used in this dissertation to study the atmosphere PBL response to TIW-induced SST fluctuations in the tropical Atlantic. Combined with available satellite observation data, these models are used to explore key physical processes that contribute to regional feedbacks.

CHAPTER II

BACKGROUND

A. Genesis and Effect

Early analytical studies by Philander (1976, 1978) demonstrated that oscillations with characteristics similar to the observed TIWs derive their energy through barotropic instability arising from the latitudinal shear between the South Equatorial Current (SEC) and North Equatorial Countercurrent (NECC). The SEC, NECC and Equatorial Undercurrent (EUC) distributions are shown in Figure 2. A series of idealized numerical studies corroborate these findings. Cox (1980) confirmed that barotropic instability is the primary source of energy of the TIWs, but that the unstable meridional shear is between EUC and the northern branch of the SEC. The energy analysis also indicates that baroclinic instability represents an important energy contribution to the growth of the oscillations. Proehl (1996) showed that the instabilities draw their energy through amixture of baroclinic, barotropic and Kelvin-Helmhotz mechanisms. With an idealized numerical model of the Pacific Ocean, Masina and Philander (1999) and Masina et al. (1999) showed that localized studies of the energy budget might be misleading , the whole equatorial domain has to be analyzed before a definite conclusion about the energy sources and sinks of the TIWs can be reached. These studies emphasized that the generation, structure and decay of TIWs depend on the particular generation region. A recent model study of Jochum et al. (2004) found that, in the Atlantic, TIWs are generated by barotropic instability of the shear between the EUC and northern SEC and make a small contribution to the heat budget of the equatorial mixed layer.

Besides these numerical studies, Qiao and Weisberg (1995) examined the energetics of the waves detected during the Tropical Instability Waves Experiment (TIWE) through

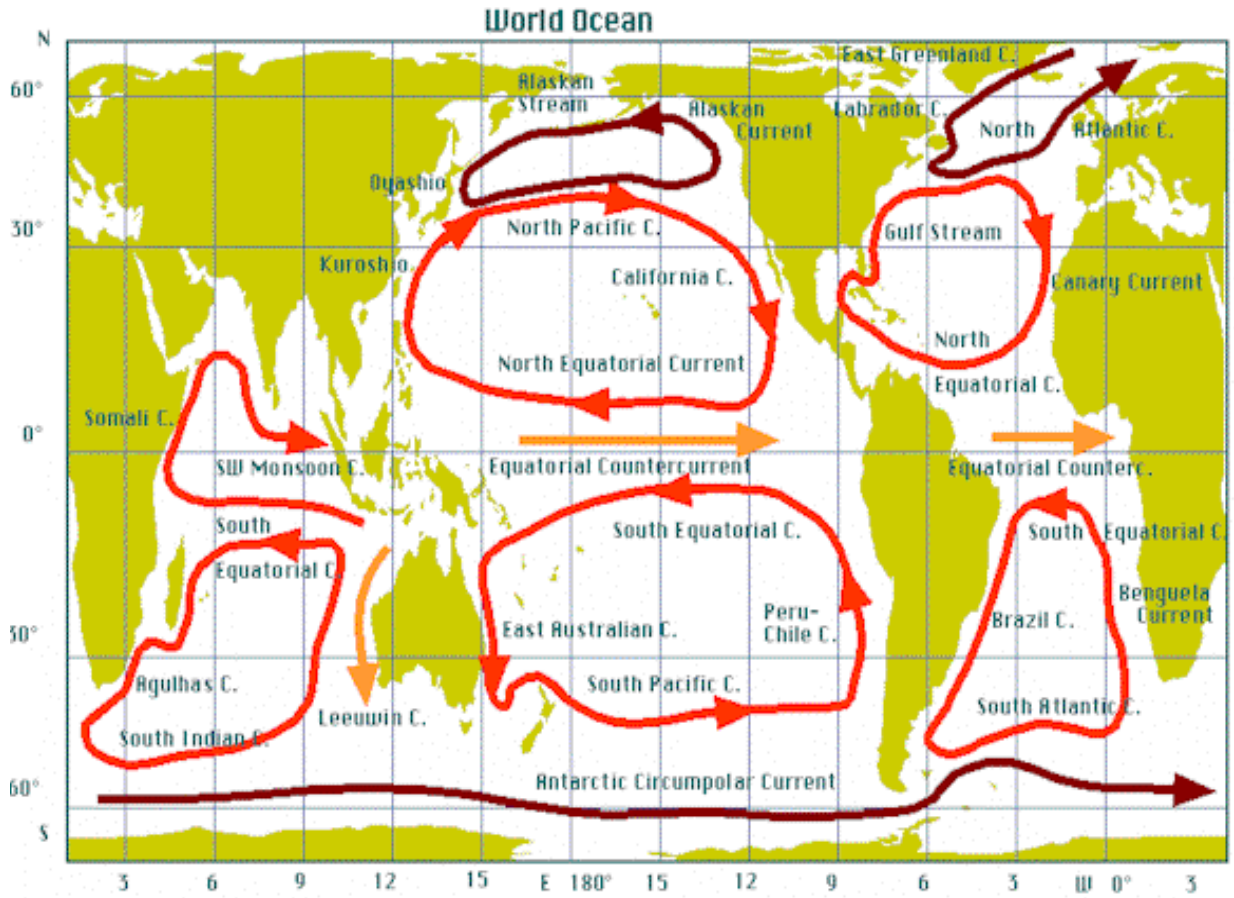

Fig. 2. Global ocean current circulations (courtesy of Matthias Tomczak).

the use of the traditional energy conversion and found that barotropic instability is the main energy source for TIWs. They showed that both the SEC and EUC are important for the waves to develop and that the baroclinic instability due to the mean meridional temperature gradient is small compared to the barotropic instability. In a case study, Grodsky et al. (2005) used temperature, salinity, velocity, and wind from a mooring at 0°N, 23°W along with satellite data for sea surface temperature and sea level to examine the contribution of TIWs to the energy and heat balance of the equatorial Atlantic mixed layer. They found that in 2002 these waves were maintained by barotropic and baroclinic conversions at comparable size.

TIWs are an important part of equatorial ocean dynamics and thermodynamics, as can be seen in their influence on mean momentum and heat balances. Lukas (1987) found the magnitude of Renolds stress due to TIWs accounts for a considerable fraction of the local wind stress. Hansen and Paul (1984) found the horizontal eddy drag of the TIWs on the SEC and NECC is the same order of magnitude as the mean trade wind stress. Weisberg and Weingartner (1988) estimated that the equatorial heat flux of TIWs in the upper 50m is approximately 100W/m^2, which is comparable to the atmospheric heat flux in the tropics. Hansen and Paul (1984) found even higher values in the Pacific. Wang and McPhaden (1999) showed that TIW-induced oceanic eddy heat flux towards the equator is comparable to the Ekman heat flux away from the equator and the large-scale net air-sea heat flux over the tropical Pacific. Thus, the TIWs could have an important influence on the phase of the seasonal cycle and the position of the equatorial cold tongue and the ITCZ. Furthermore, TIWs have an effect on equatorial Atlantic plankton and nutrient distribution, which has been observed and discussed by Menkes et al. (2002).

B. Characteristics

The characteristics of TIWs depend on the ocean basin. The typical zonal wavelength, period and phase speed of TIWs in the Atlantic are about 700-1100km, and 0.3-0.5 m/s (Jochum et al. 2004); whereas in the tropical Pacific they are about 1000km, 20-40 days and 0.5m/s (Qiao and Weisberg 1995). Another striking aspects of TIWs is their asymmetry about the equator (Qiao and Weisberg 1995). Chelton et al. (2000b) found Pacific TIWs on both the north and south sides of the equator, whereas similar phenomena are observed only on the north side of the equator in Atlantic. TIWs also have a distinctive seasonal cycle. Generally waves begin to be visible in June and decay as the next year starts.

Some studies have found that there may be more than one type of TIW. Using moored current meter data, Halpern et al. (1988) reported 20-day oscillations in the upper 100-150m of the eastern Pacific that were largely antisymmetric about the equator with a meridional structure similar to that of Yanai wave. They also found that weaker 30-50-day oscillations were present at depths below 200 m. Using profiling-current-meter data from the Hawaii-to-Tahiti Shuttle Experiment, Luther and Johnson (1990) reported three different types of instability. The first occurred during the summer and fall due to the strong horizontal shear between the EUC and the northern branch of SEC. The second occurred in the winter, and its energy was associated with the equatorial SST front located from 3°N to 6°N. The third occurred during the spring and utilized the mean potential energy associated with the thermocline tilt beneath the NECC.

C. Current Understanding of Atmosphere-Ocean Covariability

At present there are two main hypotheses concerning the relationship between SST and surface winds over the tropical oceans. According to the first hypothesis, SST affects sea level pressure, which then changes the surface wind (Lindzen and Nigam 1987, hereafter

LN). Lindzen and Nigam (1987) postulate that SST-induced air temperature anomalies can change the sea level pressure (SLP) by changing the hydrostatic balance. Pressure gradients lead to low-level convergence over warm SST and divergence over cold SST. The mechanism is similar to sea breeze circulations, which are also driven by surface heating gradients. In this scenario, warm SST is associated with low SLP, cool SST with high SLP. In the tropics, surface winds tend to flow down the SLP gradient. Under this scenario, zonal wind perturbations are 90° out of the phase with the SST, while meridional wind changes tend to be either in phase or 90° out of phase depending on the latitude. Hashizume et al. (2001) found some evidence to support this hypothesis.

In the second hypothesis, SST is coupled with surface winds through stability changes in the atmospheric boundary layer (Hayes et al. 1989; Wallace et al. 1989, hereafter HMW). When the southeasterly trade winds flow from colder to warmer waters, the atmosphere becomes more buoyant, mixing increases, and wind shear is reduced in the boundary layer. As a result, surface winds increase. That is, increased boundary layer mixing brings high momentum air down to the surface. Under this scenario, the zonal winds are 180° out of phase with SST perturbations and meridional winds are in phase with them. Evidence to support this hypothesis was found by Liu et al. (2000), Hashizume et al. (2001) and Chelton et al. (2000b).

Until the late 1990s only limited in situ and satellite data were available to test LN and HMW theories. This was first noted in Hayes et al. (1989) when the authors did temporal correlations of differences in surface winds and SST from an array of moored sensors. They observed significant correlations in the wind speed associated with TIWs. The authors postulated that the coupling of the ABL to the TIWs could be accomplished by hydrostatic sea level pressure perturbations, changes in the ABL stratification, or a combination of the two. As a result of the phase relationship they observed between SST and near surface wind velocity perturbations, the authors concluded that the coupling was dominated by the

changes in stratification.

Global measurements of vector winds by satellite scatterometer have contributed greatly to an improved understanding of coupled ocean-atmosphere variability in the Tropics. Using measurements by the European Remote-sensing Satellite (ERS), Xie et al. (1998) and Contreras (2002) demonstrate space time structure of TIW-induced wind fluctuations. Using high resolution QuickSCAT data, Liu et al. (2000), Chelton et al. (2000b) and Hashizume et al. (2001) find in the cold tongue season, low wind speeds are measured over the cold water and higher speeds over the warmer surrounding waters. When the data are filtered to show anomalies due to TIWs, it is clear that the southeasterly trade winds are enhanced over the warm SST anomalies, and reduced over the colder anomalies. These results support the findings of HWM. Hashizume et al. (2001) also found some evidence to support LN hypothesis. They found that the magnitude of SLP-induced winds is comparable to those due to the vertical mixing in central Pacific. Using QuickSCAT and TMI data, Liu et al. (2000) and Hashizume et al. (2001) further indicate that nonprecipitating clouds tend to gather over the warm TIW anomalies or over the adjacent convergence zones of the surface winds, suggesting that TIWs may have an influence on the whole boundary layer. Hashizume et al. (2001) combined data from TMI and three Special Sensor Microwave/Imagers (SSM/I) (F-11,F-13,F-14) to obtain the column integrated water vapor, cloud liquid and precipitation. Their study indicates that the TIW signal and SST are strongly trapped near the equator in the Atlantic and significant variations of water vapor and clouds are observed in the ITCZ, where local SST perturbations are small. This remote response to TIWs appears to be more significant in the tropical Atlantic than in the Pacific. Chelton et al. (2000a) used wind stress from QuikSCAT and SST from TMI to investigate TIW-induced atmosphere-ocean interaction. The wind stress divergence is shown to be linearly related to the downwind component of the SST gradient with a response on the south side of the cold tongue that is about twice that on the north side. The wind stress

curl is linearly related to the crosswind component of the SST gradient with a response that is approximately half that of the wind stress divergence response to the downwind SST gradient. This close coupling between SST and wind stress supports the HWM hypothesis that surface winds vary in response to SST modification of atmospheric boundary layer stability.

Numerical modeling has also been used to investigate the underlying physical mechanisms governing tropical ocean-atmosphere feedbacks. Xie et al. (1998) used a global general circulation model to investigate the physical processes that occur in the atmospheric response to SST driving. Their study found that both vertical mixing and pressure gradient terms were equally important. However, the input SST field was idealized and fixed in time and the horizonal and vertical resolution of the model was rather coarse (2.8 horizontally and four levels in the PBL). Small et al. (2003) used a high-resolution (10 levels below 800 hPa and 0.5 grid resolution) regional model climate model to study the PBL response to SST variation. The daily SST product derived from a 3-day running mean of TMI data was used as model boundary condition. Their model study found that in addition to pressure gradient and vertical mixing mechanisms, horizontal advection can also be important in balancing the momentum budget within the PBL.

Analyzing the TIW-induced air-sea coupling, one obvious question is whether these TIW-induced perturbations of the wind field have a significant feedback onto the ocean circulation. Pezzi and Richards (2004) investigated whether TIW-induced wind field perturbations feed back onto the ocean circulation in the tropical Pacific by using an ocean model coupled and uncoupled to the atmosphere. They showed that the wind perturbations have a negative feedback that tends to reduce the SST and meridional velocity signatures of TIW. This, in turn, reduces equatorward eddy heat flux associated with TIW, thereby resulting in intensified cooling of equatorial cold tongue. This negative feedback has potentially important implications about the role of TIWs in climate variability.

CHAPTER III

DATA

A. SST Data

a. TMI SST

The SST data were obtained from the TRMM Microwave Imager (TMI) on board the TRMM satellite. TRMM is a joint mission between NASA in the United States and the National Space Development Agency of Japan. It was launched on November 27th 1997. The TRMM satellite is put in a nonsunsynchronous orbit with an inclination angle of 35° and a low altitude of 350 km. In August 2001, TRMM is boosted to a altitude of 400 km.

Because the atmosphere is nearly transparent to microwave radiation in nonraining conditions, the TMI provides an essentially uninterrupted record of the westward propagation of SST signatures of TIWs (Chelton et al. 2000b). TMI utilizes nine channels with operating frequencies of 10.65 GHz, 19.35 GHz, 21.3 GHz, 37 GHz, and 85.5 GHz. The lowest frequency channel of TMI penetrates non-rain clouds with little attenuation, giving a clear view of the sea surface except in regions of strong precipitation and near coasts. This is a distinct advantage over the traditional infrared SST observations that require a cloud-free field of view (Wentz et al. 2000). Rain contaminated observations are easily identified and eliminated from further analysis based on vertically and horizontally polarized brightness temperatures measured by the radiometer itself. Furthermore, at this low frequency, microwave retrievals are not affected by aerosols and are insensitive to atmospheric water vapor, making it possible to produce a very reliable SST time series for climate studies.

TMI estimates of SST are obtained from a physically-based algorithm that matches the brightness temperatures to a radiative transfer model that is a function of SST, wind speed, columnar water vapor, and columnar cloud liquid water. The algorithm is a direct

extension of the algorithm for retrieval of wind speed, columnar water vapor, and columnar cloud liquid water from the Special Sensor Microwave/Imager (SSM/I). SST cannot be obtained from SSM/I data because of the lack of measurements at 10.7 GHz.

Gentemann et al. (2004) compared TMI SST with buoy measurements. The result shows the good accuracy of TMI SST retrievals. Other geophysical variables retrieved by TMI: atmospheric water vapor, liquid cloud water and precipitation rates are also used in this study. The data cover latitudes from 40°S to 40°N at 0.25° latitude by 0.25° longitude resolution, separated according to ascending and descending orbits. TMI SST data used in this study are the TMI product Version 3a, spanning from January 1998 to December 2005 from RSS (Remote Sensing Systems). The wave signals are strongest near 2°N, indicated by the heavy lines in Figure 1, so this latitude is chosen for the display of longitude-time cross sections. The grey areas in the ocean represents missing SST data, primarily due to interference by rain. Most missing data occur in the ITCZ, which lies north of the main TIW zone, where rain rates are largest. Daily maps of these datasets are averaged in 3-day running mean composites. There are only a few small data gaps in the TIW region. Remaining gaps in the 3-day mean data are filled by linear interpolation in the zonal direction in this study.

b. Reynolds SST

The SST data used as boundary conditions in the CAM and MM5 models are TMI SSTs in the Tropics. Outside the Tropics, monthly Reynolds SST are used for monthly SST forcing and weekly Reynolds SST are used to compute daily SSTs.

The Reynolds SST analysis has been developed by Richard Reynolds from the Climate Modeling Branch of NCEP. A monthly one degree global SST climatology was constructed. This climatology was derived from monthly optimum interpolation (OI) SST

analysis with an adjusted base period of 1950-79. These analyses were based on ship and buoy SST data supplemented by satellite SST retrievals. In addition, an SST climatology was derived from monthly analyses using sea-ice coverage data over a 12-year period (1982-93). The one degree climatology resolves equatorial upwelling and fronts.

The optimum interpolation (OI) SST analysis is produced weekly on a one-degree grid. The analysis uses buoy and ship data, satellite SST data, and SST's simulated by sea-ice coverage. Before the analysis is computed, the satellite data is adjusted for biases using the method described by Reynolds (1988). A description of the analysis can be found in Reynolds and Smith (1994).

B. ENSO Index and Atlantic Niña Index

Since TIWs are visible undulations of the SST fields, it is natural to tie TIW activity to the annual and interannual variations of the cold tongues in the Atlantic and Pacific basins. Because the state of the cold tongue in the Pacific is dominated by El Niño-Southern Oscillation (ENSO) variability, in addition to the annual cycle, a relationship between TIW activity and ENSO is to be expected. The multivariate ENSO Index (MEI) is an index of ENSO state based on six observed variables over the tropical Pacific. The six variables are: sea-level pressure, zonal and meridional components of the surface wind, sea surface temperature, surface air temperature, and total cloudiness fraction of the sky. These observations have been collected and published in COADS (Comprehensive Ocean-Atmosphere Data Set) for many years. Negative values of the MEI represent the cold ENSO phase (La Niña), while positive MEI values represent the warm ENSO phase (El Niño). The MEI time series is bimonthly so the January value represents the December-January value and is centered between the months. Figure 3 shows the MEI from 1998 to 2005, the period of interest here. The figure shows the latter part of the strong 1997-98 El Niño, the La Niña

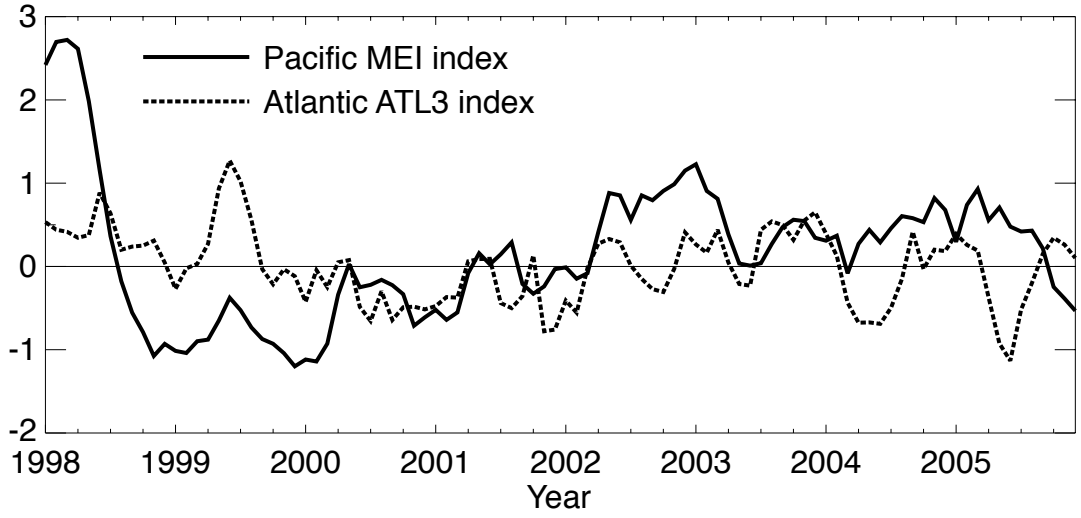

Fig. 3. Time series of Pacific MEI index (solid line) and Atlantic ATL3 index (dot line) from 1998 to 2005.

cold phase from mid-1998 to 2001, and the mild warm phase after 2001. Turning to the Atlantic, the coupled mode index, ATL3, is defined by Zebiak (1993) as the area-averaged SST anomaly over 3°N-3°S, 20°W - 0°. Figure 3 also shows the ATL3 index from 1998 to 2005 based on the TRMM monthly SST data. The figure shows a warm phase from 1998 to 1999 and a mild cold phase in 2000 and 2001. Both warm and cold phases appear in the remaining four years. The correlation between MEI ENSO index and ATL3 index is small (~ 0.4).

C. Wind Data

The surface vector winds analyzed here are from the SeaWinds scatterometer (Hoffman and Leidner 2005) launched on 19 June 1999 on board the QuikSCAT satellite. The geophysical data record began on 15 July 1999. The SeaWinds instrument on QuikSCAT is

the first satellite- borne scanning radar scatterometer. QuikSCAT is designed to provide accurate ocean surface winds in all conditions except for moderate to heavy rain. QuikSCAT data are invaluable in providing high-quality, high-resolution winds to detect and locate significant meteorological features and to produce accurate ocean surface wind analyses.

The QuikSCAT scatterometer infers wind stress magnitude and direction from measurements of microwave radar backscatter received from a given location on the sea surface at multiple antenna look angles. The wind retrievals are calibrated to the so-called neutralstability wind at a height of 10 m above the sea surface, that is, the wind that would exist if the atmospheric boundary layer were neutrally stable. The QuikSCAT instrument measures vector winds with 25 km resolution over a single 1600 km swath centered on the satellite ground track. The 1600 km QuikSCAT swath width is 33% greater than its predecessor, the dual-swath National Aeronautics and Space Administration scatterometer (NSCAT), and more than 300% greater than the narrow 500 km single-swath scatterometers on board the ERS-1 and ERS-2 satellites launched by the European Space Agency. Rain-contaminated QuikSCAT observations were flagged and eliminated from subsequent analysis by comparison with rain estimates from the three SSM/I satellites (F11, F13, and F14) that are in operation simultaneously with QuikSCAT.

The scatterometer operates in the Ku-band (13.4 GHz). QuikSCAT covers 93% of the global ocean under clear and cloudy conditions, night and day. QuikSCAT data extend from $89.875°$S to $89.875°$N with a spatial resolution of $0.25°$ latitude by $0.25°$ longitude. Daily maps of these datasets are averaged in 3-day mean composites. Gaps in the 3-day mean datasets are filled with simple spatial interpolation method in this study. The SeaWinds data is the product Version 3, spanning July 1999 to December 2005. Both QuikSCAT wind data and TMI SST data are available at Remote Sensing Systems (http://www.ssmi.com).

D. Rain Data

The 3B42 rain rate data are used to study the rain rate response to TIWs. The purpose of the 3B42 algorithm is to produce TRMM merged high quality (HQ)/infrared (IR) precipitation estimations. These gridded estimates have a 3-hour temporal resolution and 0.25° X 0.25° spatial resolution in a global belt extending from 50°S to 50°N latitude. The 3B42 data are averaged to daily temporal resolution to match the SST data resolution.

E. TMI Data

The TMI also measures column-integrated water vapor and cloud liquid water. These variables are poorly sampled by a single microwave imager due to high-frequency variability. We combine the TMI and four Version 5 SSM/Is (F-11, F-13, F-14, F-15) that were simultaneously in space with TRMM. For data from 1998 to 1999, we combine the TMI, F-11, F-13 and F-14. For data from 2000 to 2005, we combine the TMI, F-13, F-14 and F-15. The combination of these five microwave imagers greatly improves the sampling of water vapor and cloud liquid water. TMI, SSM/I and QuikSCAT data are processed and made available by RSS (http://www.ssmi.com).

F. Monthly SST and OLR Data

Monthly mean Reynolds SST and monthly mean Outgoing Longwave Radiation (OLR) are used to study the interannual variability of ITCZ location in the Atlantic Ocean. Monthly mean SST covers the period from 1982 to 2005 with 1° grid resolution. Monthly mean OLR data are from 1974 to 2005 with 2.5° grid resolution.

CHAPTER IV

MODELS

A. CAM3

The Community Climate System Model (CCSM) is a coupled model for simulating past, present, and future climates. In its present form, CCSM consists of four components for the atmosphere, ocean, sea ice and land surface linked through a coupler that exchanges fluxes and state information among these components. The most recent version, CCSM3, was released to the climate community on 23 June 2004. The CCSM3 system includes new versions of all the component models. The atmosphere is Community Atmosphere Model (CAM) version 3.0 (Collins et al. 2004).

CCSM3 has been designed to produce simulations with reasonable fidelity over a wide range of resolutions and with a variety of atmospheric dynamical frameworks. This is accomplished by introducing dependence on resolution and dynamics in the time step and twelve other adjustable parameters in CAM3. Those parameters affect the physics governing clouds and precipitation and the biharmonic diffusion coefficients for temperature, vorticity, and divergence. The parameter values have been adjusted to yield climate simulations with nearly balanced top-of-model energy budgets and realistic zonal-mean top-of-atmosphere cloud radiative forcing.

In this study, two control runs are made to test the sensitivity of the model to horizontal resolution. The first control run has T42 horizontal resolution for spectral Eulerian dynamics, and 128 longitudinal by 64 latitudinal grid points for physical parameterizations. The second control run has T85 horizontal resolution for spectral Eulerian dynamics, and 256 longitudinal by 128 latitudinal grid points for physical parameterizations. For both control runs, the vertical dimension resolution is 26 levels with a hybrid terrain-following coordi-

nate. The vertical grid transitions from a pure sigma region in the lowest layer through a hybrid sigma-pressure region to a pure pressure region above approximately 83 mb.

SST data used for the simulation are 3-day mean daily SSTs from TRMM satellite and weekly Reynolds SST. In the Tropics, 35°S to 35°N, daily SSTs from TRMM are used. At latitudes higher than 40°, weekly Reynolds SSTs are used. At latitudes between 35° and 40°, in both the northern and southern hemispheres, linear interpolation is set to make the SST gradient smooth between these two types of data.

Four-member ensembles simulations were performed for both control runs. All of the simulations use initial conditions May, with a 10-min time step. The simulations were run from May 1st 2000 to September 29th 2000 and used prescribed distributions of daily SSTs. The first month of the simulations is regarded as spinup, and the remaining 3 months (June 1st 2000 to September 29th 2000) are analyzed.

B. MM5

This study also uses a regional climate model, the PSU/NCAR MM5 model. The MM5 model is a limited-area, nonhydrostatic, terrain-following, sigma-coordinate model designed to simulate or predict the mesoscale atmospheric circulation. MM5 version 3.4 (Grell 1994) is used to study the atmospheric response to TIWs in the Atlantic Ocean. MM5 uses finite differencing in both space and time. The model has 24 vertical sigma levels. In this study a large domain is designed to position the lateral boundaries far from the area in which the important aspect of TIWs and reduce the possibility that disturbances propagate into the domain, rather than being generated by the model physics. Boundaries are located at $12°$S and $47°$N in latitude and $112°$W and $25°$E in longitude. SSTs from the year 2000 are used for the simulations.

Two simulations are carried out. The first uses monthly-averaged SST. The second

simulation uses daily SSTs . In the region between 12°S and 35°N, SST data are from the TRMM satellite. In the region from 40°N to 47°N, SST data are from the Reynolds SST (Reynolds 1988; Reynolds and Smith 1994). SST are linearly interpolated between TRMM and Reynold SST data in the region from 35°N to 40°N to produce a smooth transition between the two different SST data sets. Daily SSTs for this simulation use data from 3-day running-mean TRMM SST and weekly Reynolds SST. Both daily and monthly SSTs are prescribed and updated every 12 hours using linear interpolation in the simulation.

Physical options chosen for the simulations include the following: the high resolution Blackadar planetary boundary layer scheme (Blackadar 1979; Zang and Anthes 1982); stable precipitation explicit moisture scheme; Rapid Radiative Transfer Model (RRTM) longwave scheme (Mlawer et al. 1997); Grell convective scheme (Grell 1993); and shallow cumulus parameterization (Grell 1994).

Each model simulation uses an 80 km grid and a model time-step of 2 minutes. The simulations are initialized at 0000 UTC on May 14th and run through the middle of December. The first 15 days are discarded for model spin-up. Initial conditions are climatological May conditions from the National Centers for Environmental Prediction (NCEP) reanalysis. Monthly means from the reanalysis are taken to represent the middle of the month. Lateral boundary conditions for winds, temperature and moisture at each vertical level are also taken from NCEP reanalysis, updated every 12 hours based on a linear interpolation between monthly means as in Vizy and Cook (2002 (D3). Thus, the boundary conditions include the effect of the seasonal cycle but not the diurnal cycle or synoptic-scale variability. Finally, the 6-hourly output data is averaged to form a climatology of TIWs.

CHAPTER V

METHODS

In order to isolate TIW variability from other temperature signals, such as the seasonal cycle, a filtering scheme is used.The filter is designed using prior knowledge of the approximate range of the period and wavelength of the waves. Data are bandpass filtered in space by applying moving averages of 5° and 12° ($\sim$ 600 km to 1300 km) in the zonal and in time by applying moving averages of 20 and 40 days. For each year the SST variance is used as an index of the amplitude of the TIW. Using the bandpass filtered SSTs, the temporal variance is computed at each point, then averaged over the active TIW region. We use this filter to derive anomaly fields of SST. After the filtering, the Radon transform technique is applied to estimate the propagation characteristics of the TIW.

The Radon transform in two dimensions is an integral transform consisting of the integral of a function over a set of linear paths with varying orientations and offsets (Figure 4). The inverse Radon transform is commonly used in computerized tomography to reconstruct the internal structure of objects from x-ray data. Because TIWs are nearly monochromatic, when θ is aligned with the wave propagation, the path integrals will vary with ρ as the offsets move from wave crest to wave trough. The wave phase speed is found by identifying the angle θ that has the largest variance in the path integral with respect to ρ. The wavelength can be estimated by analyzing the alternating maxima and minima of the Radon integrals at the θ with the greatest variance. Hill et al. (2000) have detailed descriptions on how to use Randon transform to estimate phase speed.

Our aim is to investigate the covariability of the geophysical fields measured by the satellite. Following Hashizume et al. (2001), a linear regression technique is used to map the spatial structure of the TIWs. Using the grid point with maximum TIW SST variability as a reference point (x_0, y_0), a linear relation between the atmospheric fields at each point

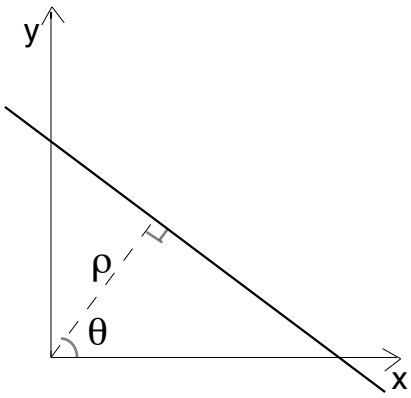

Fig. 4. The scheme of Radon transform to estimate wave characteristics from the longitude–time TIW distribution. The angle θ specifies the orientation of the path, while ρ is the offset from the origin. The solid line indicates the path over which the function $f(x, y)$ is intergrated. The Radon transform is the value of the path integrals for all θ and ρ.

and SST at the reference point is computed using least squares. It seeks a linear relation between one of the filtered atmospheric fields $F_f(x, y, t)$ and the filtered SST at the reference point $T_{f0} = T_f(x_0, y_0, t)$. Since the mean of the filtered SST anomalies is approximately equal to 0, the regression relation $F_f = bT_f$ instead of $F_f = a + bT_f$ is used.

The least squares method leads to the regression coefficients,

$$b(x, y) = \sum_{n=1}^{N} F_f(x, y, t_n) T_{f0}(t_n) / \sum_{n=1}^{N} T_{f0}^2(t_n) \tag{5.1}$$

The regression method is useful to identify the relationship between an atmospheric variable and a TIW SST index at reference point (Hashizume et al. 2001).

The correlation coefficients (r^2) of the regression measure the fraction of the total variance of the dependent variable explained by the SST. To investigate how much variation of the atmospheric field $F(x, y)$ is explained by the TIW SST T_f, we use the same regression model, $F = bT_f$. With the same least square method, we obtain the R-value:

$$R^2(x, y) = S_{ft}^2(x, y) / (S_{tt}(x, y) S_{ff}(x, y)) \tag{5.2}$$

where,

$$S_{ft}(x, y) = \sum_{n=1}^{N} ((F(x, y, t_n) - \overline{F(x, y, t_n)}) T_{f0}(t_n)) \tag{5.3}$$

$$S_{tt}(x, y) = \sum_{n=1}^{N} T_{f0}^2(t_n) \tag{5.4}$$

$$S_{ff}(x, y) = \sum_{n=1}^{N} (F(x, y, t_n) - \overline{F(x, y, t_n)})^2 \tag{5.5}$$

CHAPTER VI

INTERANNUAL VARIATIONS OF TIWS

The characteristics of TIWs are largely controlled by the background ocean currents, which have been studied with models and observations. An early analytical study by Philander (1978) demonstrates that the period of the waves is affected by changes in the strength of the mean flow and the latitudinal scale of the shear. The wavelength is also affected by the width of the shear zone. Philander and Pacanowski (1986) demonstrate that seasonal and longitudinal changes in the shear of the currents affect the amplitude, period and wavelength of the waves. Using shipboard acoustic Doppler profiler-derived zonal currents, Johnson and Proehl (2004) show that the equatorial currents have a significant seasonal cycle and are affected by El Niño-Southern Oscillation (ENSO) cycles in the Pacific Ocean. Since TIWs are the result of the instability of meridional shears associated with the equatorial currents, an ENSO influence on the Pacific TIW characteristics is expected.

Like the air-sea coupled ENSO mode in the equatorial Pacific, the equatorial Atlantic has a similar coupled mode (Zebiak 1993). The Atlantic coupled-mode signal is less robust than the corresponding Pacific ENSO signal, but is still well-defined. The Atlantic mode signature is even more tightly focused on the equator and is situated proportionally farther to the west within the basin than its Pacific counterpart. Since ENSO has an influence on the Pacific TIW activities, in this chapter we investigate whether the Atlantic coupled mode could give rise to the TIW variation in the Atlantic.

A. Basic Characteristics

Figures 5 and 6 are unfiltered time-longitude plots of SST in the Pacific and Atlantic Oceans at 2°N. TIWs are clearly visible in the SST data as westward-propagating waves with a seasonally modulated intensity. The waves are most intense when temperatures are coldest

and weak when temperatures are warm. In the Pacific (Figure 5), TIWs start to develop in June and propagate westward. The waves typically have maximum amplitude between 130°W and 100°W, but their propagation can be traced as far west as the dateline. The strong period of wave activity usually ends in January or February. From March to May, TIW activity ceases. On the interannual timescale, the Pacific waves vary in concert with the phase of ENSO. Activity is strongest during the La Nina phase when the cold tongue is most pronounced (e.g. 1999) and the waves are weaker in warmer intervals when the SST front is weak (e.g. 2002). During the strong El Niño in the first half of 1998, the SST cold tongue disappeared completely and TIW activity ceased. During the following strong La Niña conditions from mid-1998 to 1999, the cold tongue extends further west. During the warm conditions from 2002 to mid-2005, wave activity is relatively weak. The result agrees with a previous long-term TIW observation study using Renolds weekly SST data that showed that TIW activity is strongest during the La Niña phase and weak or nonexistent during the El Niño phase (Contreras 2002).

In the Atlantic (Figure 6), the equatorial cold tongue starts to appear in late May. As the equatorial currents and the equatorial SST front start to strengthen, waves appear in early June. The Atlantic TIWs grow rapidly in the region from 0° to 10°W, reach maximum magnitude around 15°W, and then decay westward; but their propagation can reach 35°W. Unlike the Pacific, the Atlantic cold tongue reaches its maximum strength in early August and then weakens. Such a rapid development of the Atlantic cold tongue is a climatological feature of the Atlantic (Mitchell and Wallace 1992), presumably due to the strong influence of neighboring continents. The cold tongue and wave activity are strongest in 2001. The strength of the cold tongue in the Atlantic Ocean does not appear to vary strongly with ENSO condition as it does in the Pacific, but may vary with Atlantic coupled condition (more on this question below).

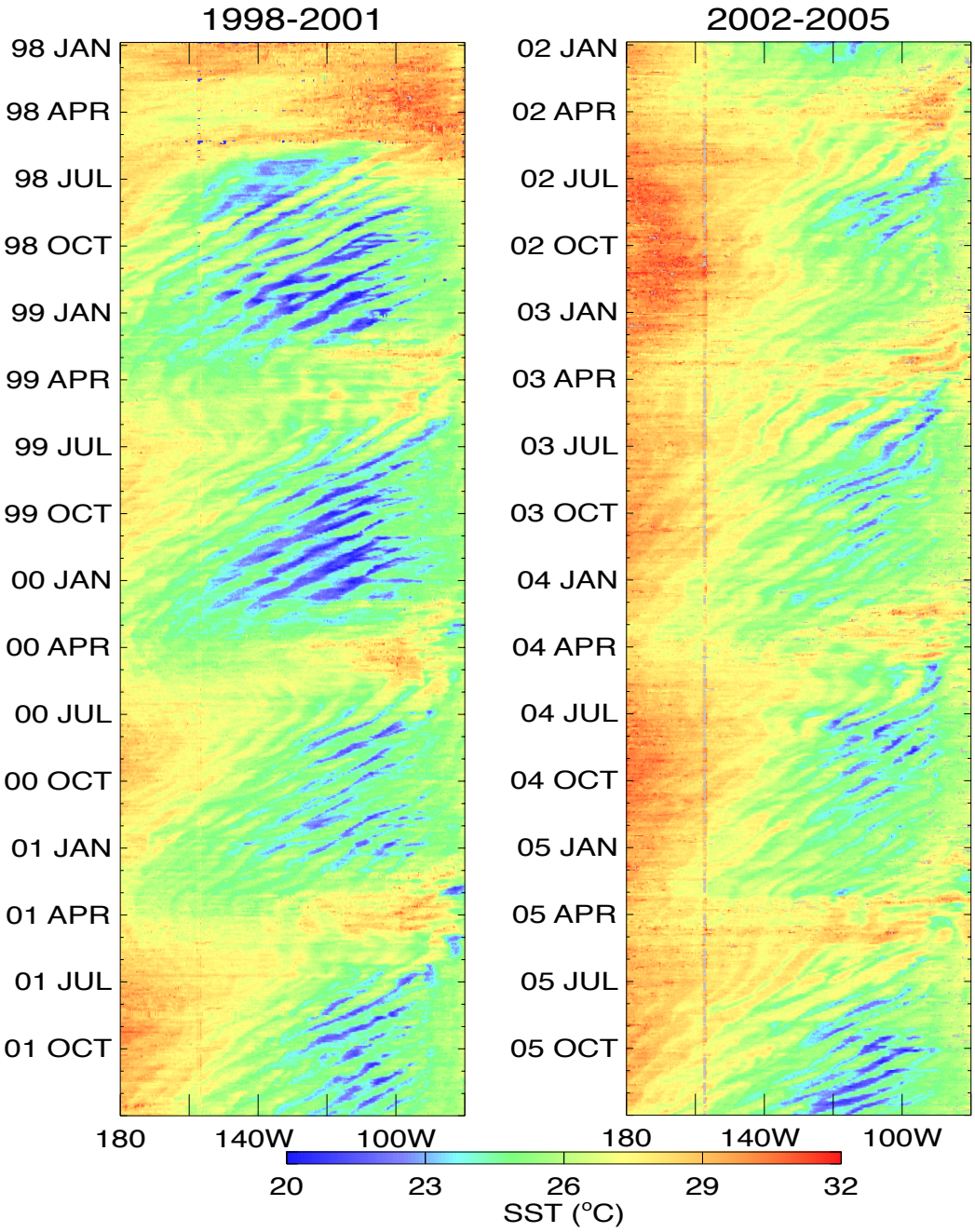

Fig. 5. Longitude-time plot of TMI SST from 1 Jan 1998 through 31 Dec 2005 in the Pacific Ocean. From mid-1998 to 2001 are in La Niña phase, and from 2002 to mid-2005 are mild El Niño phase.

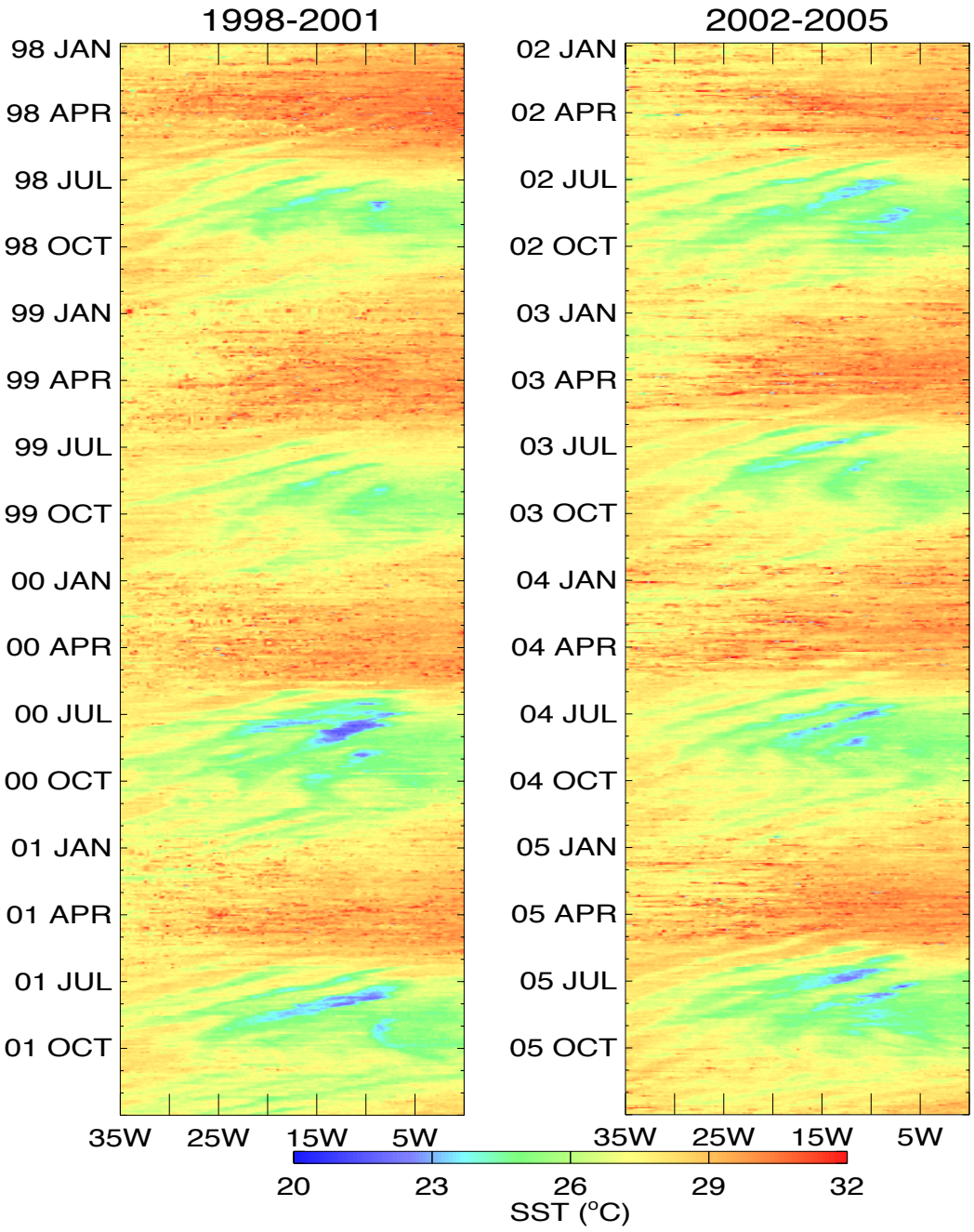

Fig. 6. Longitude-time plots of TMI SST from 1 Jan 1998 through 31 Dec 2005 in the Atlantic Ocean.

B. Horizontal Structure

Regression maps created using filtered SSTs show the horizontal structure of the TIWs for each year (Figure 7 and Figure 8). In each panel the reference point for the regression is indicated by a plus sign. The regression for the Pacific Ocean (Figure 7) covers the period from June to December, when the waves are most active (Figure 5). The most active TIWs in this region extend from the equator to 6°N with a zonal wavelength of about 10°. In some years TIWs can reach 8°N. The most intense waves are in the region between 140°W and 100°W. The zonal location of active TIWs varies from year to year. During the La Niña phase, when the equatorial cold tongues are well developed (e.g.1998, 1999), the most intense waves extend farther west. Evidence of weak waves south of the equator is found in all years. These weak westward-propagating waves can also be found as far as 5°S in longitude-time plots of SST filtered in the TIW band (not included). Southern hemisphere (SH) waves may not be coherent with northern hemisphere (NH) waves. Using a NH reference point may artificially suppress SH waves. The horizontal structure of these weak waves can be seen more clearly with a SH reference point.

In the Atlantic (Figure 8), the regression covers the period June, July and August, following Figure 6. The most active TIWs in this region are from 0° to 35°W, and from the equator to 5°N, with a wavelength of about 10°. The location of waves varies slightly from year to year. Weaker waves are found south of the equator in some years. Chelton et al. (2000b) states that TIWs are barely detectable south of the equator in the Atlantic Ocean with TRMM data in 1998. But weak westward-propagating waves do show up in the regression map and exist in the region between the equator and 5°S in longitude-time plots using SST filtered in the TIW band (not included). These weak waves are weaker than those south of the equator in the Pacific Ocean.

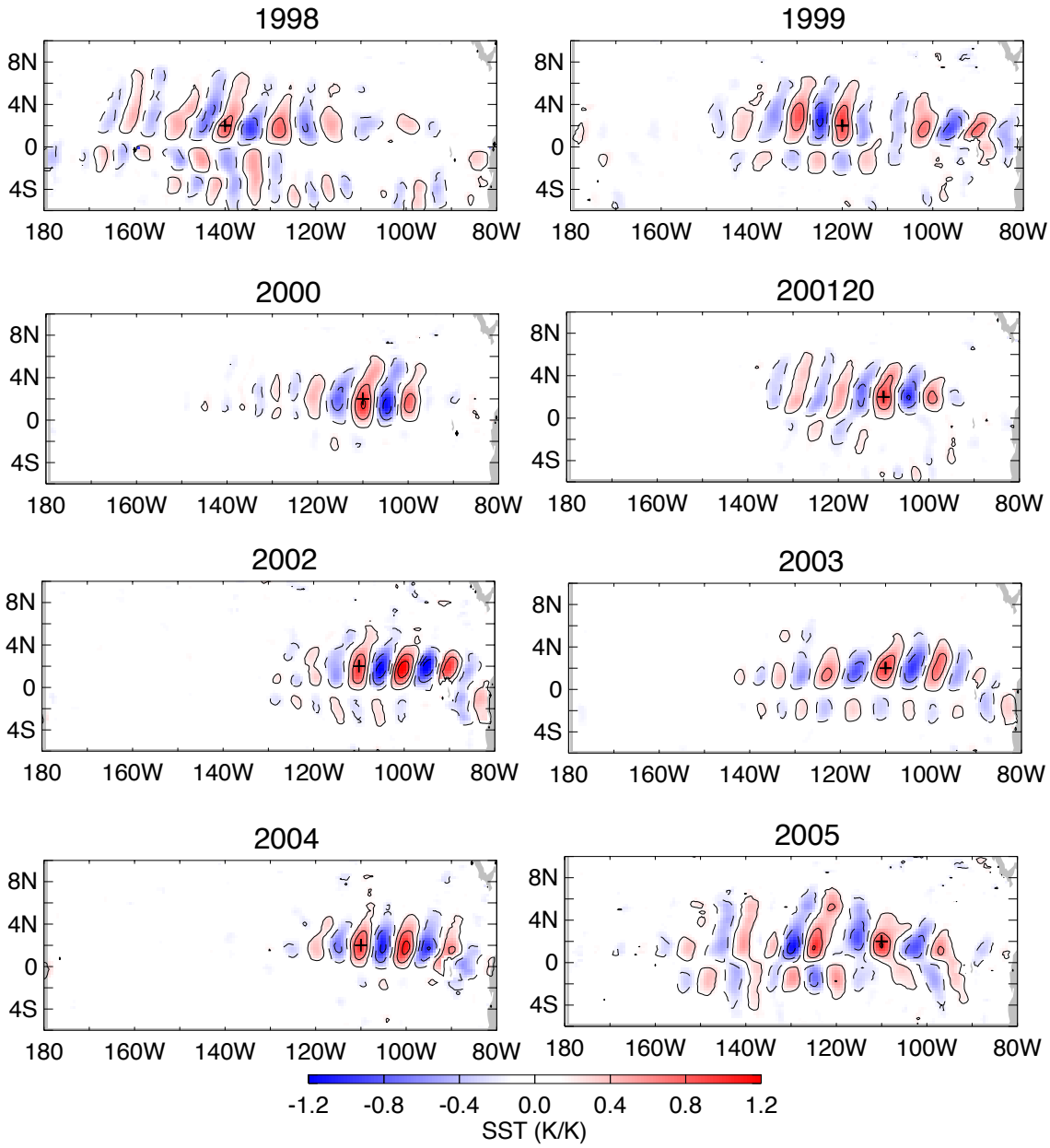

Fig. 7. Regression maps for SST in the Pacific Ocean from 1998 to 2005 in the period from June to the end of each year. The plus sign represents the reference point of the regressions. The contour interval is 0.4k.

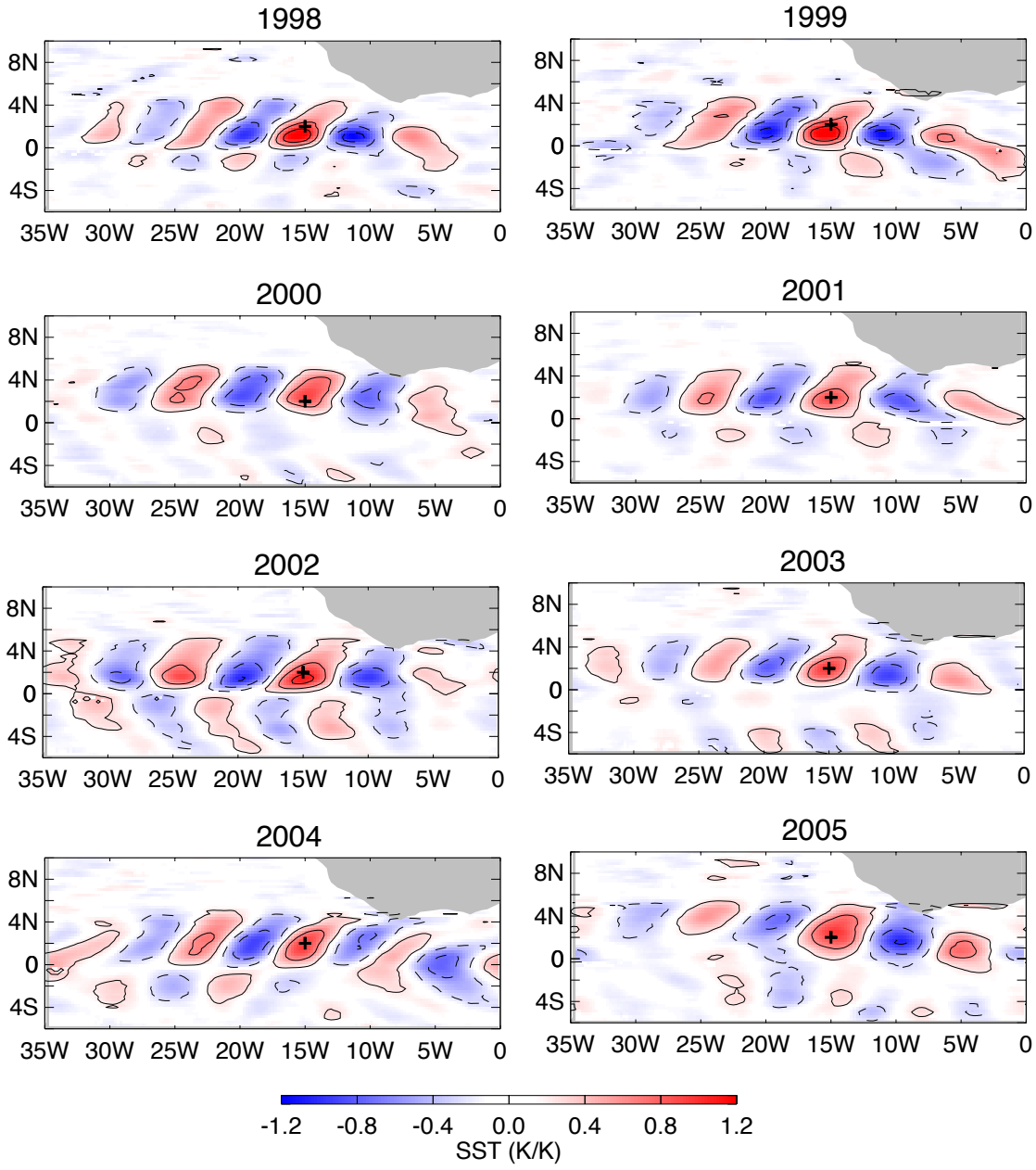

Fig. 8. Regression maps for SST in the Atlantic Ocean from 1998 to 2005 in the period of JJA. The plus sign represents the reference point of the regressions. The contour interval is 0.4k.

C. Interannual Variability

The SST variance can be used as an index of the amplitude of the TIW. Using the bandpass filtered SSTs, the temporal variance is computed at each point, then averaged over the active TIW region. The active TIW regions are defined according to the TIW horizontal structure in both basins. Figure 9 shows scatter plots of SST variance as a function of the ENSO index (MEI) for the TIW active seasons in the Pacific Ocean and SST variance as a function of the Atlantic coupled mode index (ATL3) in the Atlantic Ocean.

In the Pacific there is a clear negative relationship between the MEI and the wave activity index. This indicates that the ENSO phenomena does have an effect on TIW activity in the Pacific. The TIW SST variance decreases as the ENSO index increases, which means that during La Niña periods TIWs have larger variance, that is, stronger wave activity. TIWs are most active in 1998 and 1999, which is during the strong La Niña period.

In the Atlantic Ocean, the scatter plot of TIW SST variance versus ATL3 also shows a negative relationship between ATL3 and the wave activity index. It indicates the Atlantic coupled mode influences the TIW activity in the Atlantic ocean in the same sense as the ENSO phenomena in the Pacific. TIWs are most active in 2001, which is during an ATL3 cold phase. TIWs are weakest in 1999, when ATL3 is in the warmest phase. The scatter plot of TIW activity in the Atlantic Ocean as a function of ENSO does not show any relationship (not shown).

The wavelength and wave speed estimated from the Radon transform in the Pacific and Atlantic Oceans show year-to-year variations due to different oceanographic conditions. The wavelength (Table I) in the Pacific Ocean varies from $\sim$10° to 12° longitude, while in the Atlantic Ocean the wavelength varies from $\sim$8° to 10°. The wave speed in the Pacific Ocean varies from $\sim$40 to 50 cm/s, while in the Atlantic Ocean the wave speed varies from $\sim$35 to 45 cm/s, slower than that in the Pacific Ocean.

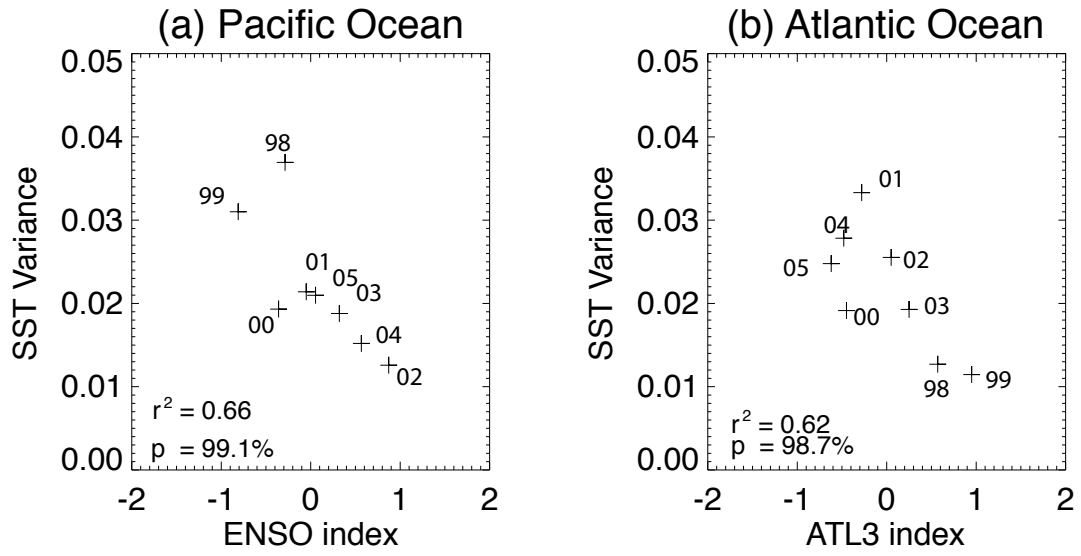

Fig. 9. TIW variance as a function of ENSO index (MEI) for the Pacific and a function of Atlantic coupled mode index (ATL3) for Atlantic Oceans. (a) Pacific Ocean from June to the end of the year in the region from 80°W to the dateline, from 0° to 5°N; (b) Atlantic Ocean from June to August in the region from 0° to 35°W, from 0° to 5°N.

Table I. Wave Characteristics of the Pacific and Atlantic Ocean at 2°N

	1998	1999	2000	2001	2002	2003	2004	2005
Pacific Speed (cm/s)	55.3	48.2	47.2	45.7	42.8	42.5	44.8	40.0
Pacific Wavelength (°)	11.3	11.8	10.8	11.2	11.1	10.8	10.3	12.0
Atlantic Speed (cm/s)	33.7	42.7	34.6	37.4	38.4	33.7	42.7	37.4
Atlantic Wavelength (°)	8.1	9.5	9.8	9.9	9.9	9.4	8.5	10.0

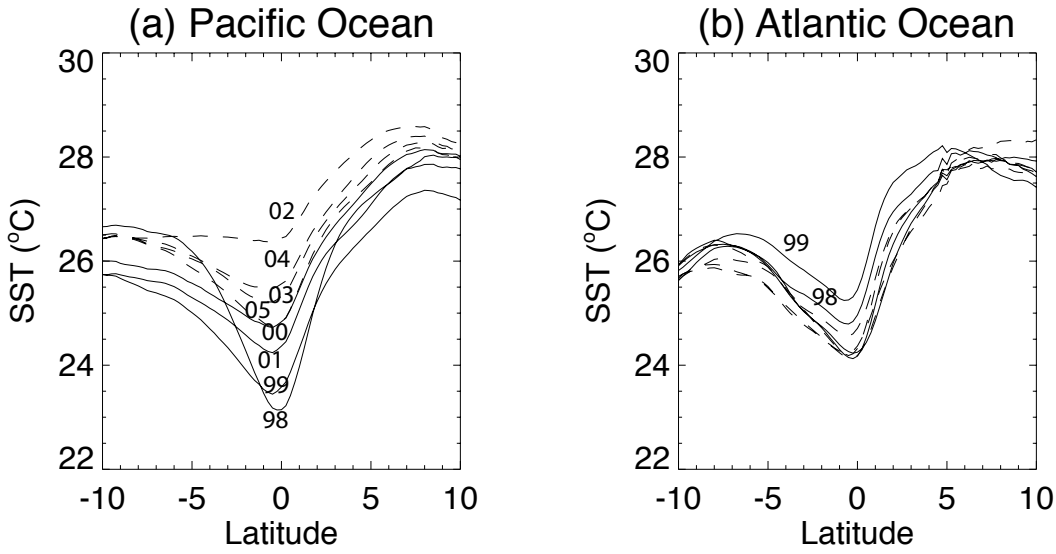

Fig. 10. Zonal mean SST in the Pacific and Atlantic Ocean from 1998 to 2005. Solid lines represent SST from 1998 to 2001 and dash lines represent SST from 2002 to 2005. (a) Pacific Ocean from June to the end of the year in the region from 180°W to 80°W; (b) Atlantic Ocean from June to August in the region from 0° to 35°W.

To evaluate the interannual variability of the basic state and its influence on the wave characteristics, we show meridional plots of the time-mean zonal-mean SST for the two basins in Figure 10. These zonal-mean SSTs have interannual variations in both basins, but the interannual variation in the Pacific is larger than that in the Atlantic, with mean SSTs much colder in the La Niña period than that in the El Niño period. The interannual SST variability in the Atlantic is small.

The meridional gradients of average SST are crucial for detecting TIWs. Strong positive and negative meridional SST gradients are associated with the SST fronts that bracket the equatorial cold tongue (Chelton et al. 2000b). We measure the SST meridional gradient at 2°N by the difference between the SST at 4°N and the equator. Scatter plots of the

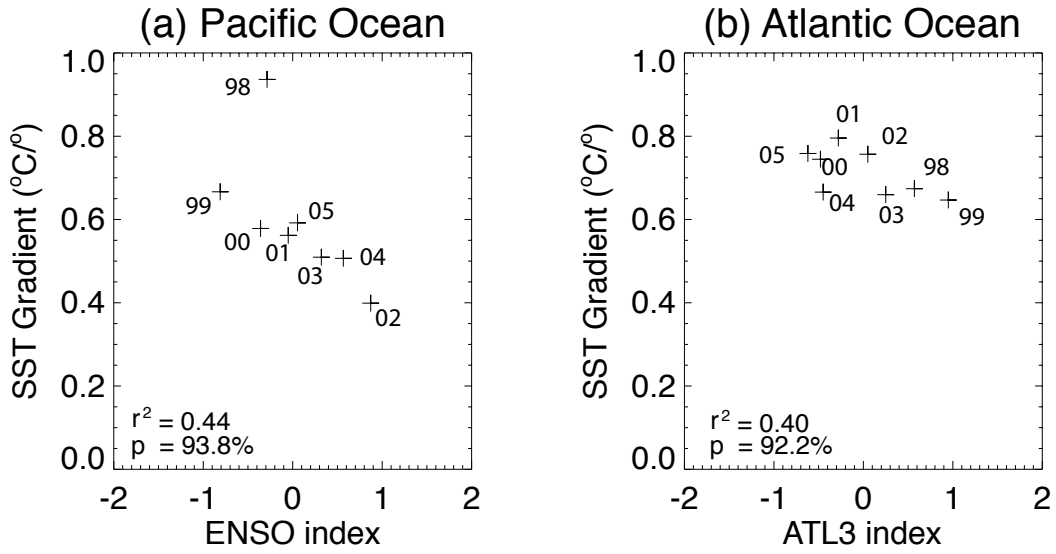

Fig. 11. Mean SST gradient from 4°N to equator as a function of ENSO index (MEI) for the Pacific and and a function of Atlantic coupled mode index (ALT3) for Atlantic Oceans. (a) Pacific Ocean from June to the end of the year in the region from 180°W to 80°W; (b) Atlantic Ocean from June to August in the region from 0° to 35°W.

meridional SST gradient in each basin and respective indices (Figure 11) show negative relationships in the both oceans. It indicates the mean SST gradient state in each ocean is influenced by the air-sea coupled mode background there.

D. Conclusions to Chapter VI

TIWs have a well-defined seasonal cycle in both the Pacific and Atlantic basins. In the Pacific, waves appear around June and disappear in the early part of the following year. The waves are typically most intense between 100°W and 130°W. TIWs are observed on both sides of the Pacific cold tongue, but the most intense waves are on the northern side

between the equator and 6°N. On internannual time scales the wave activity varies with the phase of ENSO. Wave activity is strongest and extends farthest west during ENSO cold phases, as measured by the Multivariate ENSO Index (MEI). Waves are weak when the MEI index is positive, indicating warm ENSO conditions; and the waves appear to have vanished entirely during the strong 1997-1998 El Niño, although TRMM did not observe the first part of that El Niño.

In the Atlantic Ocean, TIWs develop rapidly due to geographic features of the basin, beginning in June and terminating in August. In the Atlantic, TIWs develop in the region between 0° and 35°W. The location of TIWs does not vary much from year to year. TIWs are most active between the equator and 5°N. Weak TIWs are also detected south of the equator in the Atlantic. Unlike the Pacific, TIW activity in the Atlantic does not show a clear relationship with Pacific ENSO indices. TIW activity in the Atlantic is influenced by the Atlantic air-sea coupled mode as measured by the ATL3 index. As in the Pacific, wave activity is strongest during the cold phase of the Atlantic coupled mode, and weak when the ATL3 index is positive, the warm phase of the Atlantic coupled mode.

Wave amplitude, wavelength, and phase speed vary from year to year in both basins. Generally, TIWs in the Pacific have a longer wavelength and higher wave speed than those in the Atlantic. Interannual variations of TIW characteristics are associated with interannual variations of the background oceanographic state. Zonal-mean SSTs during the TIW active seasons in the Pacific have more interannual variability than in the Atlantic Ocean, responding in part to gradients that vary with the ENSO cycle. In the Atlantic, SST gradients vary with the Atlantic coupled mode, and stronger waves occur when SSTs are colder and SST gradients are larger. In keeping with theoretical considerations, colder SSTs and larger SST gradients imply stronger currents and shears, which lead to greater available energy for wave instabilities.

CHAPTER VII

ATMOSPHERIC RESPONSE TO ATLANTIC TIWS

Interactions between the ocean and the atmosphere play a fundamental role in determining tropical climate variability. Current research on the response of the atmosphere to SST variation has focused on the El Niño-Southern Oscillation (ENSO) phenomena in the tropical Pacific. ENSO wind anomalies are mostly induced by changes in deep convection, which are limited to high-SST regions. TIWs, on the other hand, induce wind changes over relatively cool SSTs. TIWs are an important aspect of equatorial ocean dynamics and thermodynamics. Since TIWs transport a substantial amount of heat and momentum across the equatorial front (Hansen and Paul 1984, Weisberg 1984), this high-frequency ocean-atmosphere interaction could have an effect on the tropical climate (Xie et al. 1998).

In the previous chapter, we showed that TIW SST interannual variability in the Atlantic Ocean is related to the interannual Atlantic equatorial mode (or Atlantic Niño). It is thus interesting to investigate how the atmospheric response to the TIW SST anomalies varies from year to year. Hashizume et al. (2001) showed that significant variability of wind, water vapor, cloud liquid water, and precipitation can be observed in the Atlantic ITCZ, where direct TIW forcing is absent. They hypothesized that TIWs can have a remote influence on the ITCZ. Nevertheless, the authors use only a short time series of satellite data from 1999, which prevents study of interannual variations.

Some important questions about the atmospheric response to TIW in the Atlantic Ocean are: What is the interannual variability of the atmospheric response to the TIW SST anomalies? Is the atmospheric remote response to TIW SST anomalies in the Atlantic Ocean in 1999 typical? To what extent do these SST anomalies have an impact on rainfall variability in the ITCZ? We use eight years of TRMM data, six years of QuikSCAT data, and available SSM/I data to address these questions.

A. Atmospheric Response

Figures 12 and 13 show the time-mean large-scale characteristics of the SST, surface wind and precipitation fields during the TIW season. The top panel in each figure is the climatological map for 1998-2005. Because 1999 had some unique characteristics, separate maps for that year (to be discussed later) are included in each figure. In the Tropics, the ITCZ is collocated with maximum SSTs. During the boreal summer, the cold tongue in SST develops along the equator and the ITCZ reaches its northernmost extent. During the years 1998 to 2005, on average, the northern boundary of the ITCZ in the Atlantic Ocean in JJA lies at 10°N, although the location of the ITCZ varies from year to year. The southern boundary of the ITCZ is located near 4°N, except in 1999, when the southern boundary is about 2°N (Figures 12b and 13b). The contours in Figure 12 represent the temporal variance of the filtered SST. This is the temporal variance at each point of the bandpass filtered SSTs. The largest filtered SST variance is found to the south of the ITCZ, where there are large meridional SST gradients. The SST variance can be used as an index of the TIW activity. TIWs are most active in the latitudes between 1°N and 5°N. Weak TIW activity is also visible to the south of the equator (Figure 1).

Figure 13(a) presents the time-mean precipitation in JJA for 1998 to 2005 and the time-mean surface wind fields for 2000 to 2005. In the Tropics, rainfall is primarily associated with deep convective activity. The region of enhanced rainfall (ITCZ) constitutes the upward branch of the Hadley circulation. As the southeasterly trades in the Atlantic basin flow across the cold tongue, they gain speed and become more southerly between 0° and 10°N. The southeasterly and northeasterly trades converge around 10°N over the warmest water. The mean wind speed in the TIW active region between 0° and 5°N is about 6.5 m/s, and the maximum seasonal mean wind speed is about 8 m/s. As stated above, Figure 13(b) shows that the warmest SST and the ITCZ lie further south in 1999 than is typical of the

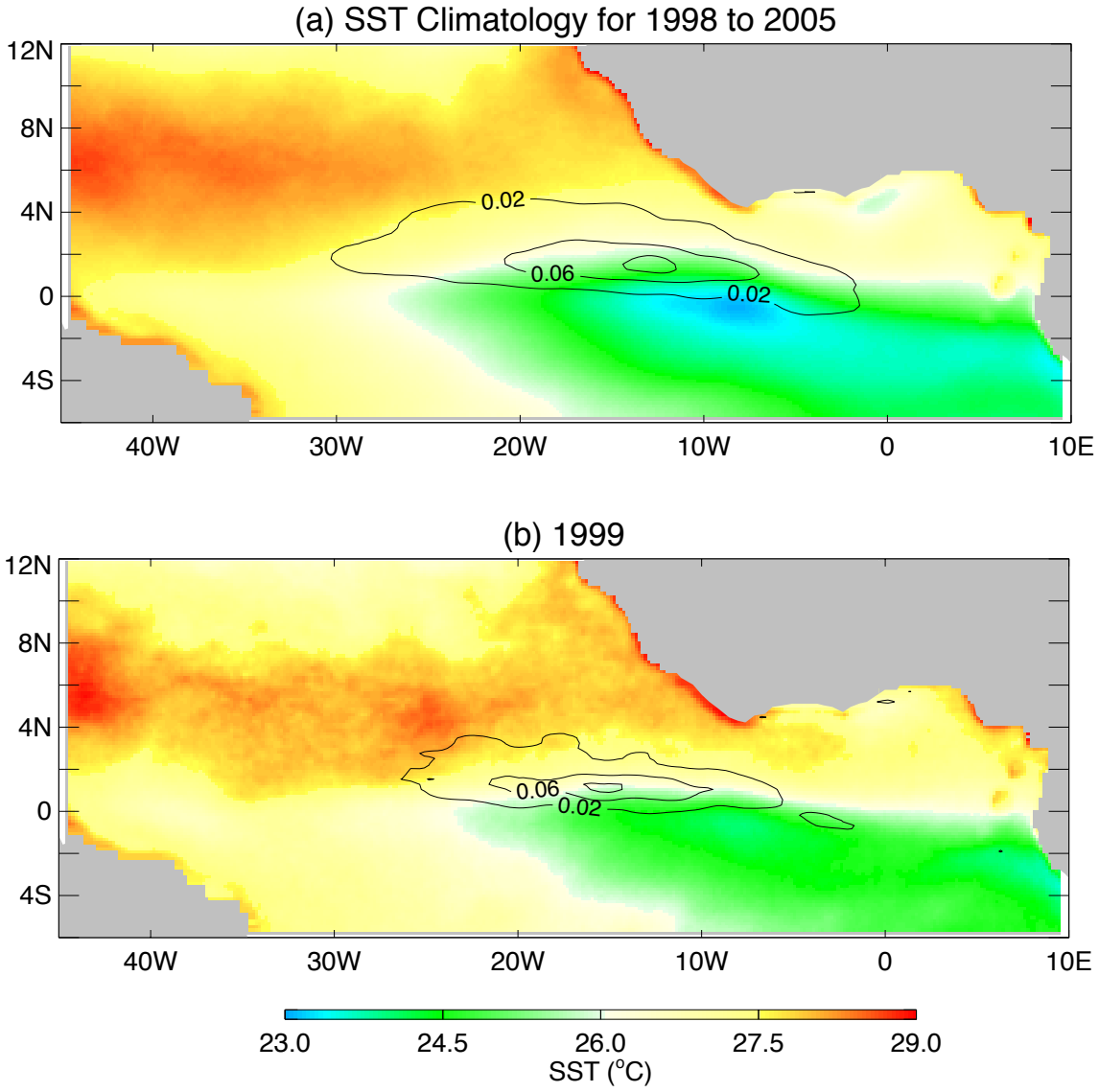

Fig. 12. Time-averaged SST (color) and TIW SST variance (contours in $^{\circ}C^2$) for JJA (a) 1998 to 2005. (b)1999.

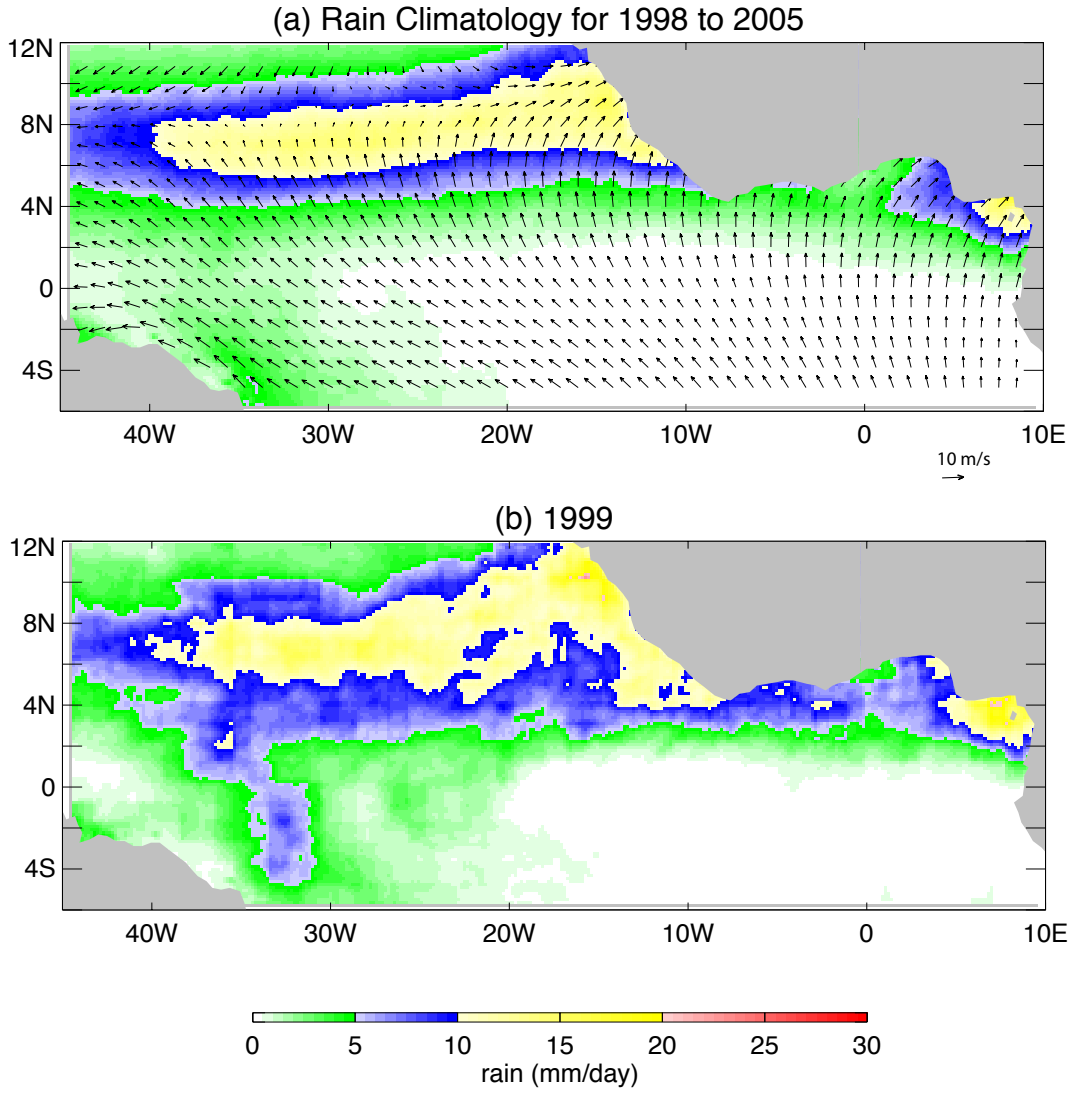

Fig. 13. Time averaged rainfall and wind velocity (vectors) in the period of JJA from 1998 to 2005. (a) the climatology from 1998 to 2005. (b) in 1999.

eight-year climatology.

Figure 14 shows regressions of SST and wind for each individual year. The regression maps created using filtered SSTs show clear horizontal structure in SST and wind velocity. As previous studies have shown (Liu et al. 2000; Hashizume et al. 2001), the typical TIW wavelength is about 10° in the SST regression. Phase lines tilt southwest to northeast. The SST anomalies are approximately antisymmetric about the equator with much weaker southern anomalies. The TIW-induced SST variations are 0.3∼0.6K in magnitude in our selected band. Figure 15 shows an example of an SST anomaly time series at the reference point (15°W, 2°N) in 1998.

The near-surface wind anomalies are generally easterly or southeasterly over the warm SST anomalies, and the reverse is true over cold anomalies. The maximum magnitude of the effect is $\sim$ 0.4 to 0.6 ms^{-1} K^{-1} in those areas. Convergence tends to occur to the west of the warm SST anomalies, while divergence occurs to the east (Figure 16 shows 2000 as an example). This result supports the vertical mixing hypothesis proposed by Wallace et al. (1989). Although SST anomalies disappear north of 5°N, wind anomalies are observed even at the northern edge of the plot at 8°N, which suggests a link between TIW and the ITCZ. In some years, the wind anomalies at 8°N are even larger than the local response (e.g., 2002 and 2005). The wind anomalies in the Southern Hemisphere can be quite large even though the SST anomalies are small. This response may not be real since the patterns are not consistent from year to year.

Local SST anomalies can affect the boundary-layer water vapor, and enhanced turbulence over warm SST can mix moist air upward. Figure 17 shows the regression of total column water vapor with SST at the reference point. While there are interannual variations in magnitude, the vapor anomalies are generally in phase with the SST anomalies. In each year studied, water vapor anomalies are positive above warm SST anomalies and negative above cold SST anomalies. The water vapor anomalies often extend to 8°N, well beyond

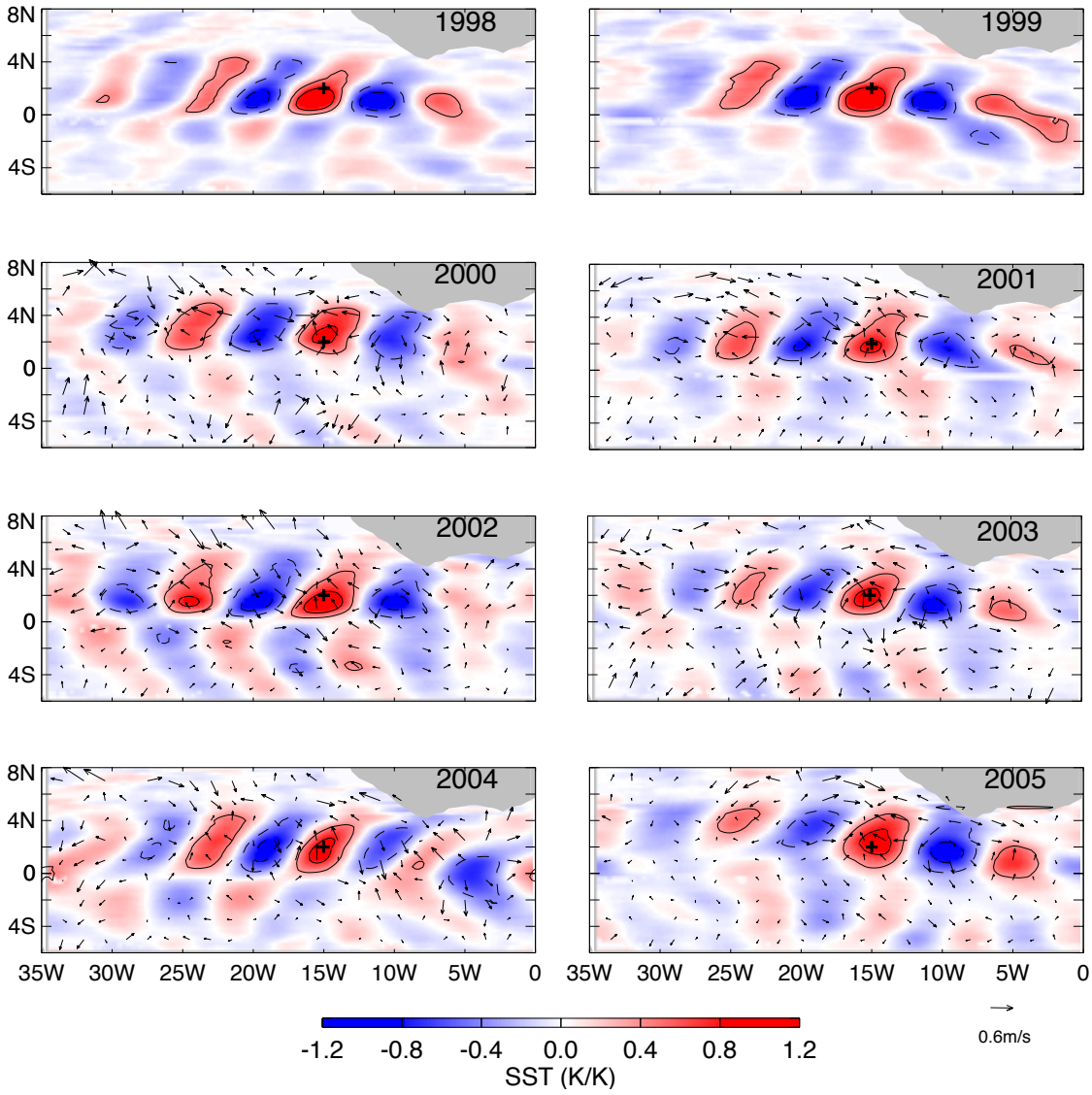

Fig. 14. Regression maps for SST and wind velocity in the period of JJA. The plus represents the reference point (15°W, 2°N) for the regression. The vectors are the wind velocity regressed aganist the reference point. The contours are the SST regression with contour intervals of 0.4K.

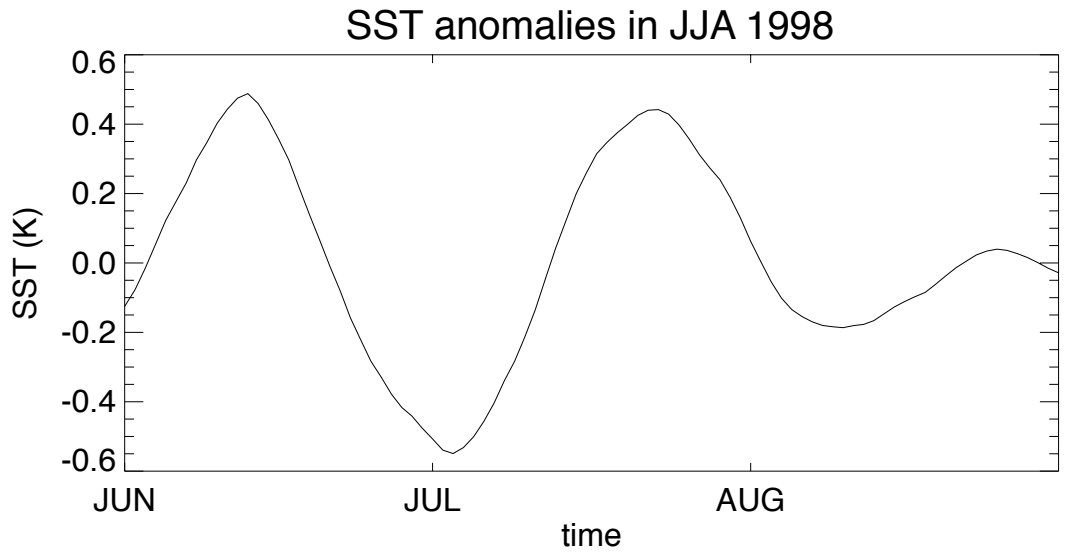

Fig. 15. Time series of SST anomalies in JJA 1998 at the reference point (15°W, 2°N).

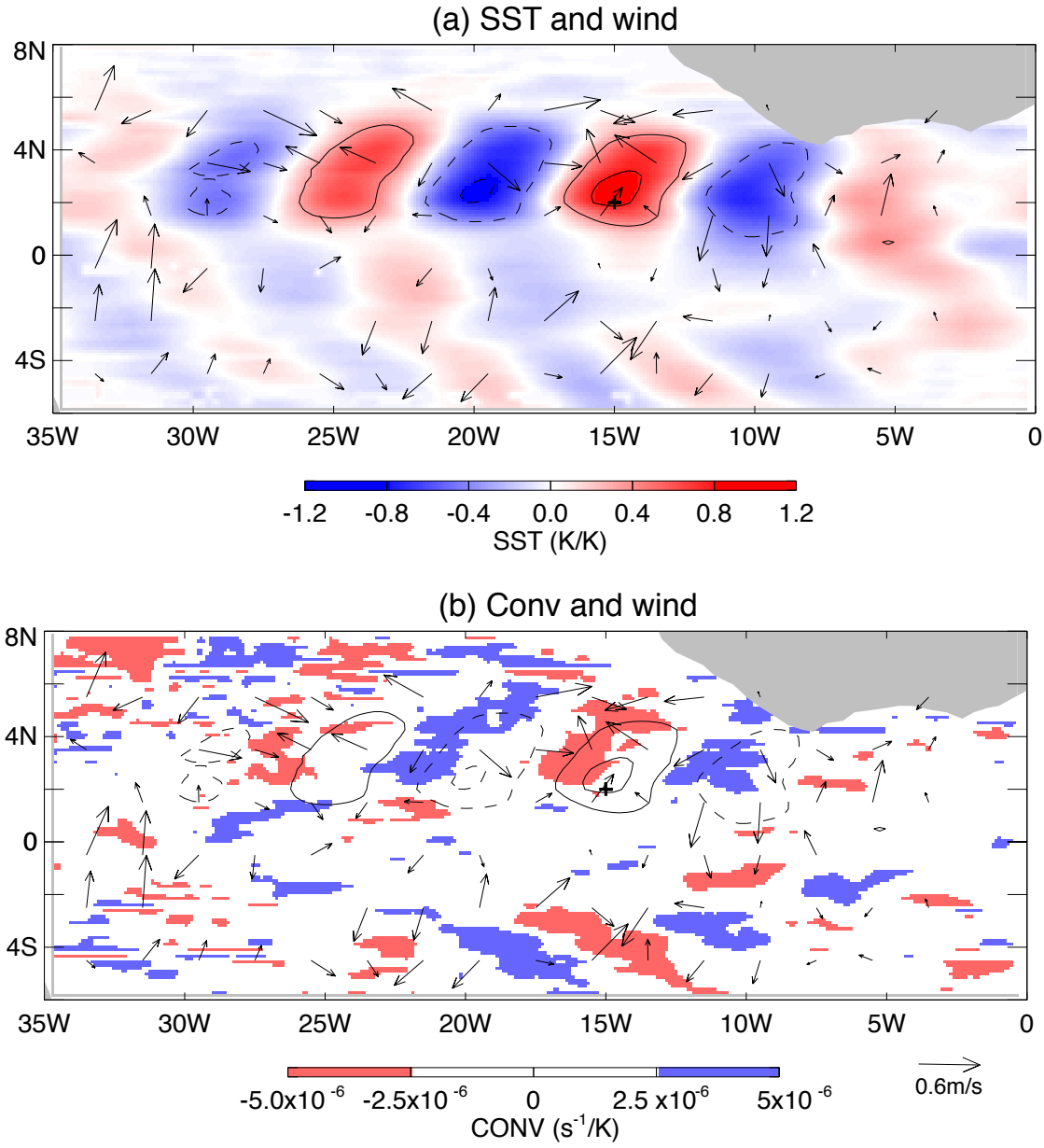

Fig. 16. Regression maps for SST, convergence and wind velocity in the period of JJA in 2000. (a)SST and wind; (b)Convergence and wind. The plus represents the reference point (15°W, 2°N) for regression. The vectors are the wind velocity regressed over the reference point. The contours are SST regression with intervals of 0.4K.

the extent of the SST anomalies. The water vapor anomalies in 2004 are notably weaker than other years. Large water vapor anomalies can also found in the Southern Hemisphere in some years (e.g., 1999 and 2001), although the SST anomalies are weak. Also, water vapor anomalies do not appear to be as antisymmetric about the equator like the SSTs. The water vapor variability induced by TIW SST explains 5$\sim$15% of the total variation.

The cloud liquid water (Figure 18) and rain (Figure 19) regressions are similar to each other, appearing to be roughly downstream from SST anomalies in the central tropical Atlantic. Even though the TIWs are active in latitudes between the equator and 5°N, the cloud liquid water and rain anomalies range from 2°N to 8°N. The cloud liquid water anomalies are accompanied by precipitation changes in the ITCZ. In most years the southern boundary of the Atlantic ITCZ is located at around 4°N. Compared with the Pacific ITCZ, this more southerly position of the Atlantic ITCZ makes it more susceptible to TIW variability. These results reproduce the finding of Hashizume et al. (2001), that during 1999 the TIW variability had a large impact on the deep convection associated with the ITCZ. The results also support the suggestion of Xie et al. (1998), based on a GCM simulation, that TIWs may induce a remote response in the atmosphere and affect the ITCZ that is downstream from the direct forcing of SST waves. The cloud liquid water variability induced by TIW SST anomalies explains 5$\sim$10% of the total variation, while the TIW SST induced precipitation anomalies account for 10$\sim$20% of the total variation. One distinct feature of Figure 19 is that during 1999 the rainfall anomalies are larger than in the other years and extend farther south. During 1999 the regression coefficients for rainfall reach as high as 4 mm day^{-1}K^{-1}. In the latitude between 2°N and 4°N, the TIW SST induced precipitation anomalies account for 20$\sim$30% of the total variation, which is larger than other years. Further diagnosis of this year is presented in the next section.

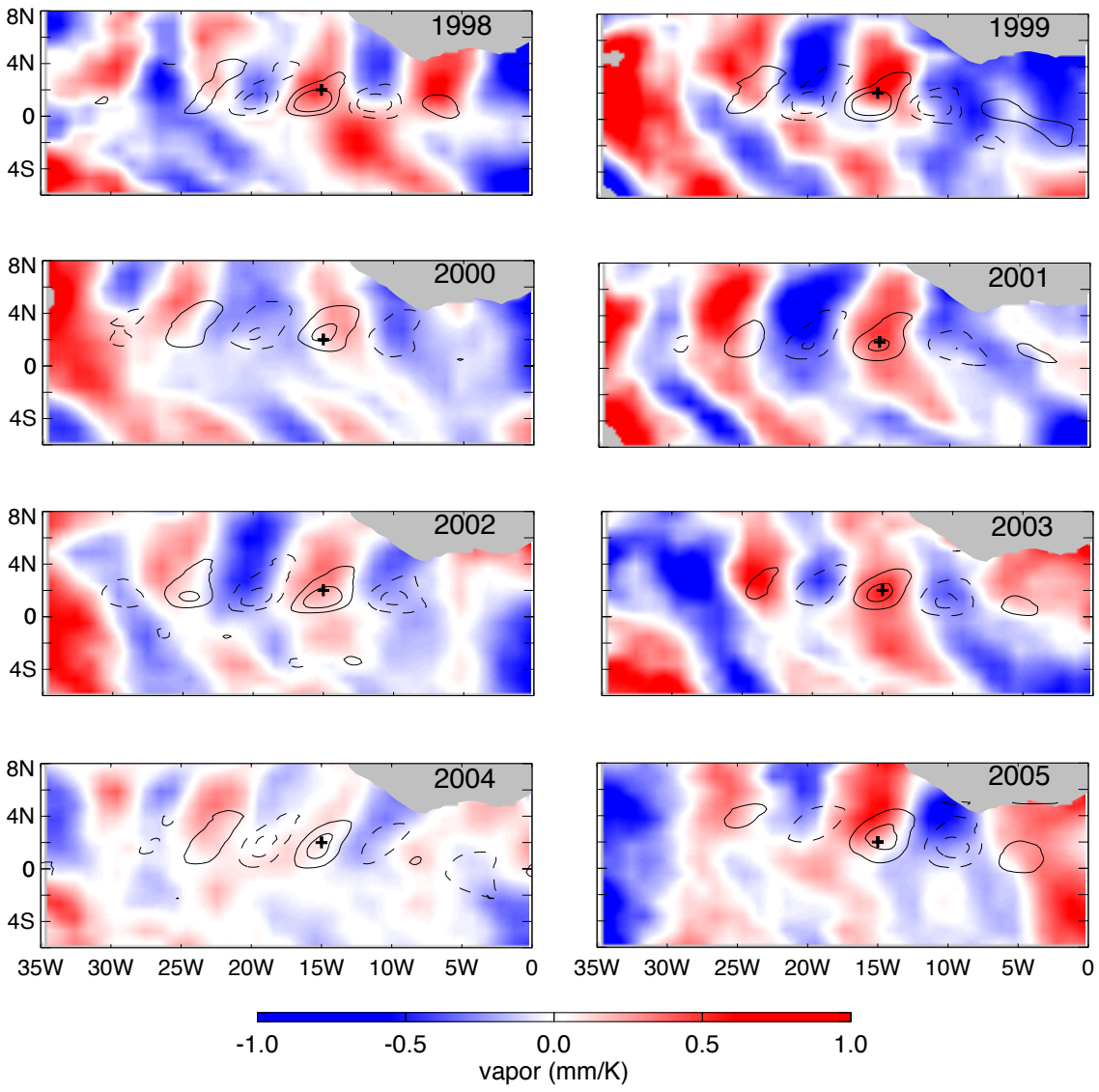

Fig. 17. Regression maps for total column water vapor in the period of JJA. The plus sign represents the reference point (15°W, 2°N) of regressions. The contours are SST regression with intervals of 0.4K.

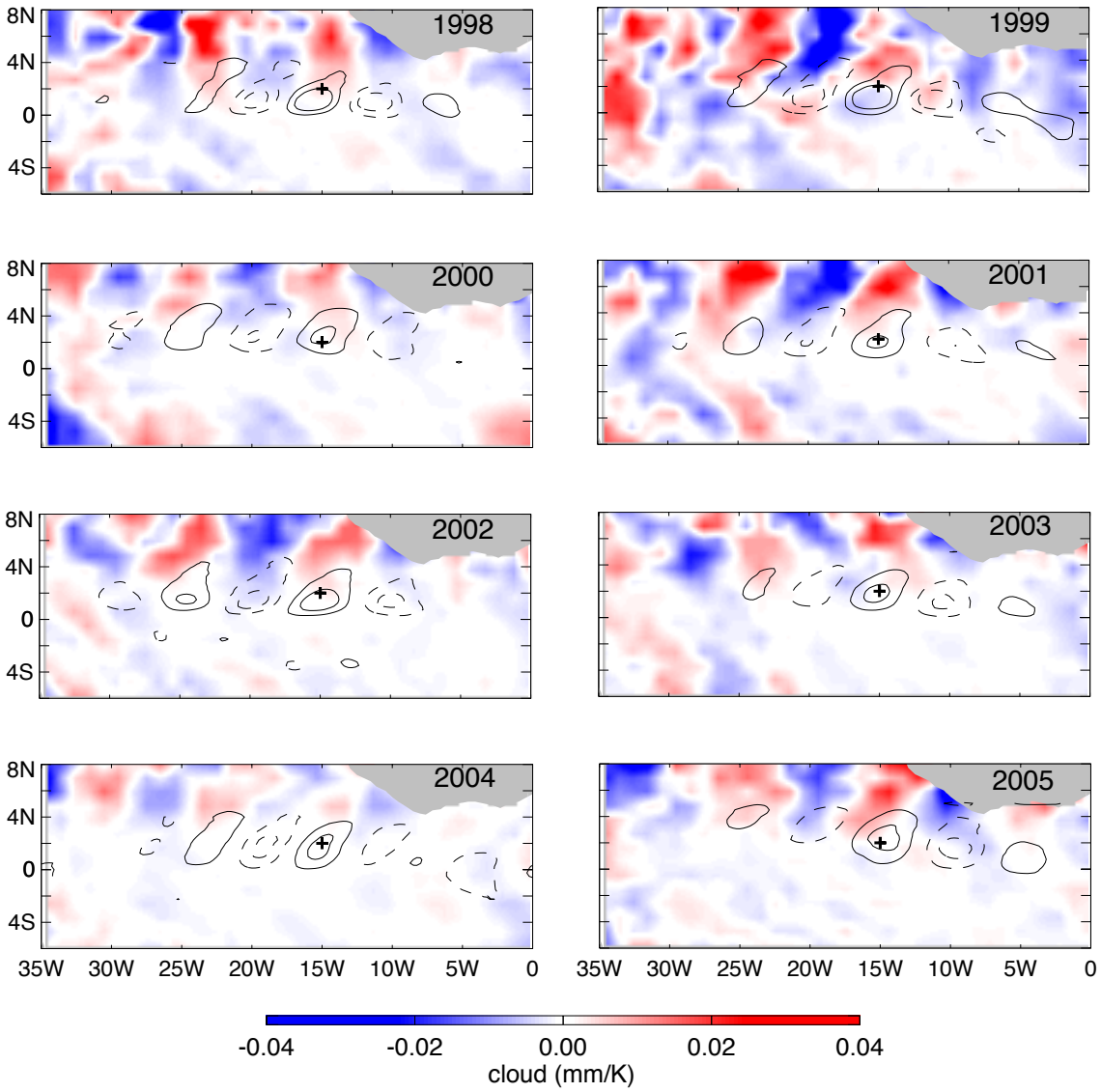

Fig. 18. Regression maps for cloud liquid water in the period of JJA. The plus sign represents the reference point (15°W, 2°N) of regressions. The contours are SST regression with intervals of 0.4K.

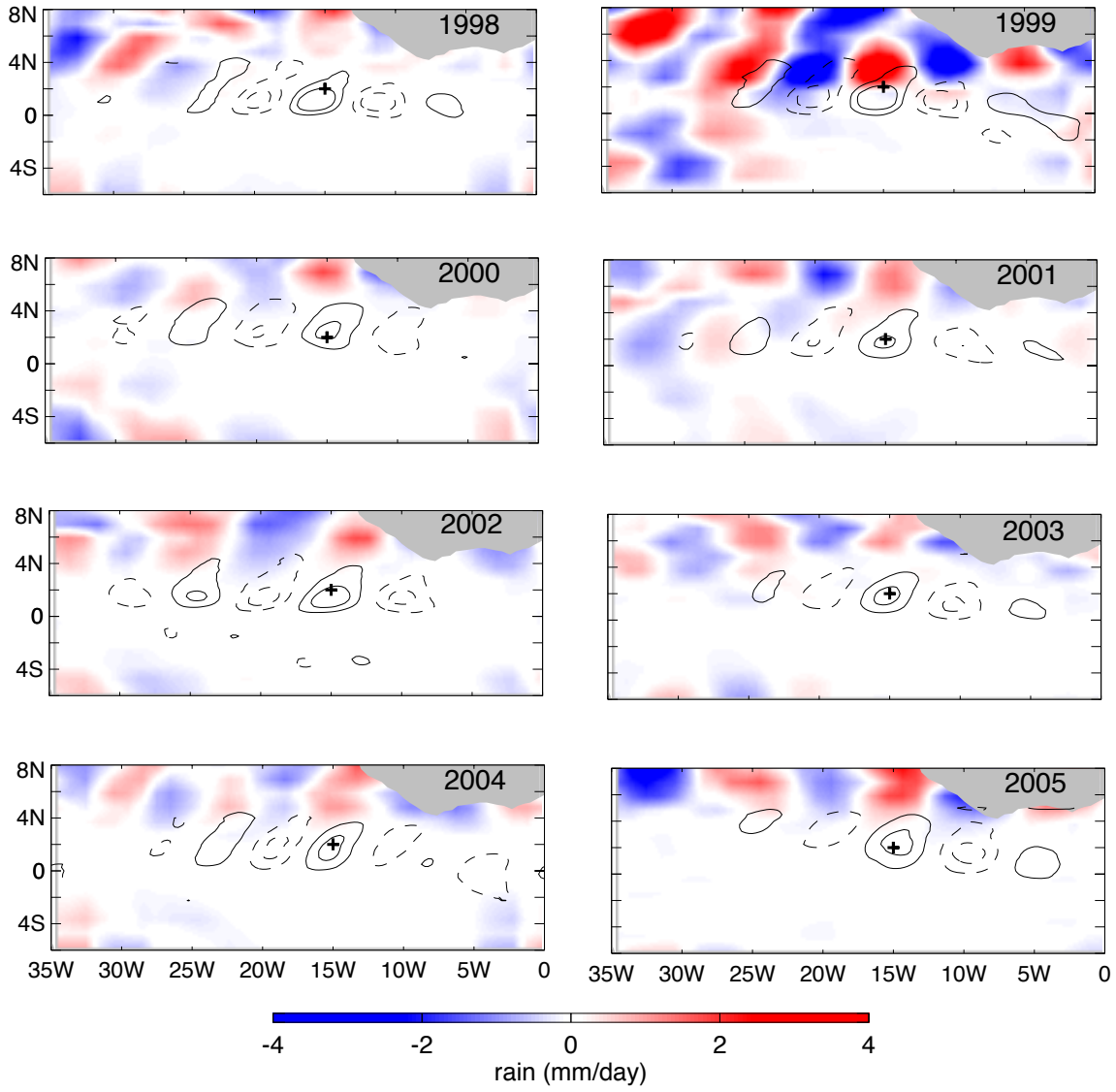

Fig. 19. Regression maps for precipitation in the period of JJA. The plus sign represents the reference point (15°W, 2°N) of regressions. The contours are SST regression with intervals of 0.4K.

B. 1999

As we found in the previous chapter, the Atlantic air-sea coupled mode influences the TIW activity in the Atlantic Ocean. The relationship is similar to that between ENSO and TIWs in the Pacific Ocean. The waves are stronger during cold phases and weaker during warm phases of the coupled mode. The wave activity in 1999, when the coupled mode is in a warm phase, is the weakest in the eight year period from 1998 to 2005. But the rainfall anomalies during 1999 associated with TIWs are much larger than those in all of the other years, particularly between 2°N and 4°N (Figure 19), suggesting that conditions other than the TIW activity must have influenced the atmospheric response to the TIW SSTs.

Figure 20 shows the latitudinal distribution of zonal mean SST, water vapor, cloud liquid water and rain for JJA in the tropical Atlantic. The zonal mean SST in 1999 is about 0.5°C to 1°C higher than other years in the TIW active region (from the equator to 5°N). The zonal mean water vapor shows little variability from 1998 to 2005, although water vapor at 2°N in 1999 is slightly higher than in other years. The zonal mean cloud liquid water at 2°N in 1999 is about 0.08 mm, while in the other seven years, the zonal mean cloud liquid water is 0.03 to 0.04 mm. The zonal mean rain rate at 2°N in 1999 is about 3 mm/day, while in the other seven years, zonal mean rain rates range from 0.1 to 0.7 mm/day. Both the zonal mean cloud liquid water and the rain rate in 1999 are several times larger than other years. Figures 12 and 13 show that the southern Atlantic ITCZ boundary in JJA moves 2° further south during 1999 compared to other years. The comparatively warm temperatures in the TIW region in 1999 increased the precipitation and made the atmosphere more sensitive to TIW variations.

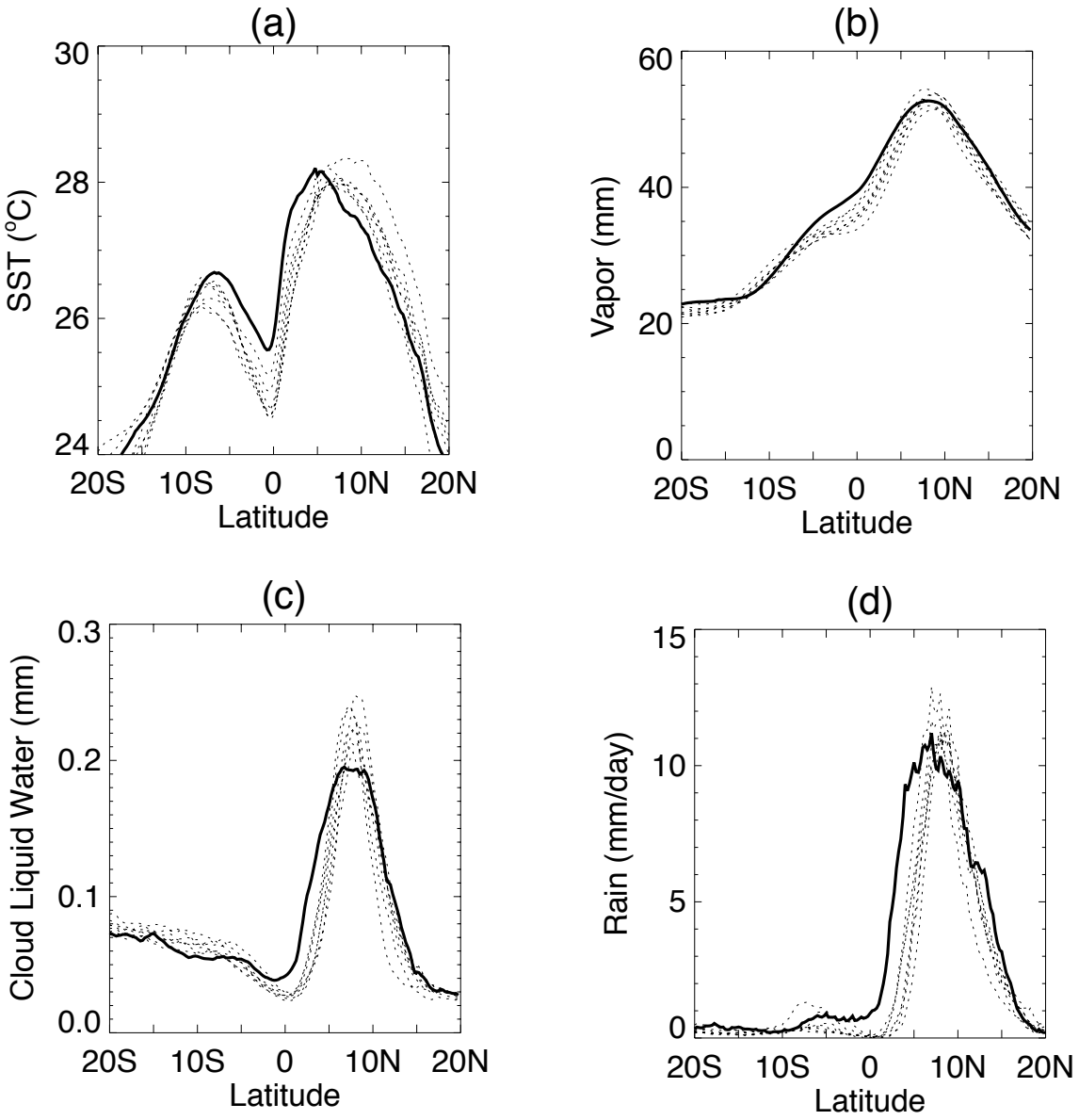

Fig. 20. Zonal mean SST and atmospheric response in the Atlantic Ocean as a function of latitude in the period of JJA in the TIW active region. (a) SST; (b) Water vapor; (c) Cloud liquid water; (d) Rain. Zonal averages are from 5°W to 35°W. The dark line represents the year of 1999.

C. ITCZ Interannual Variability

In this section we discuss how the Atlantic ITCZ location might influence the atmospheric response to the oceanic TIWs. Gu and Adler (2006) show that the ITCZ strength and total rainfall amount in the tropical Atlantic basin are significantly modulated by the Pacific El Niño and the Atlantic Niño, particularly during boreal spring and summer, whereas the impact of the Atlantic interhemispheric mode is considerably weaker. El Niños influence the tropical Atlantic in two distinct ways (Saravanan and Chang 2000; Giannini et al. 2001; Chiang et al. 2002) : (1) by modulating SST in the tropical North Atlantic through the Pacific-North American Pattern (PNA) several months after the tropical Pacific anomalies; and (2) by suppressing rainfall in the equatorial Atlantic via an anomalous Walker circulation and increased stability through widespread tropospheric warming in the tropics,which occurs with a much smaller time lag.

We use 32 years of OLR (from 1974 to 2005) and 24 years of Reynolds SST data (from 1982 to 2005) to study the variability of the Atlantic ITCZ. Figure 21 shows the Atlantic ITCZ as a function of latitude in the period of JJA with OLR and SST data. During the period of JJA in 1999, OLR is colder than any of the other years and SST is as warm or warmer than any other years in the TIW active region (0° and 5°N). By chance, the year that Hashizume et al. (2001) chose to analyze was extreme in terms of Atlantic SSTs and the position of the ITCZ, but 1999 should not be considered as a typical year in terms of the atmospheric response to TIW SST anomalies.

D. Conclusions to Chapter VII

High resolution satellite measurements from TRMM, QuikSCAT and SSM/I are used to study coupled ocean-atmosphere variablity in the equatorial Atlantic from 1998 to 2005. A simple filter and a linear regression technique are applied to the data to extract the charac-

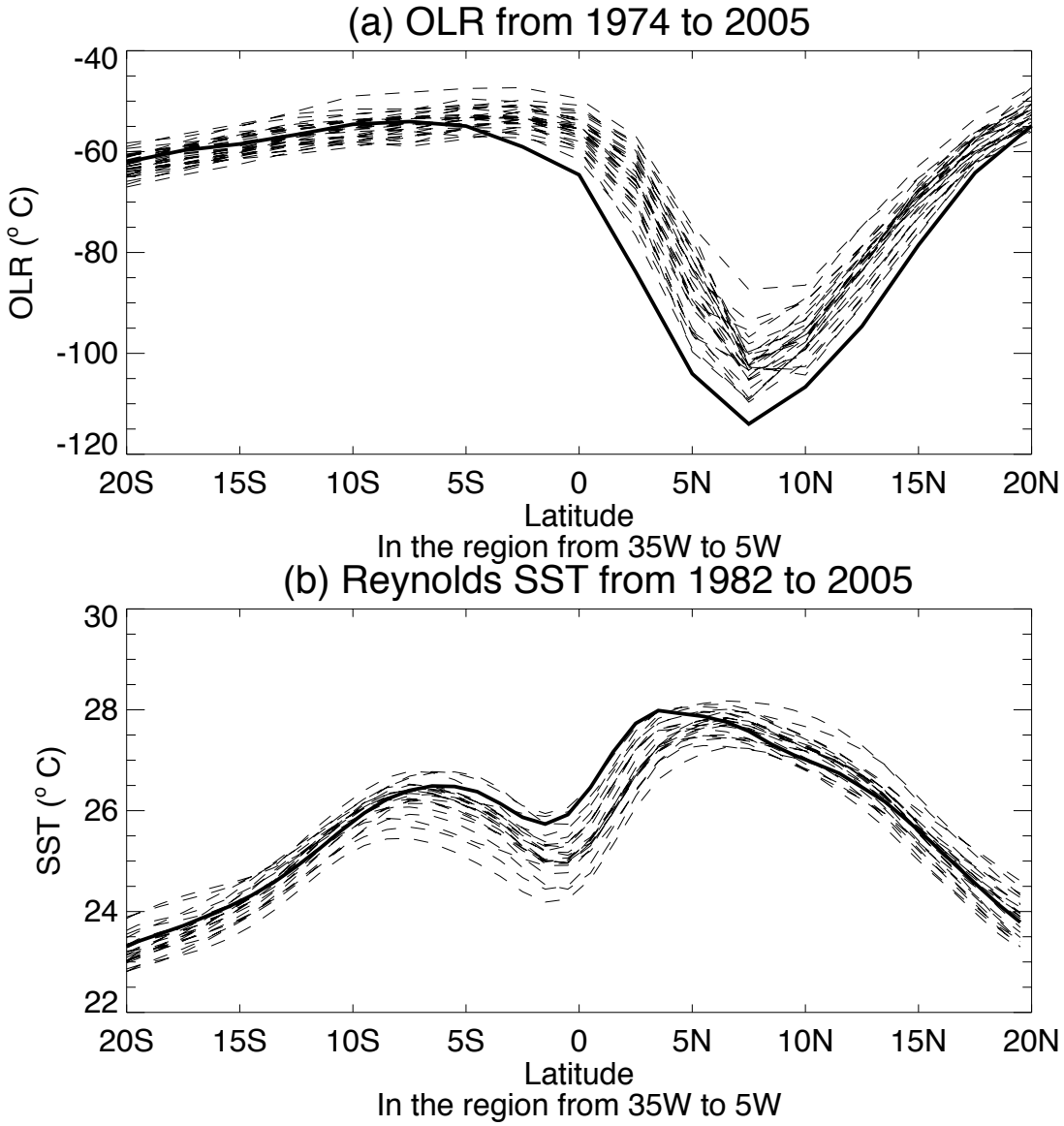

Fig. 21. Zonal mean OLR and SST as a function of latitude in the period of JJA in the TIW active region. (a) OLR from 1974 to 2005 (b) Reynolds SST from 1982 to 2005. Zonal averages are from 5°W to 35°W. The solid lines represents the ITCZ in 1999.

teristics of the atmospheric response to the SST anomalies in TIWs. The highly coherent patterns from our analysis indicate that current satellite technologies are capable of detecting interseasonal changes in atmospheric variable, including precipitation, even within the noisy ITCZ.

Coherent ocean-atmosphere patterns appear from 1998 to 2005. Although TIWs are active in the equatorial oceans, their atmospheric response extends farther north and reaches the ITCZ. Southeasterly trades strengthen over warm SST anomalies associated with TIWs and weaken over cold SST anomalies. Wind anomalies have an amplitude of $0.4\sim0.6$ ms^{-1} K^{-1} at 2°N. The water vapor variability induced by TIW SST anomalies explains $5\sim15\%$ of the total variation. Cloud liquid water and rainfall responses to the TIW SST follow a very similar pattern, appearing to be roughly in phase with SST anomalies. The TIW SST induced cloud liquid water anomalies account for $5\sim10\%$ of the total variation and precipitation anomalies account for $10\sim20\%$ of the total precipitation variation.

The atmospheric responses to the SST TIWs extend to 8°N, which is north of the principal TIW activity zone, suggesting a remote downstream response to the TIW SST anomalies. The atmospheric responses to these TIWs show interannual variability. In 1999, the rainfall response to TIWs in the latitude between 2°N and 4°N is much larger than those in other years, which we attribute to the anomalously warm SSTs at 2°N and the southward movement of Atlantic ITCZ in that year. When the ITCZ takes a more southerly position, the synoptic variability in precipitation can be larger than the long-term mean. As the Atlantic ITCZ moves south, it is more susceptible to TIW influence.

CHAPTER VIII

NUMERICAL SIMULATIONS WITH MM5

How the atmosphere responds to the SST changes is important for climate variability in the Atlantic Ocean. Current research on large-scale ocean-atmosphere interaction has focused on ENSO phenomena in the tropical Pacific, a process limited to high-SST regions. Most of the ocean in the world is not warm enough to support deep convection. TIWs thus provide an opportunity for studying the atmospheric response to relatively cool sea surface temperatures. One obvious question about TIWs is whether TIW-induced perturbations of wind field have a significant feedback onto the ocean circulation. Pezzi and Richards (2004) showed that the wind perturbations have a negative feedback that tends to reduce the SST and meridional velocity signatures of TIWs. This, in turn, reduces equatorward eddy heat flux associated with TIWs, thereby resulting in intensified cooling of the equatorial cold tongue. This negative feedback has potentially important implications about the role of TIWs in climate variability. High-resolution numerical models are necessary to further explore the mechanisms of ocean-atmosphere interaction associated with TIWs.

Compared with the tropical Pacific, our current understanding of air-sea feedback mechanisms in the tropical Atlantic is very limited. To our knowledge, there are no numerical modeling studies concerning the planetary boundary layer (PBL) response to TIWs in the Atlantic Ocean.

A. Hypothesis Test

We did two numerical simulations of the 2000 TIW season with MM5 to study the coupling of SST and atmospheric fields. The first run, referred to as the control run, uses monthly SSTs. In the second run, referred to as the TIW run, the model was forced with daily SSTs. We expected little or no TIW signal in the atmosphere fields with monthly SST forcing.

The 20-40 day TIW signals are largely absent in the monthly SST data.

The westward propagation of TIWs in SST, air temperature, and zonal and meridional wind at 995 hpa at selected latitudes is illustrated in longitude-time sections in Figure 22 and Figure 23. In the control run, there is little evidence of wave signals in the atmosphere field, while in the TIW run, air temperature, zonal and meridional winds all show strong westward-moving signals. This demonstrates that atmospheric variations are coupled to TIW variability in the model. SST has maximum variance at 2°N, while zonal and meridional wind has maximum responses at 5°N. In Figure 23 SST shows a strong TIW signal from June to September, while the atmosphere responses are strong in July and August.

B. Background of Model Simulation

The surface wind and the relationship with underlying SST from both observations and the model are shown for a typical day of the TIW season in Figure 24. A clear wave pattern is seen in the SST field. The southeast and northeast trade wind regimes are seem in both model and observations. Winds converge near 10°N over the warmest water. The major difference between the model and observation in the wind field is that the wind vectors are much weaker in the model simulation over warm water from 7°N to 15°N.

The mean rain rates in the JJA period of 2000 from observations and model are shown in Figure 25. The model produces an ITCZ, although in the Atlantic the ITCZ is weaker and broader than than the observations. The model over-estimates the rain rate in the subtropical and extratropical Atlantic. Although the simulation of the ITCZ is imperfect, we judge it to be good enough for further analysis.

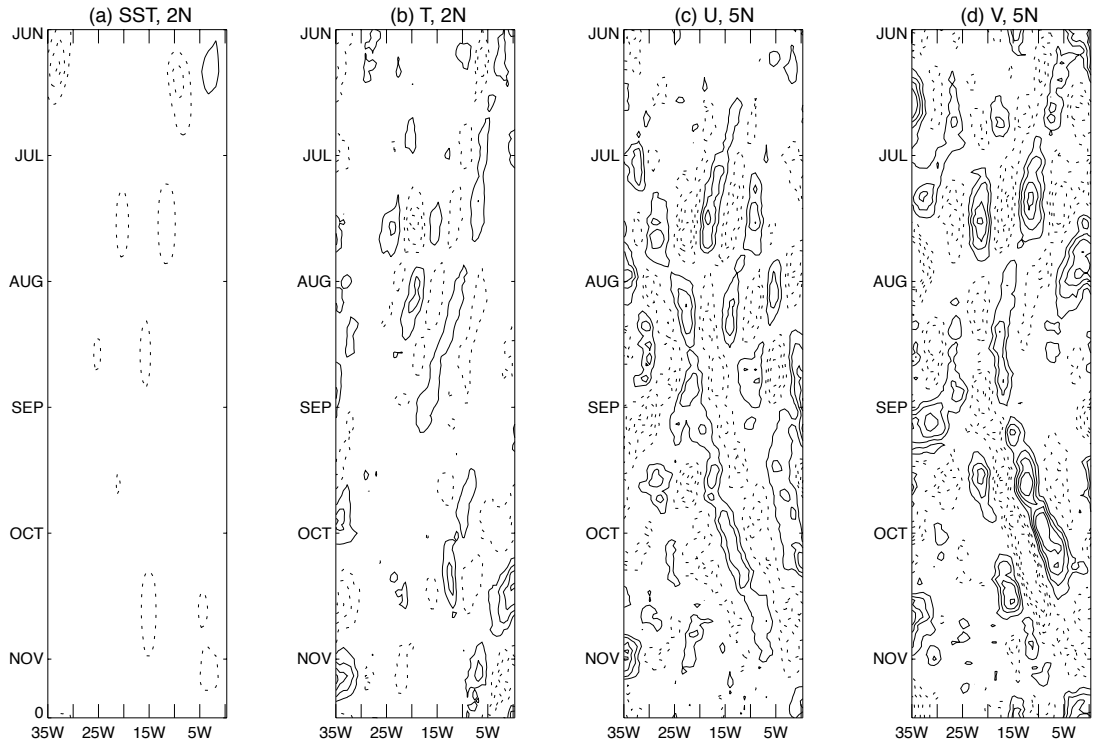

Fig. 22. Longitude-time distribution of monthly SST, air temperature and surface wind from the control run. (a)monthly SST with interval 0.05K; (b) air temperature at 995 mb with interval 0.05K; (c) U at 995 mb at with interval 0.05m/s; (d)V at 995 mb with interval 0.05 m/s.

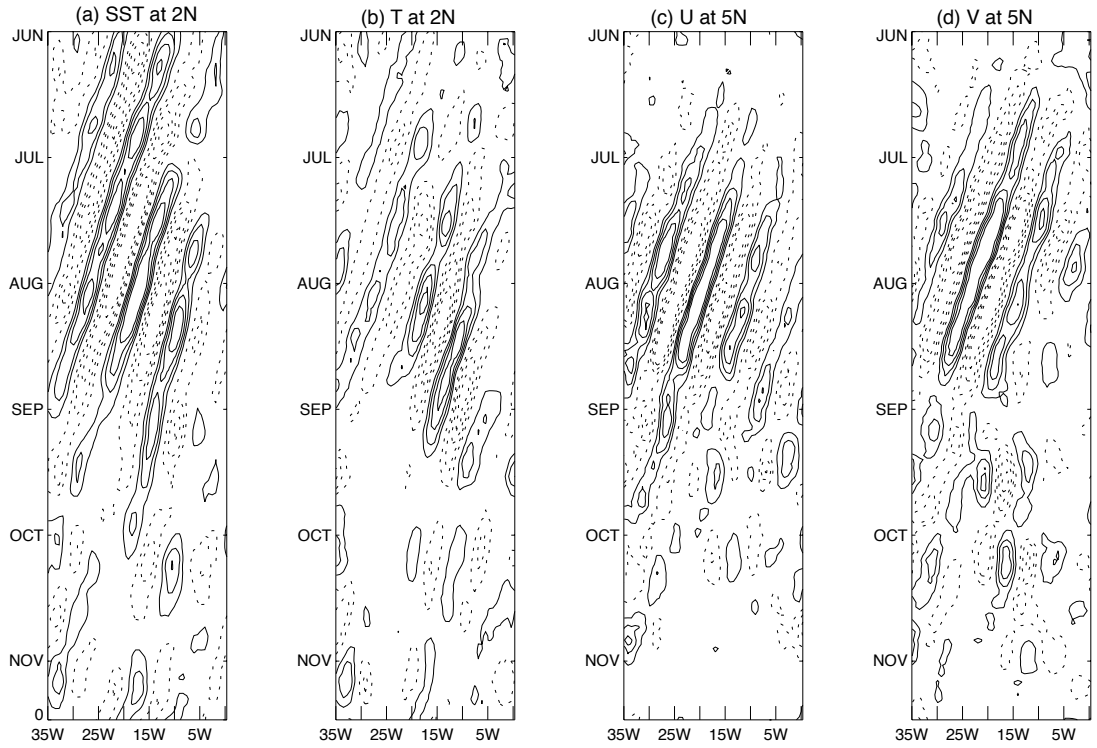

Fig. 23. Longitude-time distribution of daily SST and air temperature, surface wind from the daily SST run. (a)daily SST with interval 0.1K; (b) air temperature at 995 mb with interval 0.1K; (c) U at 995 mb at with interval 0.1m/s; (d)V at 995 mb with interval 0.1 m/s.

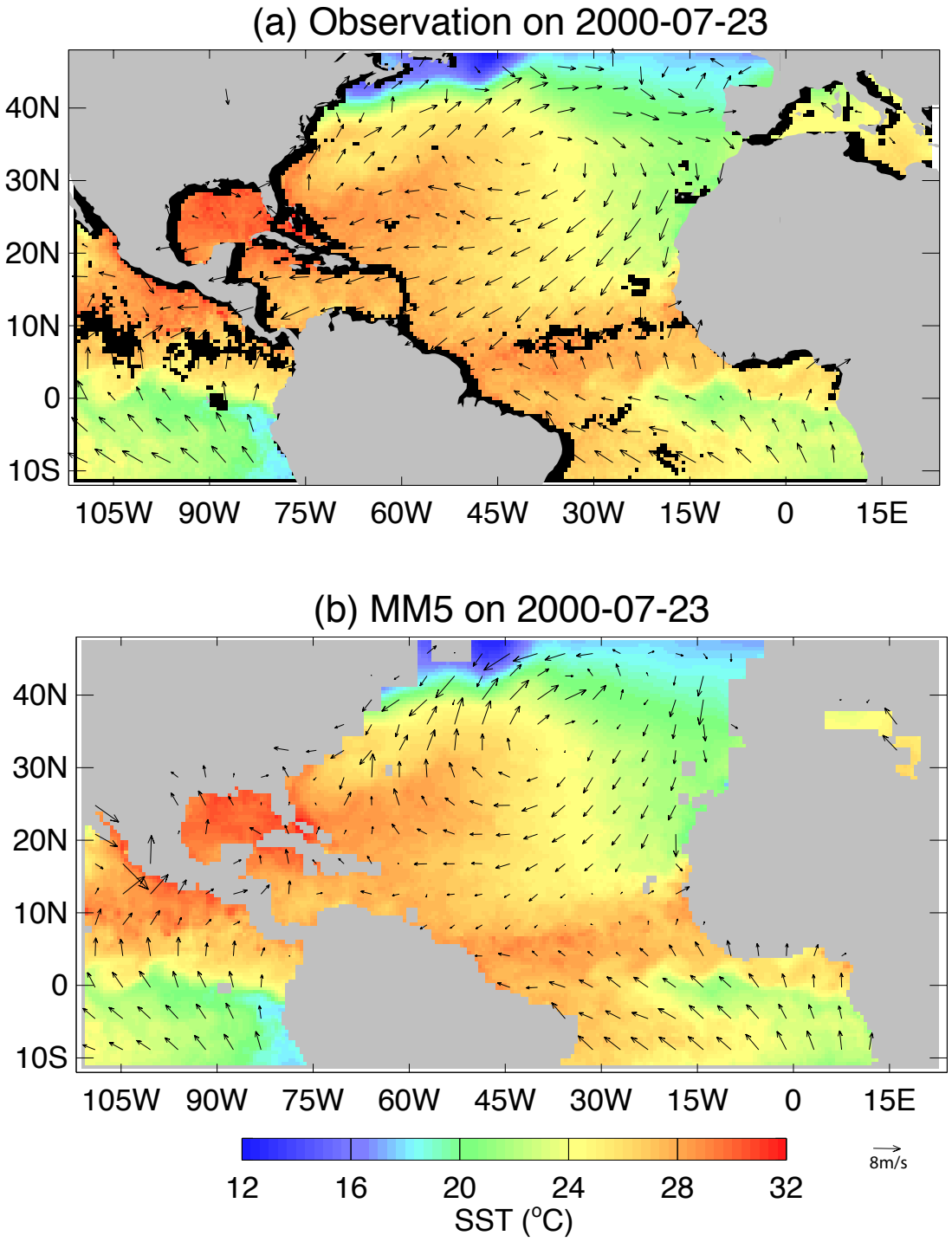

Fig. 24. SST and surface wind vector over the MM5 model domain ended on 2000-07-23. (a) SST from TMI and surface winds from QuikSCAT; (b) interpolated SST data for model simulation and modeled surface winds. Missing SST data are shown in black.

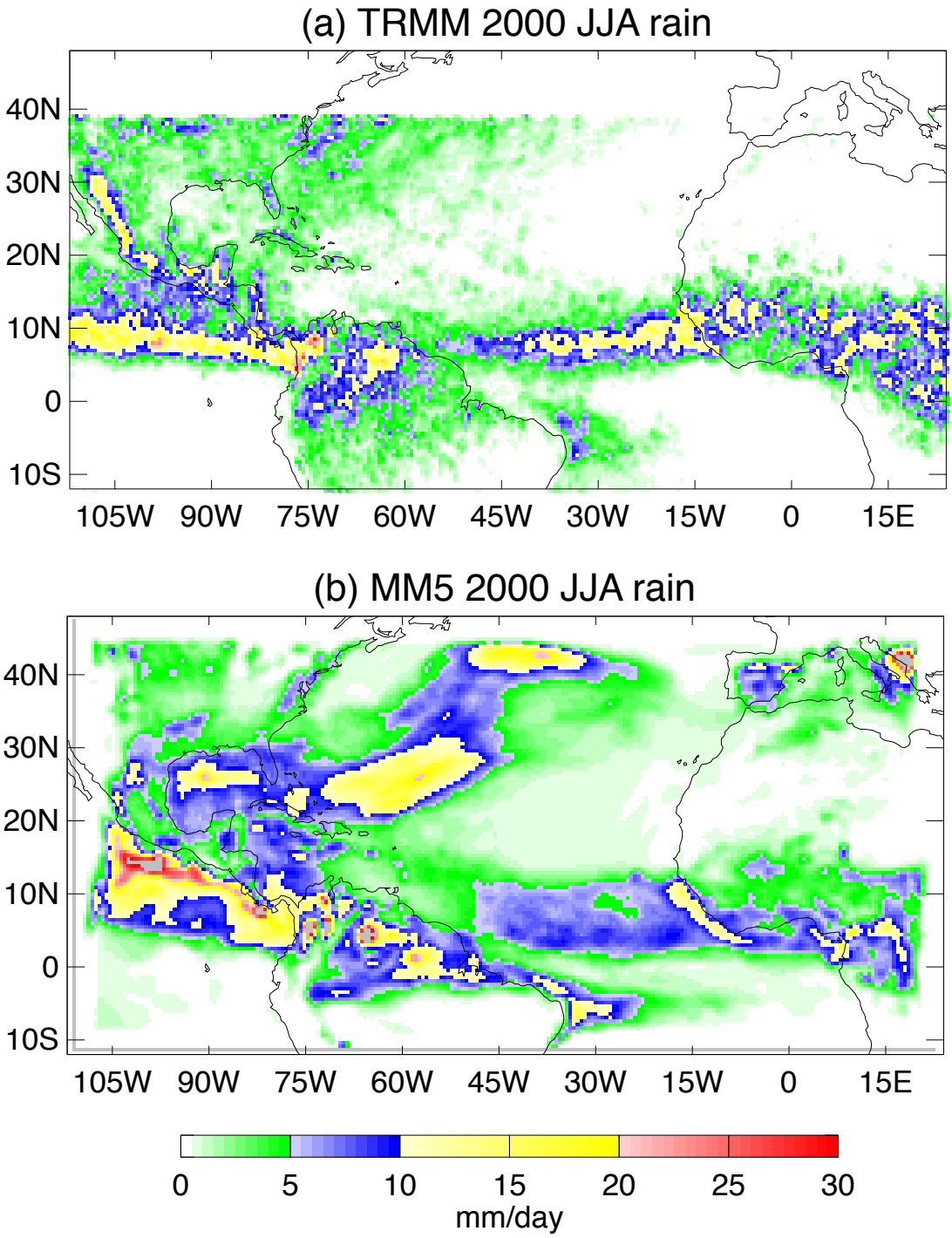

Fig. 25. Rain rate over the model domain in the period of JJA, 2000. (a) Observed rain rate from 3B42 rain rate data; (b) modeled rain rate.

C. Horizontal Structure

The effects of TIWs on the surface winds can be seen by filtering and regressing atmospheric variables against SSTs as described in section 2c. The reference point chosen is (15°W, 2°N), where SSTs have their maximum variance. Figure 26(a) shows the patterns of regressed SST and wind vector at 10 m from the QuikSCAT satellite on one day 2000. A clear TIW wave structure is seen at latitudes between 1°N and 5°N in the SST regression with a wavelength about 10 degree longitude. The regression patterns tilt slightly eastward as latitude increases. The TIW patterns in the SST regression are not symmetric about the equator; the southern TIWs are much weaker. Southeasterly winds strengthen over warm SST anomalies and weaken over cold SST anomalies. Winds converge west of warm SST anomalies and diverge west of cold SST anomalies. Wind anomalies can be large in the southern Atlantic, even though, SST anomalies are small. Wind anomalies can reach as far as 8°N, although the SST anomalies disappear north of 5°N, which suggests that TIWs might influence the ITCZ (Hashizume et al. 2001).

Figure 26(b) shows the model-simulated wind regression vectors over the SST. The model wind vector patterns are similar to the observations in many aspects. There are wind perturbations north of 5°N, where SST anomalies disappear. Compared to the observations, the convergence and divergence from the model are more in phase with SSTs. The wind response appears to be weaker in the Southern Hemisphere in the model than in the observations. In the previous chapter, we did not find a consistent pattern of wind response to the TIW SST in the Southern Hemisphere, which suggests the wind response in the South Hemisphere might not be real.

Figure 27 shows the convergence, column-intergrated water vapor and rain response to TIW SSTs from satellite observations. From the observation, the wind convergence and divergence are located west of warm SST anomalies and cold SST anomalies. This result

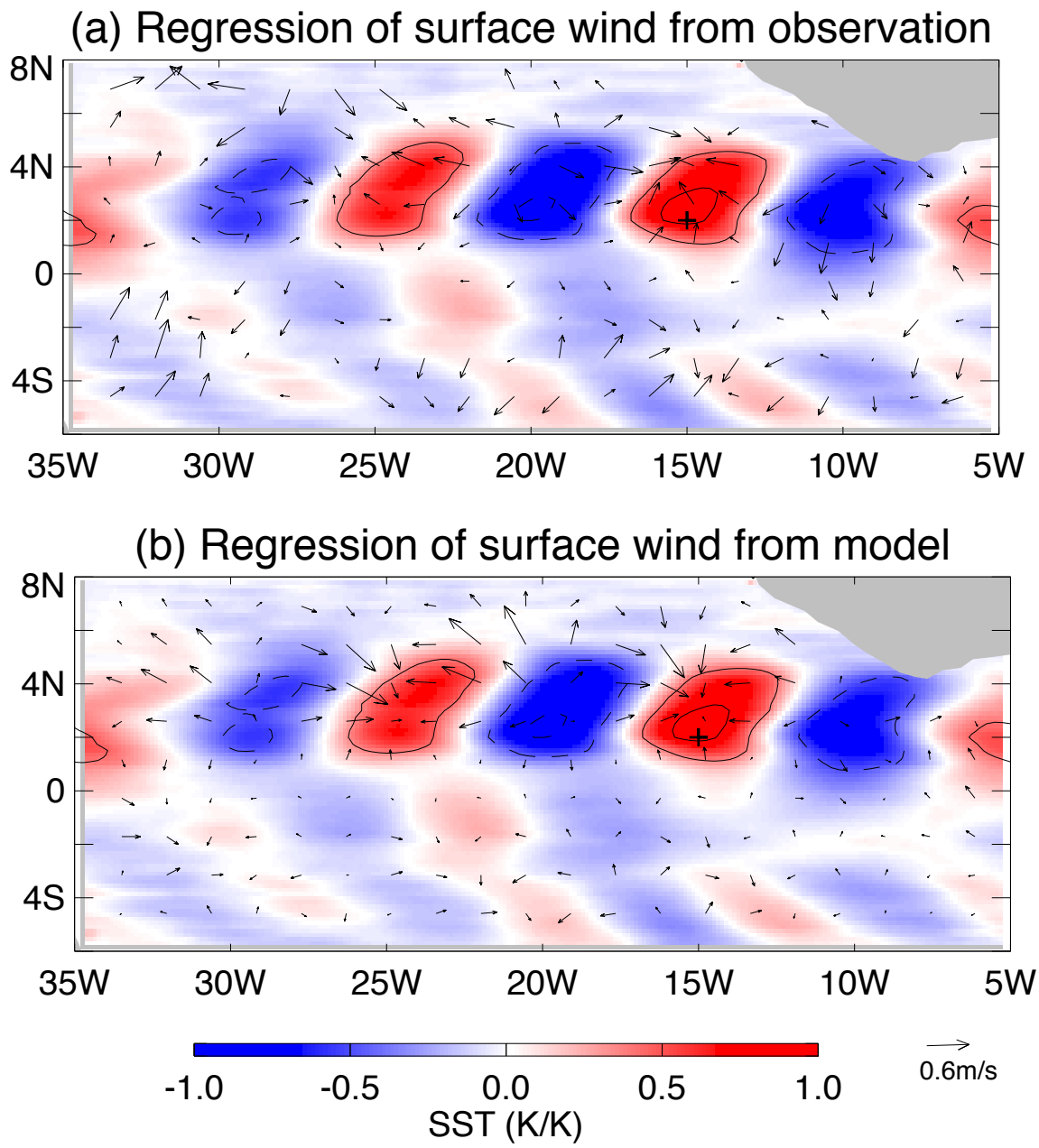

Fig. 26. Regression maps for SST and wind velocity in the period of JJA. (a) Observations from TMI and QuikScat; (b) Model simulation. The plus represents the reference point (15°W, 2°N) for regression. The contours are SST regression with intervals of 0.4K.

agrees with Figure 26(a) in the wind fields. The vapor anomalies are generally in phase with the SST anomalies. Water vapor anomalies are positive above warm SST anomalies and negative above cold SST anomalies. The water vapor anomalies often extend to 8°N, well beyond the extent of the SST anomalies. Even though the TIWs are active in latitudes between the equator and 5°N, the rain anomalies range from 2°N to 8°N in 2000. The remote response of rain to TIWs is a special feature of the Atlantic Ocean (Hashizume et al. 2001).

Figure 28 shows the convergence, mixing ratio and rain response to TIW SSTs from the model simulation. In the model, the wind convergence and divergence are located downstream of the SST anomalies. The amplitude of the convergence response in the model is 2$\sim$3 time of the observation. The mixing ratio response is downstream of the SST anomalies as well. The amplitude of the rainfall response is about the same order as in the observations, the remote response feature is also shown in the model.

The near-surface air temperature regressions in Figure 29 reach a magnitude of 0.6 K/K and -0.4K/K. The extremes are located slightly downstream of the SST extremes. The wind anomalies converge from surface pressure minima and diverge into surface pressure maxima. This result suggests that the anomalous pressure gradient is an important factor in addition to vertical mixing. The magnitude of the surface pressure anomaly reaches 15 Pa/K. The high and low pressure anomalies do not occur directly over low and high SST anomalies, but somewhat downstream. These results agree with the results of Small et al. (2003) in the Pacific. As discussed in Small et al. (2003), the downstream location of surface pressure minima relative to the SST maxima is due to the downstream displacement of the air temperature and relative humidity.

The TIW SST anomalies force a response of the sensible and latent heat fluxes (Figure 30). The latent heat flux anomalies induced by the TIW SSTs are larger than the sensible heat flux anomalies. Maximum heat flux anomalies are located very close to the maximum

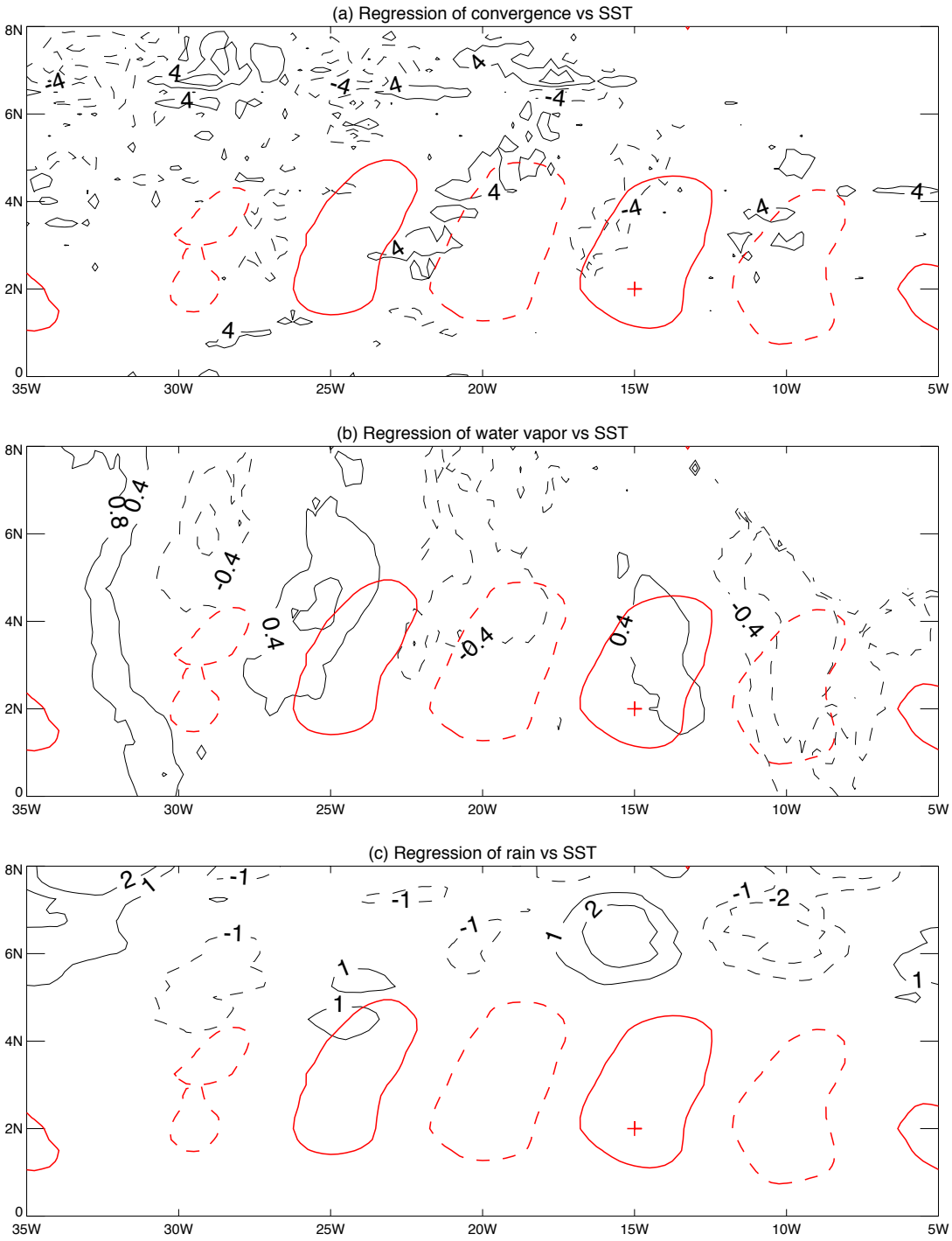

Fig. 27. Regression maps for surface wind convergence, column-integrated water vapor and rain from observations. (a) Surface wind convergence; (b) Column-intergrated water vapor; (c)Rain. The plus represents the reference point (15°W, 2°N) for regression. Red lines are contours of SST regression with intervals of 0.4K.

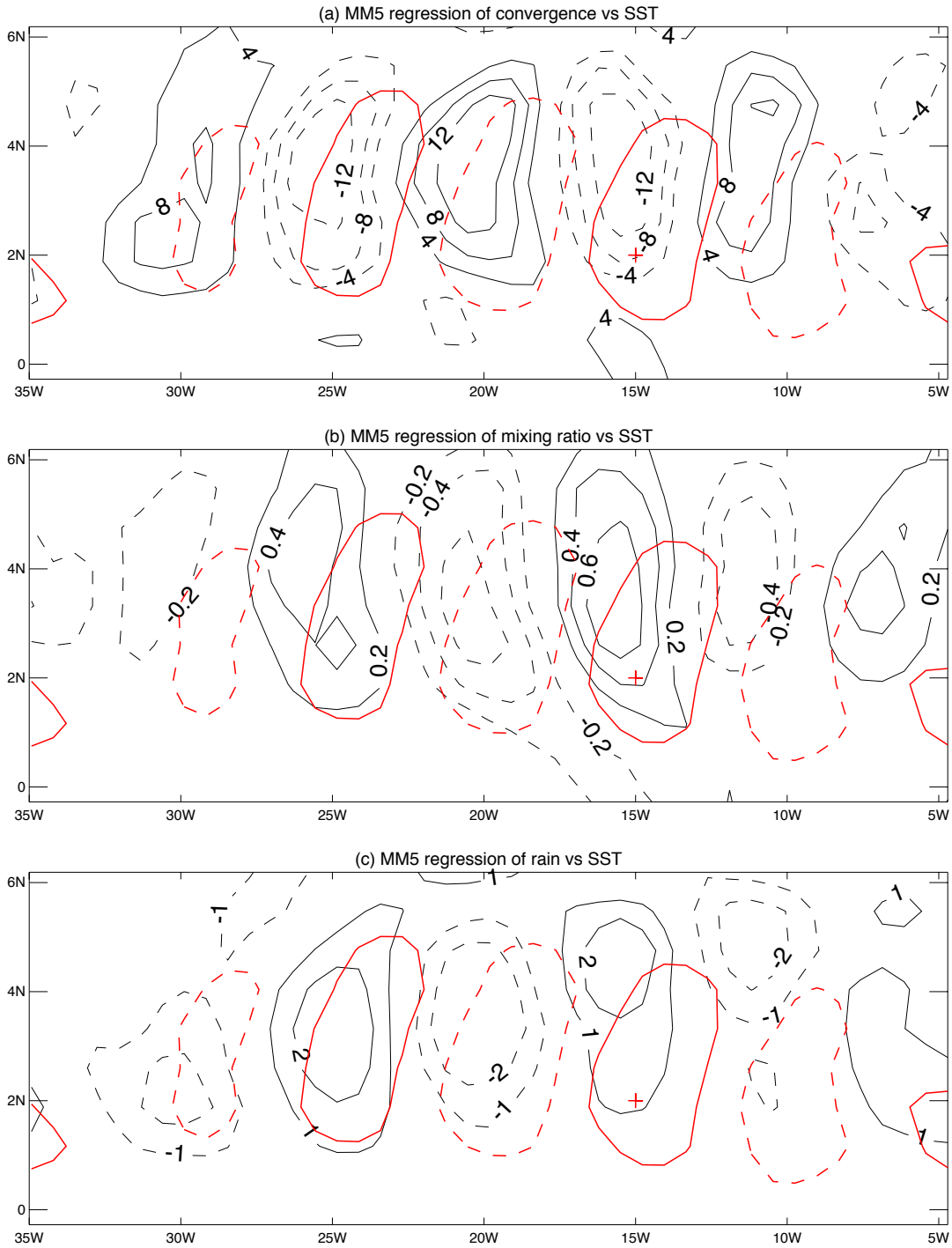

Fig. 28. Regression maps for surface wind convergence, mixing ratio and rain from model. (a) Surface wind convergence; (b) Mixing ratio; (c)Rain. The plus represents the reference point (15°W, 2°N) for regression. Red lines are contours of SST regression with intervals of 0.4K.

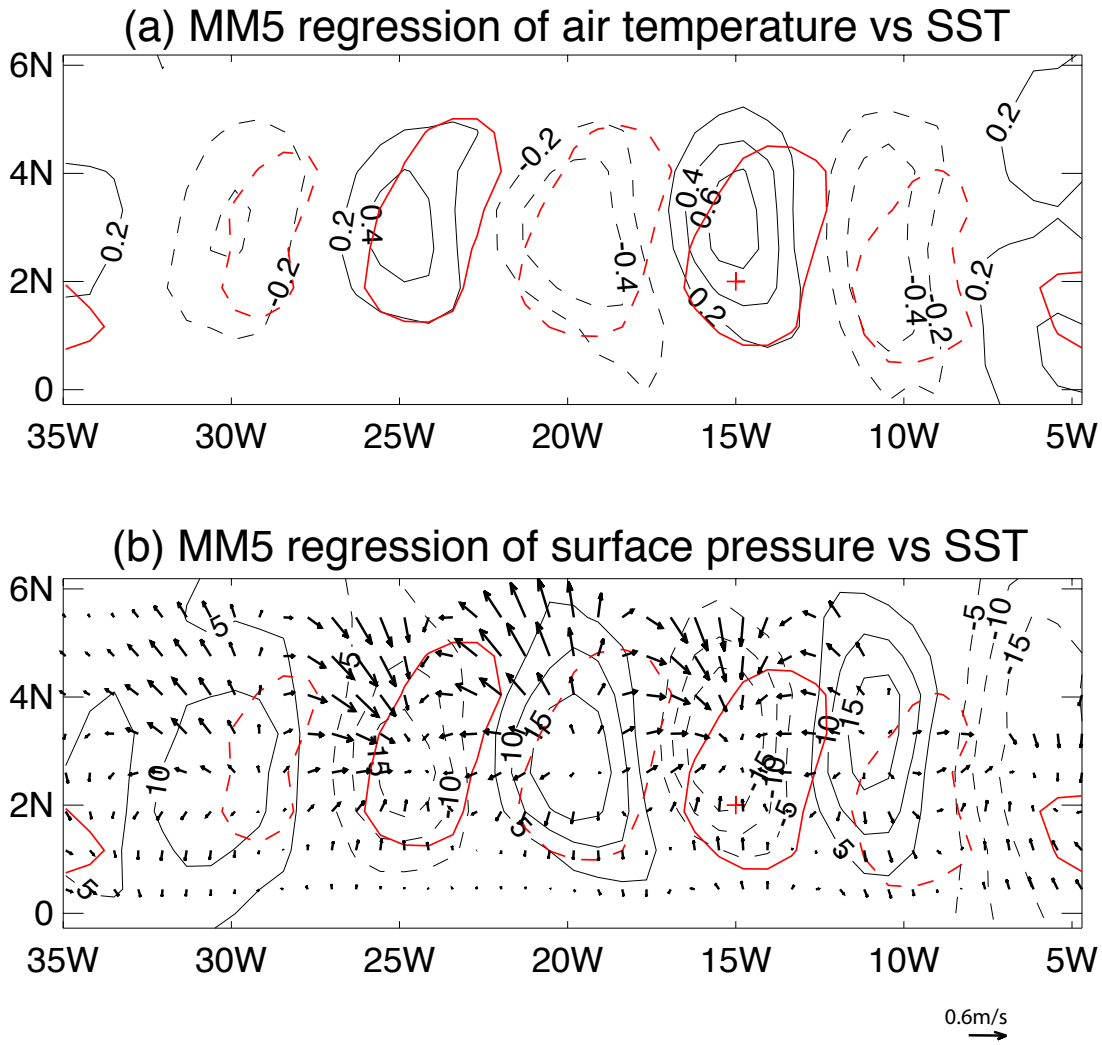

Fig. 29. Regression maps for air temperature, surface pressure and wind velocity from model. (a) Air temperature at lowest model level; (b) Surface pressure and surface wind. The plus represents the reference point (15°W, 2°N) for regression. Red lines are contours of SST regression with intervals of 0.4K.

SST anomalies. That is, over warm SST anomalies, TIWs release heat to the atmosphere and over cold SST anomalies, TIWs absorb heat from the atmosphere.

The SST anomalies also force a response in the convective and resolved rain (Figure 31). The convective rain anomalies induced by TIW SST are $\sim$10 time the resolved rain anomalies. As with the surface pressure, the convective rain anomalies do not occur immediately over the low and high SST anomalies, but are shifted downstream. The resolved rain anomalies occur between 5°N and 7°N, where SST anomalies are absent. The resolved rain shows a remote response to the TIW SSTs.

D. Vertical Structure

The vertical structure of the atmospheric response to the TIW SST variations at 2°N and variable profiles over warm and cold SST are shown in Figures 32 and 33. Cold and warm composite profiles are shown in the right-hand panels of the two figures. The warm profile is computed by adding the regression profile at a positive SST regression at 2°N (16°W here) to time-mean profile at 15°W,2°N. The cold profile defined as adding regression profile at negative SST regression at 5°N (21°W here) to time mean profile at 15°W,2°N.

The vertical structure of the regression coefficient of air temperature can be seen in Figure 32a. The regression coefficient reverses sign above $\sigma = 0.9$, and temperature perturbations are limited to altitudes below $\sigma = 0.825$ (around 1500m). Since pressure anomalies are inversely related to air temperature, pressure anomalies reverse sign above $\sigma = 0.9$. This process sets up a thermally direct circulation cell, which affects the wind velocities and water vapor.

Figure 32b shows the vertical structure of the regression coefficient for U. Negative surface anomalies of U lie to the east of warm SST and positive anomalies of U lie to the east of cold SST. There is about 90° phase shift between surface anomalies of U and SST

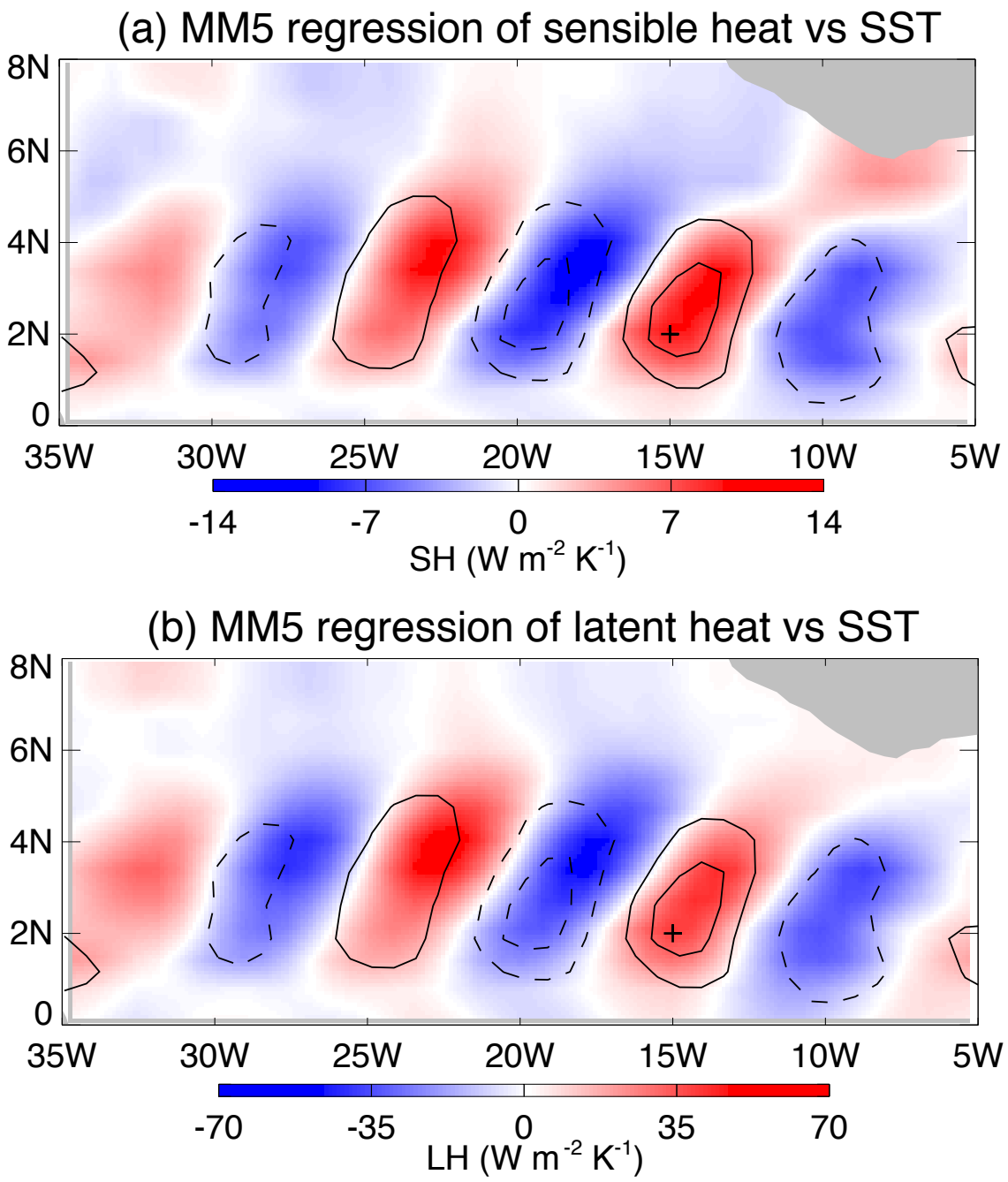

Fig. 30. Regression maps for heat from model. (a) Sensible heat; (b) Latent heat. The plus represents the reference point (15°W, 2°N) for regression. Red lines are contours of SST regression with intervals of 0.4K. Note difference in scales.

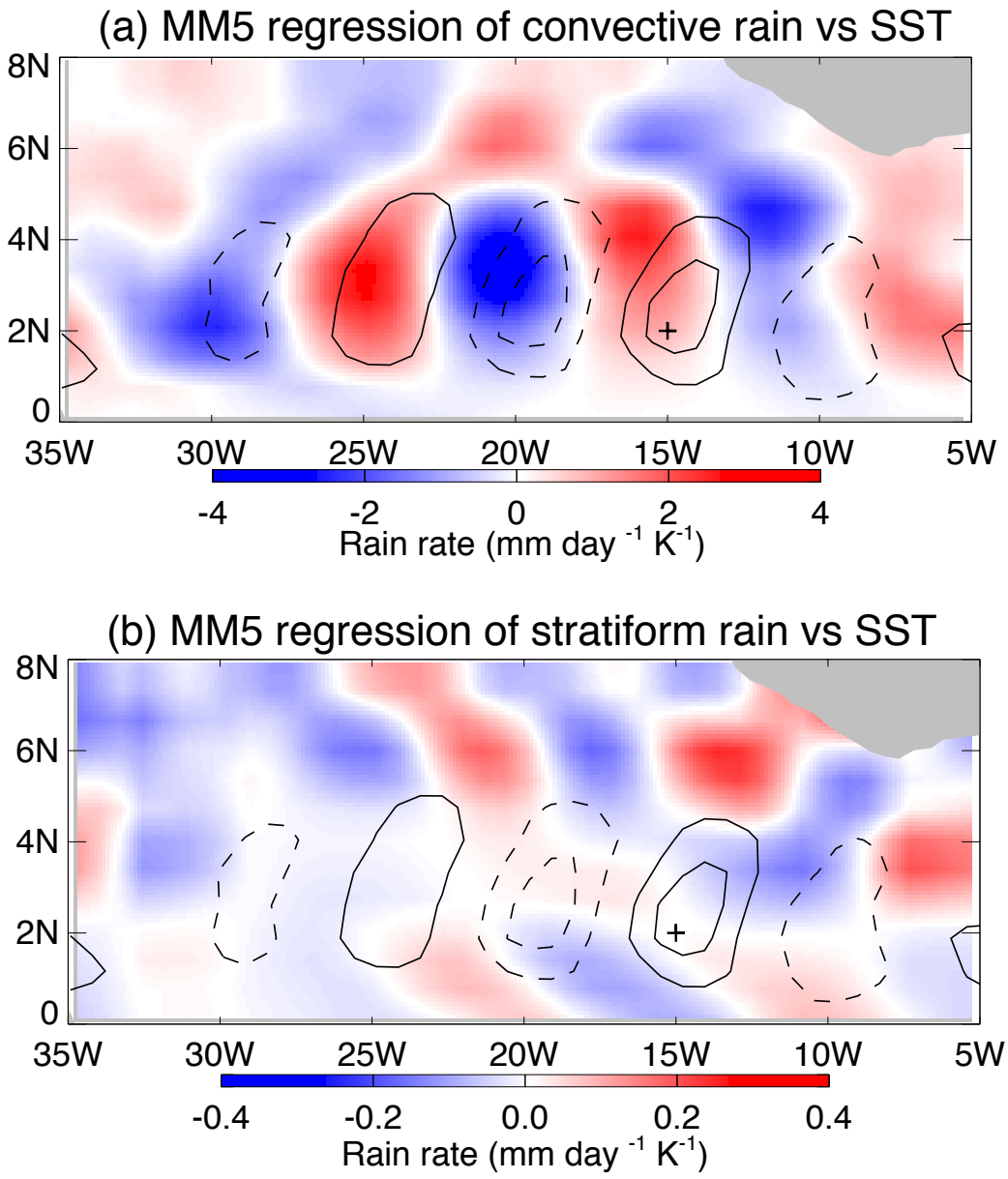

Fig. 31. Regression maps for rain from model. (a) Convective rain; (b) Resolved rain. The plus represents the reference point (15°W, 2°N) for regression. Red lines are contours of SST regression with intervals of 0.4K. Note difference in scales.

anomalies. The regression coefficient of U reverses sign above $\sigma = 0.825$. The reversal of sign shows small magnitude. The U regression profiles fail to capture the maximum contrast, since the U regression anomalies are phase-shifted relative to SST anomalies.

Regression coefficients for V are nearly out of phase with SST and air temperature anomalies in the lower layer (Figure 33a). The regression coefficient reverses sign above $\sigma = 0.9$. The V regression profile shows a decrease of southerly wind at the surface and an increase of southerly wind above $\sigma = 0.9$ over warm SST. The reverse is true over cold SST. The perturbations of V extend to higher altitudes than air temperature and U.

The regression coefficients for water vapor mixing ratio (Figure 33 b) are roughly in phase with SST and air temperature anomalies. Interestingly, the largest mixing ratio anomalies lie between $\sigma = 0.9 - 0.825$, not at the surface. The convergence and pressure fields shown in Figure 34 set up a thermal circulation cell. The circulation cells have ascent over convergence coinciding with high mixing ratios anomalies and descent over divergence coinciding with low mixing ratios.

The vertical structures of TIW in our model are slightly different from the study of Small et al. (2003) in the Pacific Ocean. In the model study of Small et al. (2003), V velocity regressions are up to 90° out of SST anomalies and U velocity regressions are over and east of SST anomalies. In our model, V velocity regressions are out of phase with SST anomalies and U velocity regressions are 90° phase shift of SST anomalies. The different result may due to differenent surface wind response mechanism in the Pacific and Atlantic Ocean or different model simulations.

E. Conclusions to Chapter VII

In this chapter, we investigated the atmospheric PBL response to TIW-induced SST variations using a regional climate model, and compared the model simulation with available

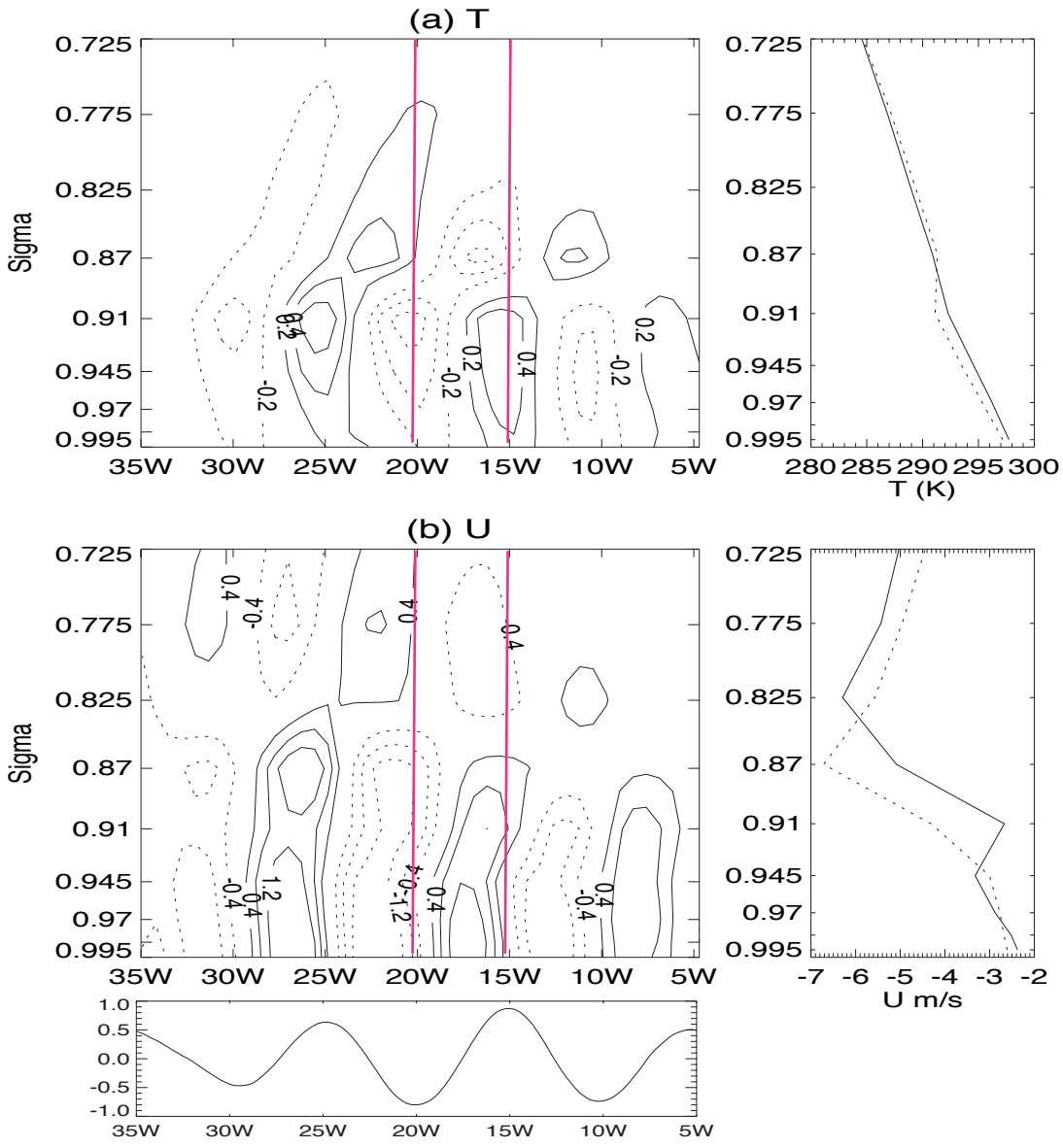

Fig. 32. Regression maps in longitude-vertical plane at 2°N. The vertical coordinate is σ. Accompanying total profiles over warm SST with solid line and over cold SST with dot line. (a) Air temperature (K), (b) U velocity (m/s). The red lines represent the warm and cold anomalies at 15°W and 20°W. The bottom panel shows the SST anomalies at 2°N.

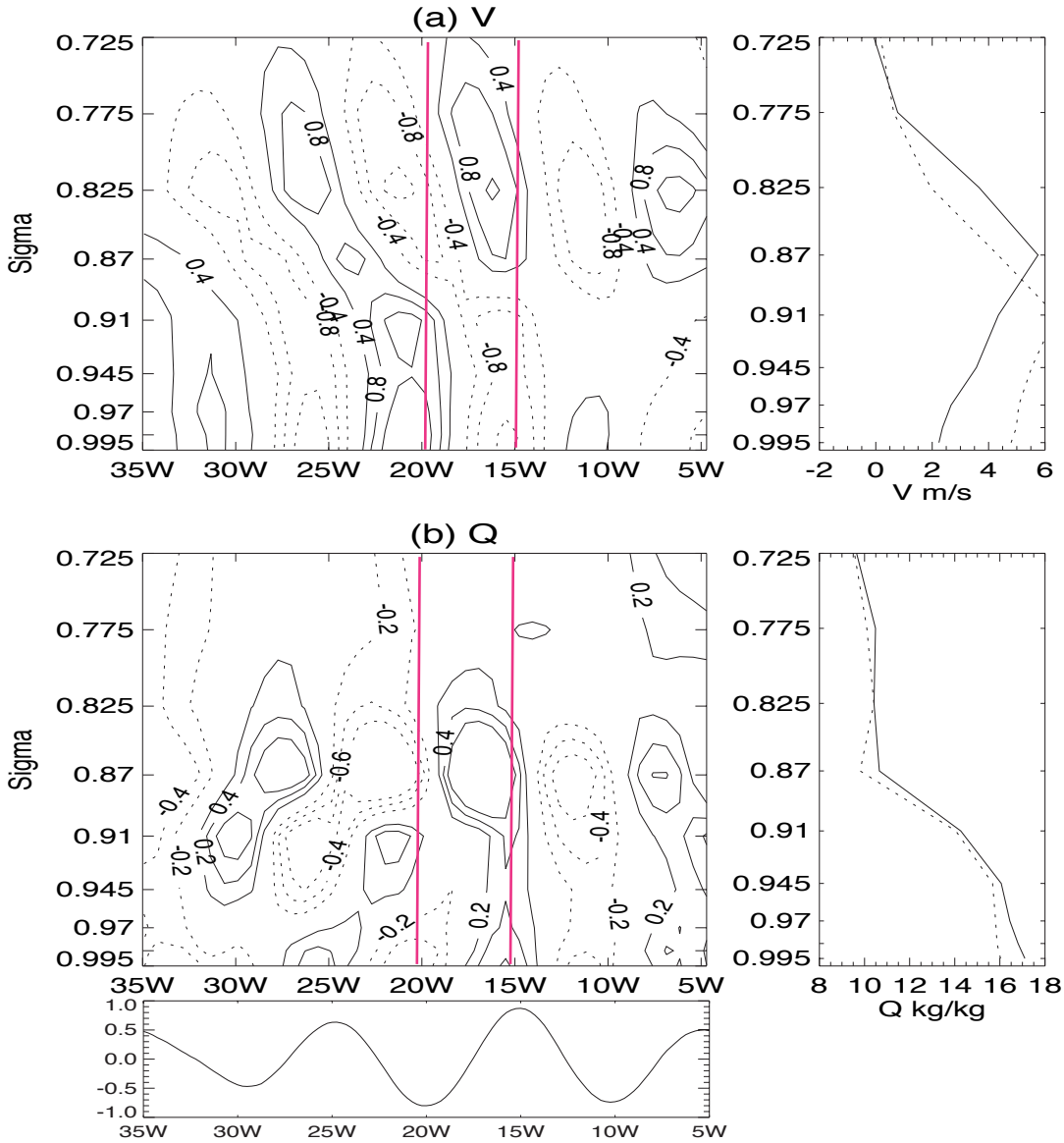

Fig. 33. The same as Figure 32 but for (a) V velocity (m/s) and (b) relative humanity (g/kg).

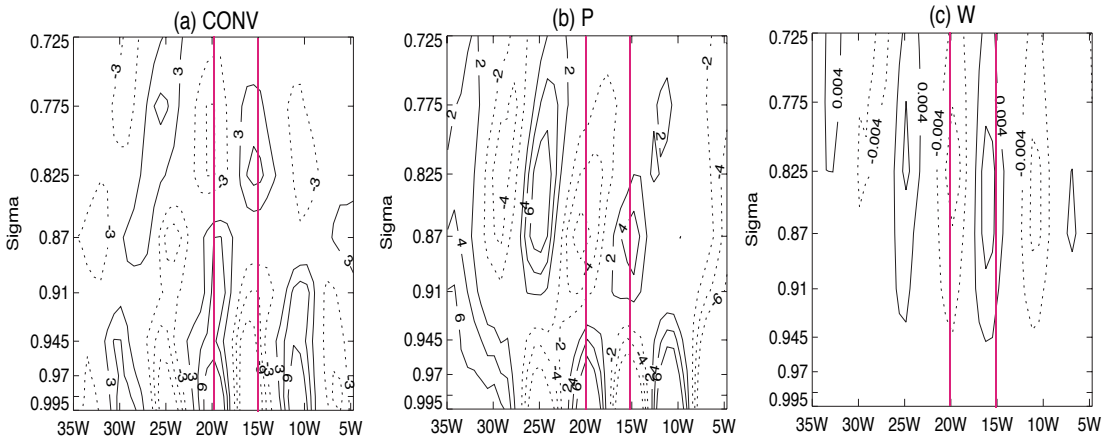

Fig. 34. Regression maps in longitude-vertical plane at 2°N for (a) Convergence ($10^{-6}s^{-1}$); (b) Pressure (mb); (c) Vertical velocity (m/s). The vertical coordinate is σ. The red lines represent the warm and cold anomalies at 15°W and 20°W.

satellite measurements.

The model tested the hypothesis that atmospheric responses are coupled to the TIW SSTs. The model successfully simulated similar wind velocity, wind convergence, column-integrated water vapor and precipitation perturbations similar to satellite observations of TIW-related variability.

Observational studies have used the phase relation between SSTs and surface winds to infer the mechanism responsible for the wind anomalies. This method may be unreliable due to the thermal and moisture advection by the mean wind (Small et al. 2003). The model shows that vertical mixing and pressure gradient are important for the atmospheric PBL response to SST variations associated with TIWs in the tropical Atlantic.

CHAPTER IX

NUMERICAL SIMULATION WITH CAM3

In the previous chapter we showed that the MM5 regional model simulated the atmospheric response to the Atlantic TIWs. In this chapter, we use a global climate model CAM to simulate the atmospheric response to the oceanic Atlantic TIWs. Both T42 and T85 resolutions are used to investigate whether the simulations are sensitive to model resolution.

A. T42 Model Ensemble

We use four numerical simulations to study the coupling of SST and atmospheric fields in the CAM T42 model. The westward propagation of TIWs in SST and air temperature, zonal and meridional wind at 992 mb, the lowest level of the model simulation at certain latitude is illustrated in longitude-time maps in a single simulation in Figure 35. The ensemble mean of the model simulations reduces the noise of the global circulation model simulation. SST and the atmospheric variables are filtered to isolated TIW signal from the background. The T42 mode of CAM simulates atmospheric response to the TIWs as T85 in late part. But the amplitude of atmospheric response it smaller in T42 than that in T85, which is most probably due to the lower resolution of the model.

B. Ensemble Effect of T85 Model

We made four numerical simulations with different initial conditions to study the coupling of SST and atmospheric fields in the CAM T85 model as well. SST and the atmospheric variables are filtered at 20-40 day over time domain and 5°-12° over space domain to isolate the TIW signals. The westward propagation of TIWs in SST, air temperature, zonal and meridional wind at 992 mb at certain latitude is illustrated in longitude-time maps in a

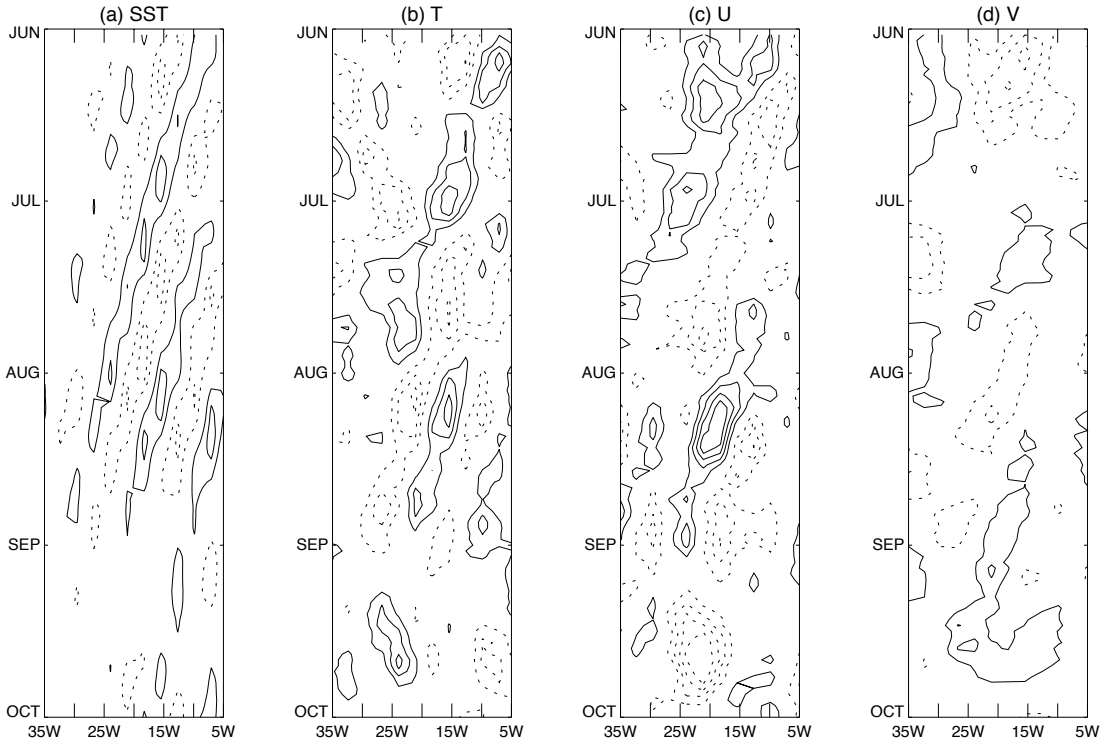

Fig. 35. Longitude-time distribution of SST, air temperature and surface wind components from a four-member T42 CAM ensemble. (a)daily SST with interval 0.1K; (b) air temperature at 995 mb with interval 0.025K; (c) U at 995 mb at with interval 0.025m/s; (d)V at 995 mb with interval 0.025 m/s.

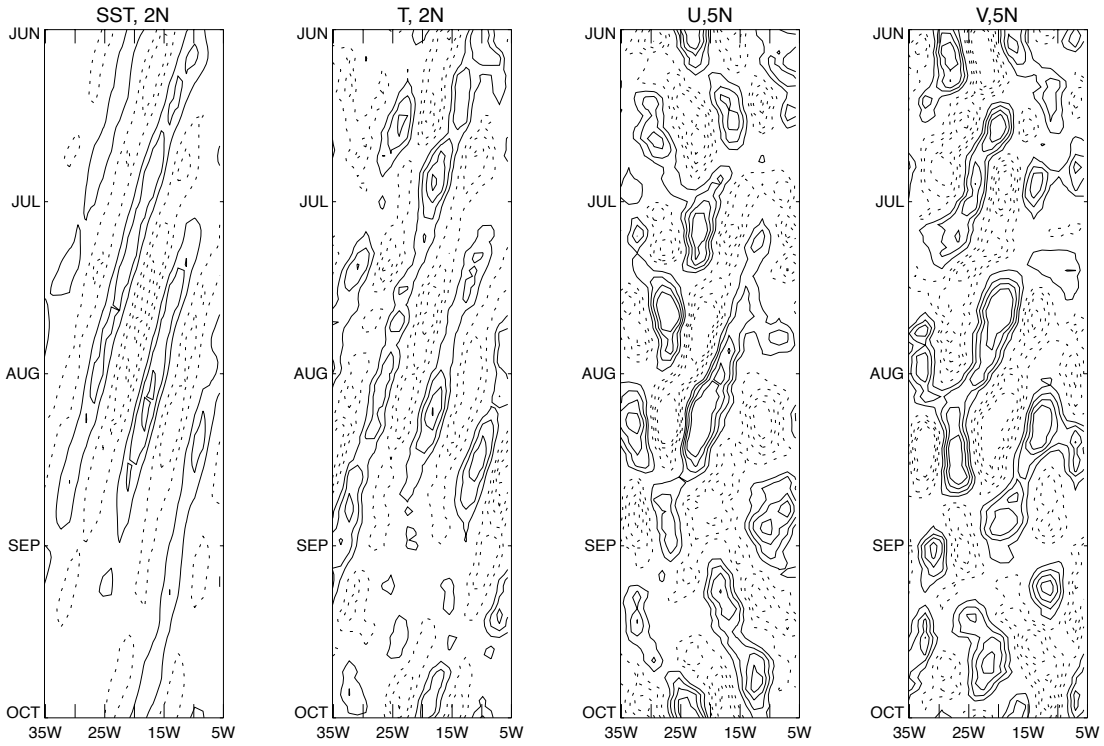

Fig. 36. Longitude-time distribution of daily SST and air temperature, surface wind in one CAM T85 simulation. (a)daily SST with interval 0.1K; (b) air temperature at 995 mb with interval 0.1K; (c) U at 995 mb at with interval 0.1m/s; (d)V at 995 mb with interval 0.1 m/s.

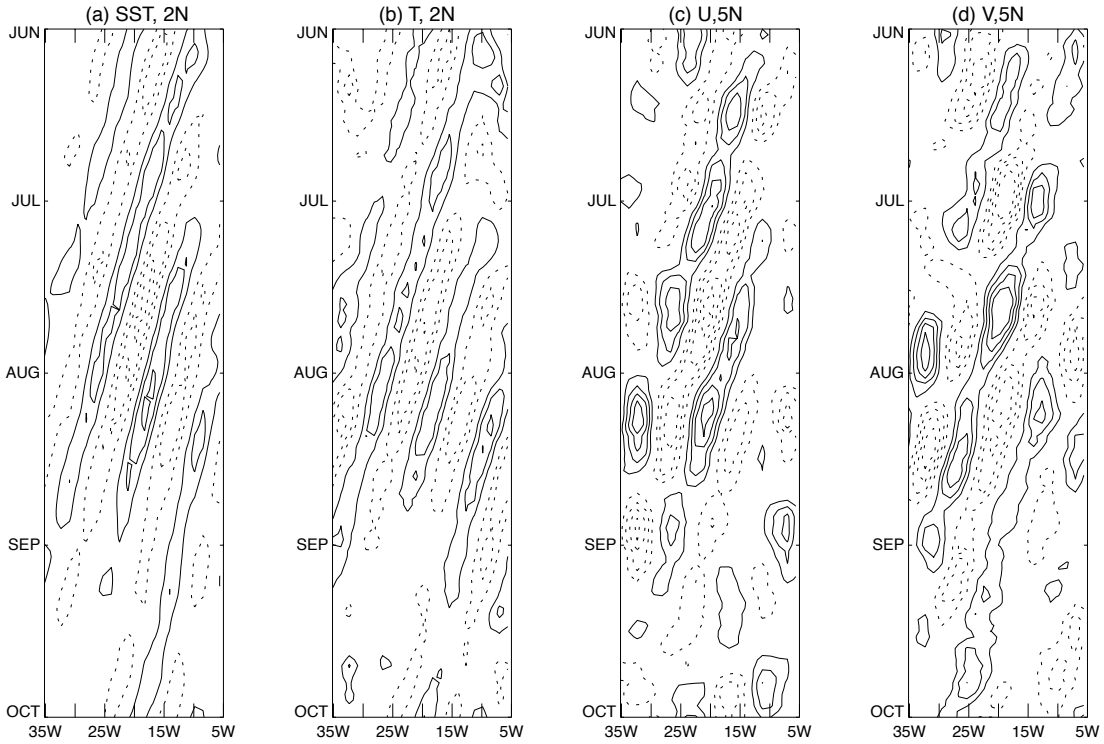

Fig. 37. Longitude-time distribution of SST, air temperature and surface wind components from a four-member T85 CAM ensemble. (a)monthly SST with interval 0.05K; (b) air temperature at 995 mb with interval 0.05K; (c) U at 995 mb at with interval 0.05m/s; (d)V at 995 mb with interval 0.05 m/s.

single simulation in Figure 36. A westward propagating signal is clear seen in air temperature and also can be identified in the zonal and meridional wind fields. The ensemble mean of the model simulations reduces the noise of the model simulation (Figure 37). The result shows that the failure to capture atmospheric response signal in the T42 mode is probably due to the low resolution. Since TIWs exist mainly in the latitude between the equator and 5°N and the model resolution the T42 mode is approximate 2.8°, it is hard capture the signal with such coarse resolution. All the analysis in the following parts are based on the ensemble mean of T85 resolution.

C. Background of CAM Simulation

The observed SST and the observed and simulated surface winds for 23 July 2000 are shown in Figure 38. A TIW wave train is seen in the SST field in the Atlantic. The southeast and northeast trade wind regimes are seen in both model and observations. Winds converge near 10°N over the warmest water. The major difference between the model and observations in the wind field is that the wind vectors are weaker in the model simulation over warm water in the ITCZ. The wind fields is similar to the simulation by MM5.

The mean rain rate in JJA 2000 from observations and the model is shown in Figure 39. Rain rates in both the Atlantic and Pacific ITCZ are weaker than the observations. In the interested region of our analysis, the model simulated the location of Atlantic ITCZ. The precipitation climatology is better than that from MM5.

D. Horizontal Structure

A similar analysis is applied to the CAM T85 simulations as to the MM5 model simulations. The reference point chosen for the regression is 15°W, 2°N as before, where SST shows maximum variance and a clear signal in the time series. Figure 40(a) shows the

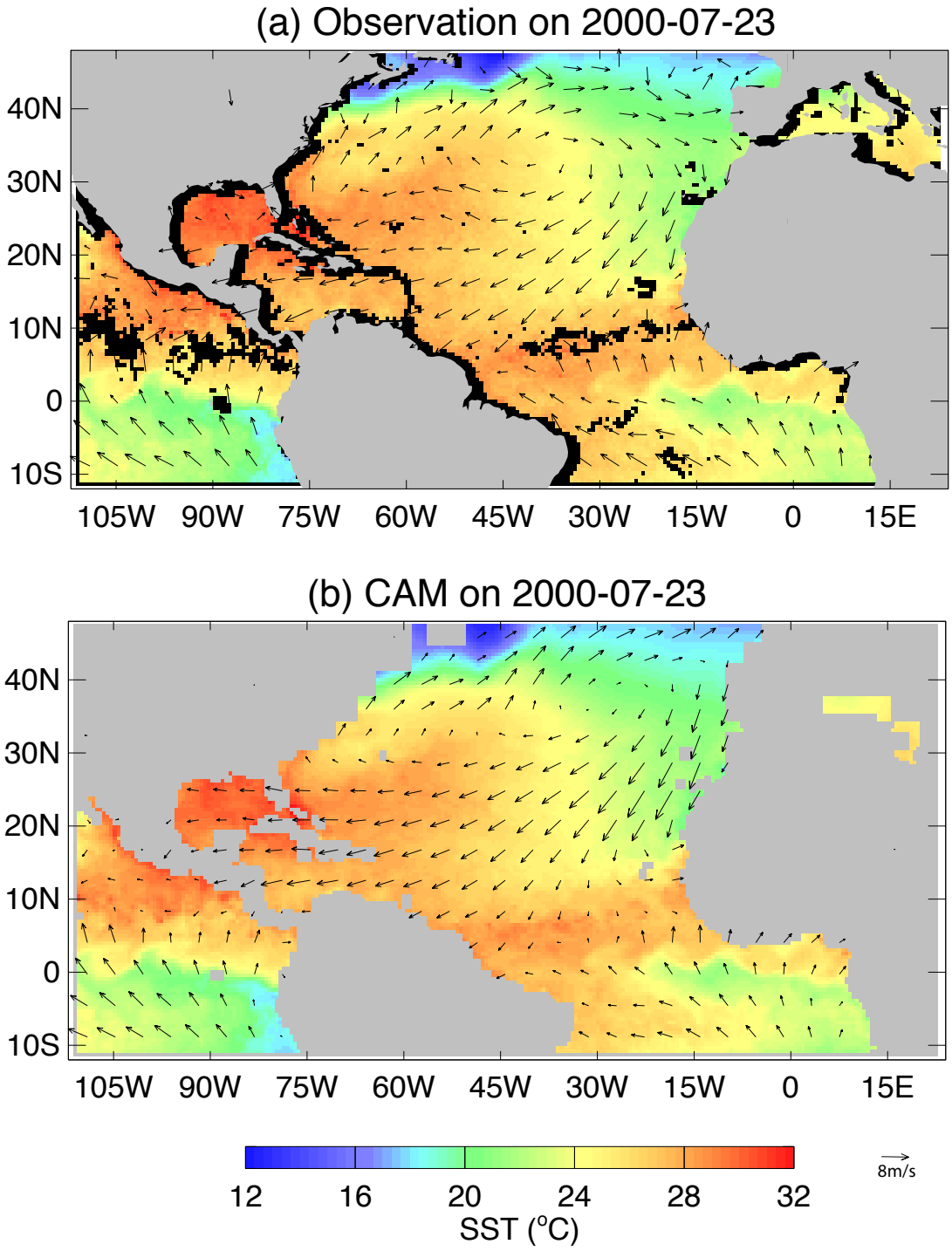

Fig. 38. SST and surface wind vector over the CAM model domain ended on 2000-07-23. (a) SST from TMI and surface winds from QuikSCAT; (b) interpolated SST data for model simulation and modeled surface winds. Missing SST data are shown in black.

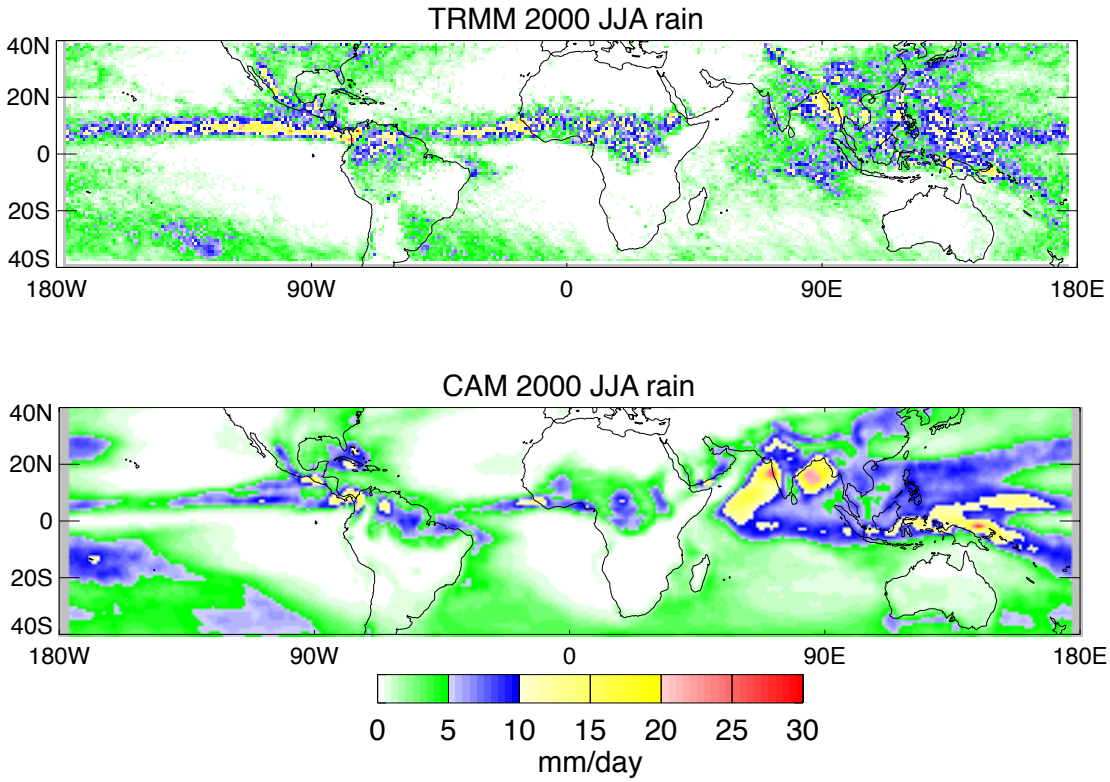

Fig. 39. Rain rate over the model domain in the period of JJA, 2000. (a) Observed rain rate from 3B42 rain rate data; (b) rain rate from four ensemble models.

patterns of regressed SST and wind vectors at 10 m from QuikSCAT. Winds converge to the west of warm SST anomalies and diverge to the west of cold SST anomalies. Wind anomalies can be large in the southern Atlantic even when SST anomalies are small. Wind anomalies can reach as far as 8°N, although the SST anomalies disappear north of 5°N.

Figure 40(b) shows the CAM wind regression vectors on top of the SST. The model wind vector patterns are similar to the observations in many aspects and are also similar to the MM5 simulation in many aspects. The wind convergence and divergence are located to the west of warm SST anomaly and cold SST anomaly. There are wind perturbations north of 5°N, where SST anomalies disappear. The wind response appears to be weaker in the Southern Hemisphere in the model than in the observations. The magnitude of the wind regression coefficient in the CAM simulation is similar to that of MM5 simulation.

Figure 41 shows the convergence, mixing ratio and rain response to TIW SSTs from the model simulation. In the model simulation, the wind convergence and divergence are in phase with warm SST anomalies and cold SST anomalies. This result agrees with Figure 40(a) in the wind fields. The magnitude of the convergence anomalies is of the same order as the observations, which is smaller than the convergence anomalies from MM5. The mixing ratio anomalies are downstream of the SST anomalies. Water vapor anomalies are positive above warm SST anomalies and negative above cold SST anomalies. The water vapor anomalies often extend to 8°N, well beyond the extent of the SST anomalies. Even though the TIWs are active in latitudes between the equator and 5°N, the rain anomalies show a remote response to the latitude between 2°N and 8°N. The CAM T85 model simulated the remote response feature in the Atlantic Ocean. The amplitude of the rainfall response is about the same order as in the observations.

The near-surface air temperature regressions in Figure 42 reach a magnitude of 0.4 K/K and -0.2K/K. These extremes are located generally in phase with the SST extremes. The wind anomalies converge into surface pressure minima and diverge into surface pres-

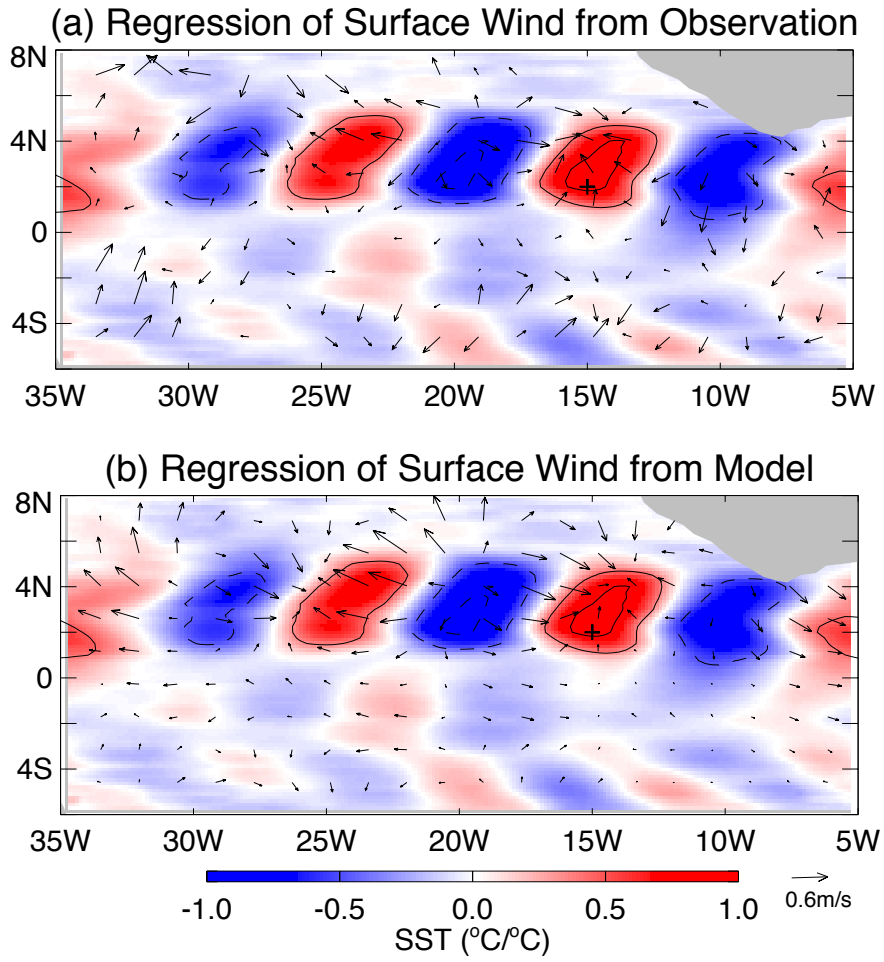

Fig. 40. Regression maps for SST and wind velocity in the period of JJA. (a) Observations from TMI and QuikScat; (b) Ensemble CAM simulation at the lowest level. The plus represents the reference point (15°W, 2°N) for regression. The contours are SST regression with intervals of 0.4K.

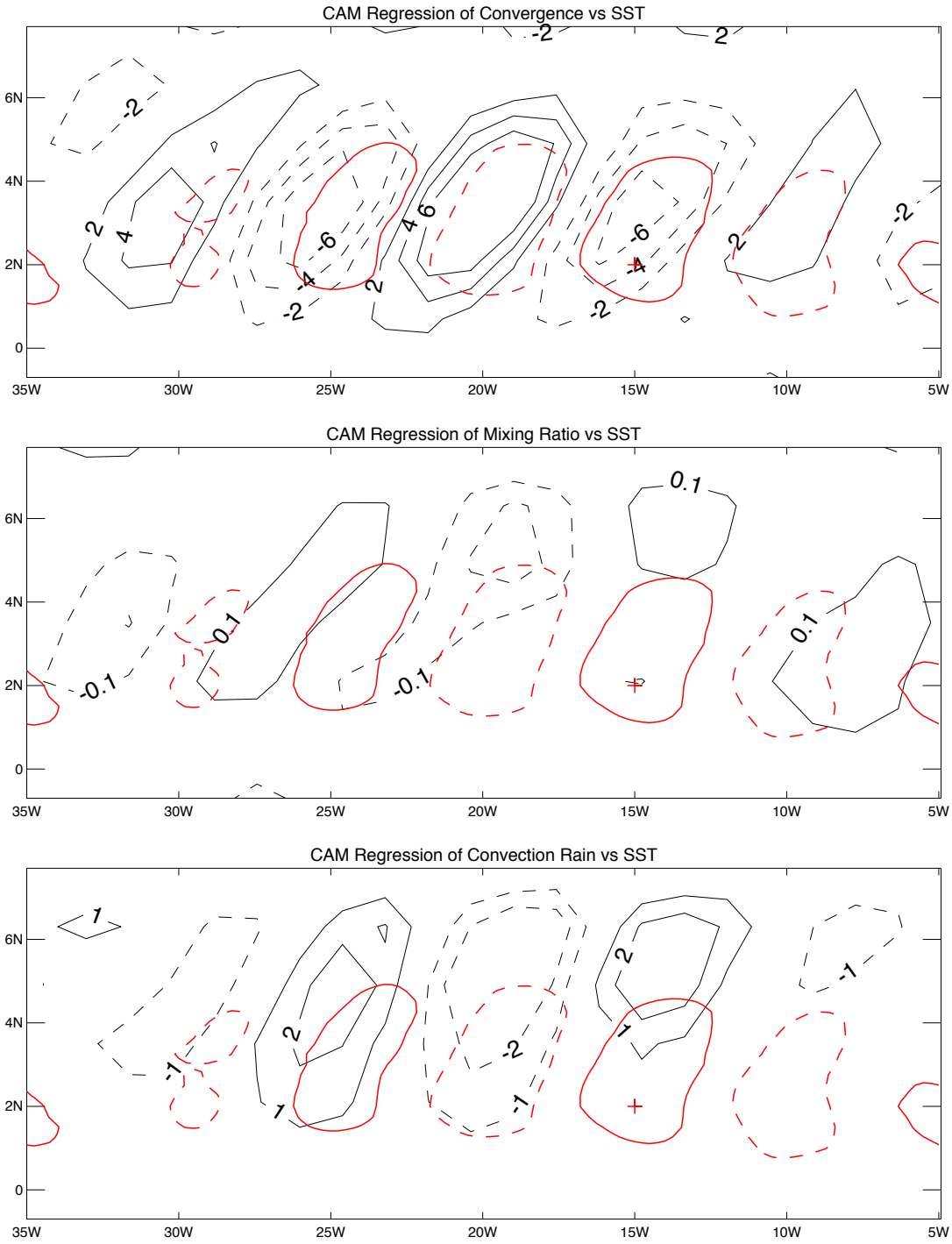

Fig. 41. Regression maps for surface wind convergence, mixing ratio and rain from CAM. (a) Surface wind convergence; (b) Mixing ratio; (c)Rain. The plus represents the reference point (15°W, 2°N) for regression. Red lines are contours of SST regression with intervals of 0.4K.

sure maxima. This result suggests that the pressure gradient is an important factor to the wind flow beside the vertical mixing factor. The magnitude of surface pressure anomaly reaches 10 Pa/K. The high and low pressure anomalies occur over low and high SST anomalies. These results agree with the results of Small et al. (2003) in the Pacific. This result further supports the Lindzen and Nigam (1987) mechanism in the Atlantic Ocean.

The TIW SSTs force a response of the sensible and latent heat fluxes (Figure 43). The latent heat flux anomalies are larger than sensible heat flux anomalies. Maximum heat anomalies are located at the maximum SST anomalies. That is, in the warm SST anomalies, TIWs take heat from the atmosphere and over cold SST anomalies, TIWs transfer the heat to the atmosphere. The response structure is like what we found from the MM5 regional model, but the magnitude of regression from the MM5 model is 2 to 3 times greater than that from CAM model simulation.

The SST waves also force a response of convective and resolved rain (Figure 44) as found in MM5 model. The magnitude of regression is approximately the same order as convective and stratiform rain by MM5. Both convective and stratiform rain show a remote response to the SST anomalies. The remote response does not show up in the convective rain response in MM5 model

Zonal and meridional wind stress (Figure 45) also show a response to the TIW-induced SST anomalies. Positive wind stress over warm SST anomalies and negative wind stress over cold SST anomalies. The magnitude of regression is approximately in the same order as in the zonal and meridional wind stress. The regression of wind stress extends further north than the SST anomalies. The farther north responses in the wind stress are consistent with the surface wind response. Response signals are also found in precipitable water and total cloud (Figure 46) . Both total precipitable water and total cloud show a downstream response to the SST anomalies. The PBL height (Figure 47) shows a response to the TIW related SST anomalies. PBL height is higher over warm SST anomalies and lower over

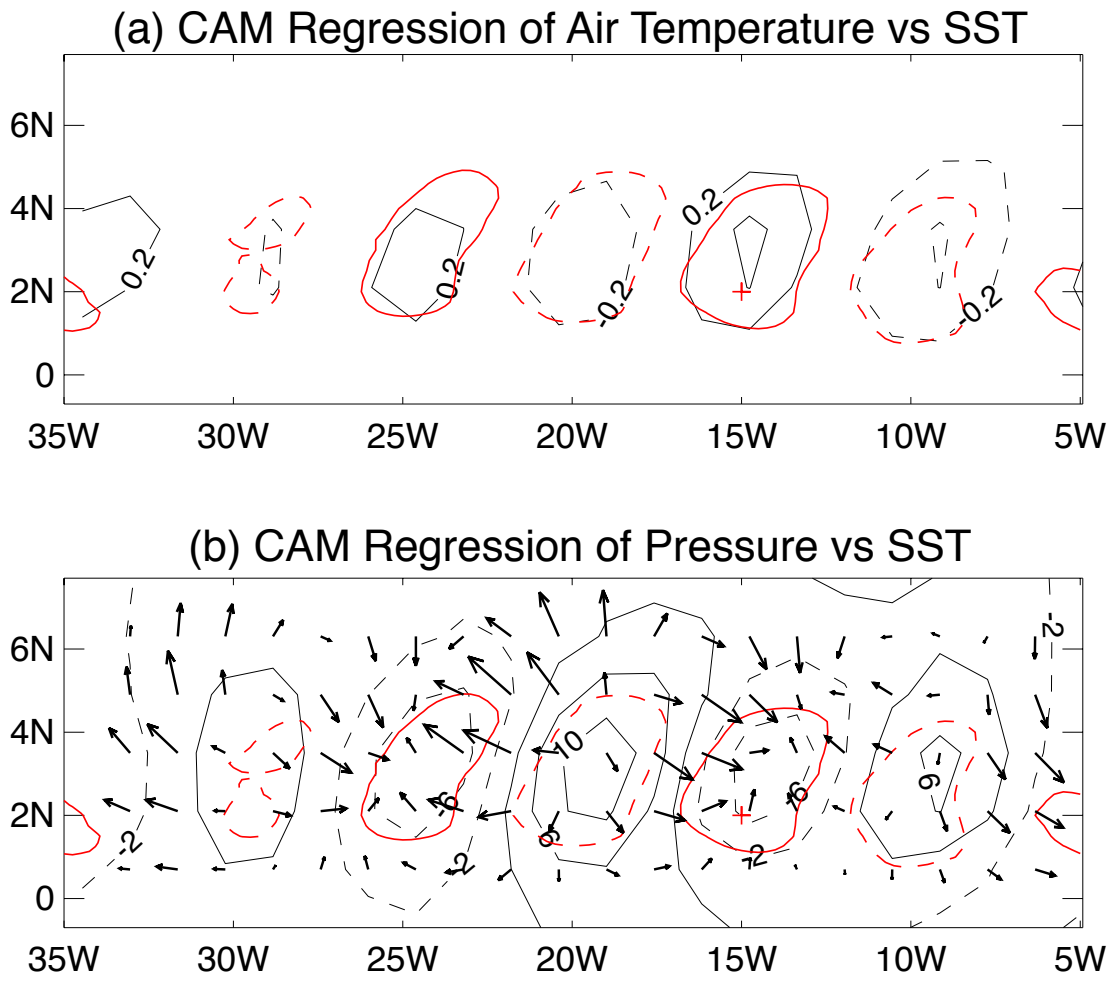

Fig. 42. Regression maps for air temperature, surface pressure and wind velocity from CAM. (a) Air temperature at lowest model level; (b) Surface pressure and surface wind. The plus represents the reference point (15°W, 2°N) for regression. Red lines are contours of SST regression with intervals of 0.4K.

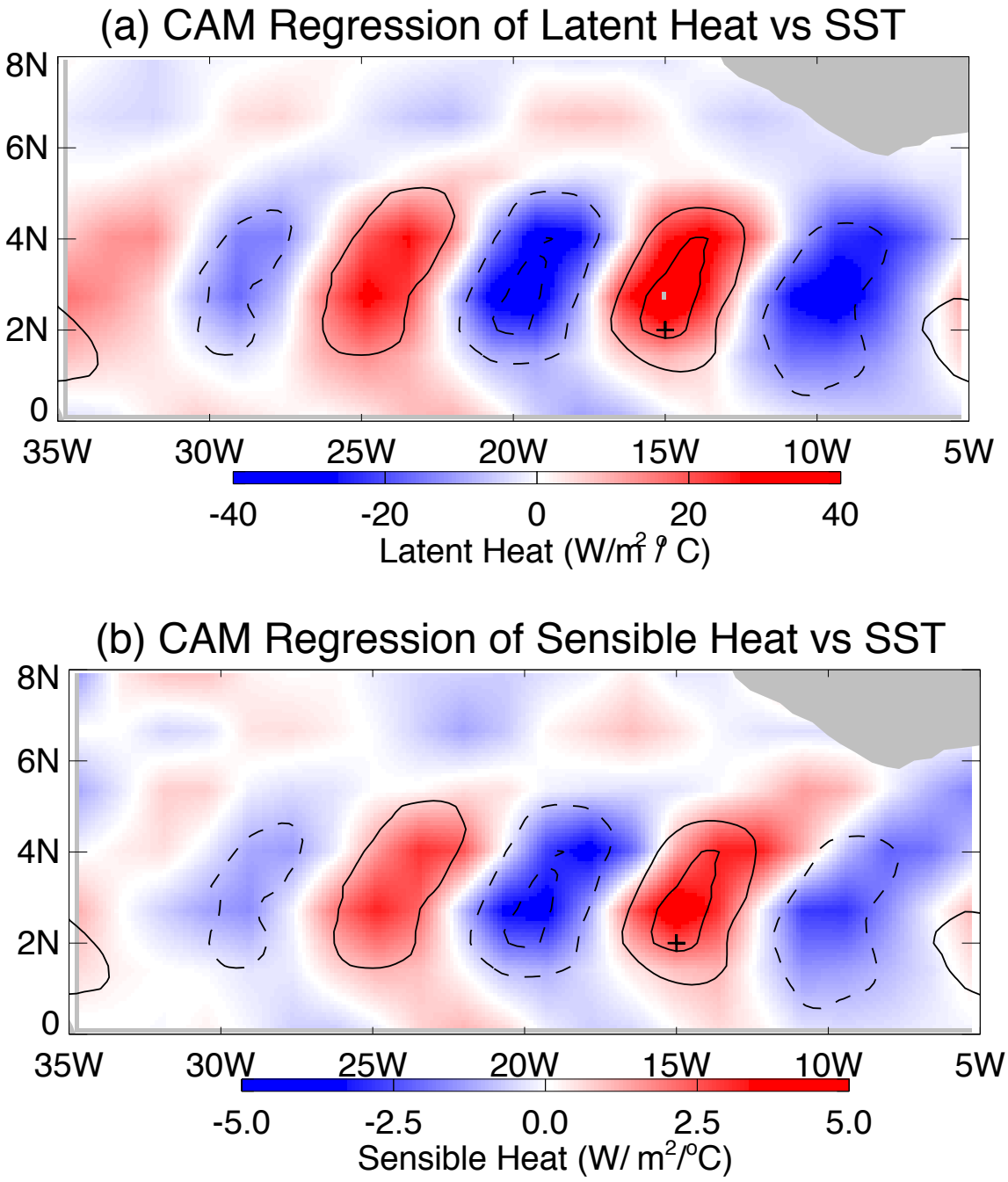

Fig. 43. Regression maps for heat from CAM ensemble models. (a) Sensitive heat; (b) Latent heat. The plus represents the reference point (15°W, 2°N) for regression. Contour lines are SST regression with intervals of 0.4K.

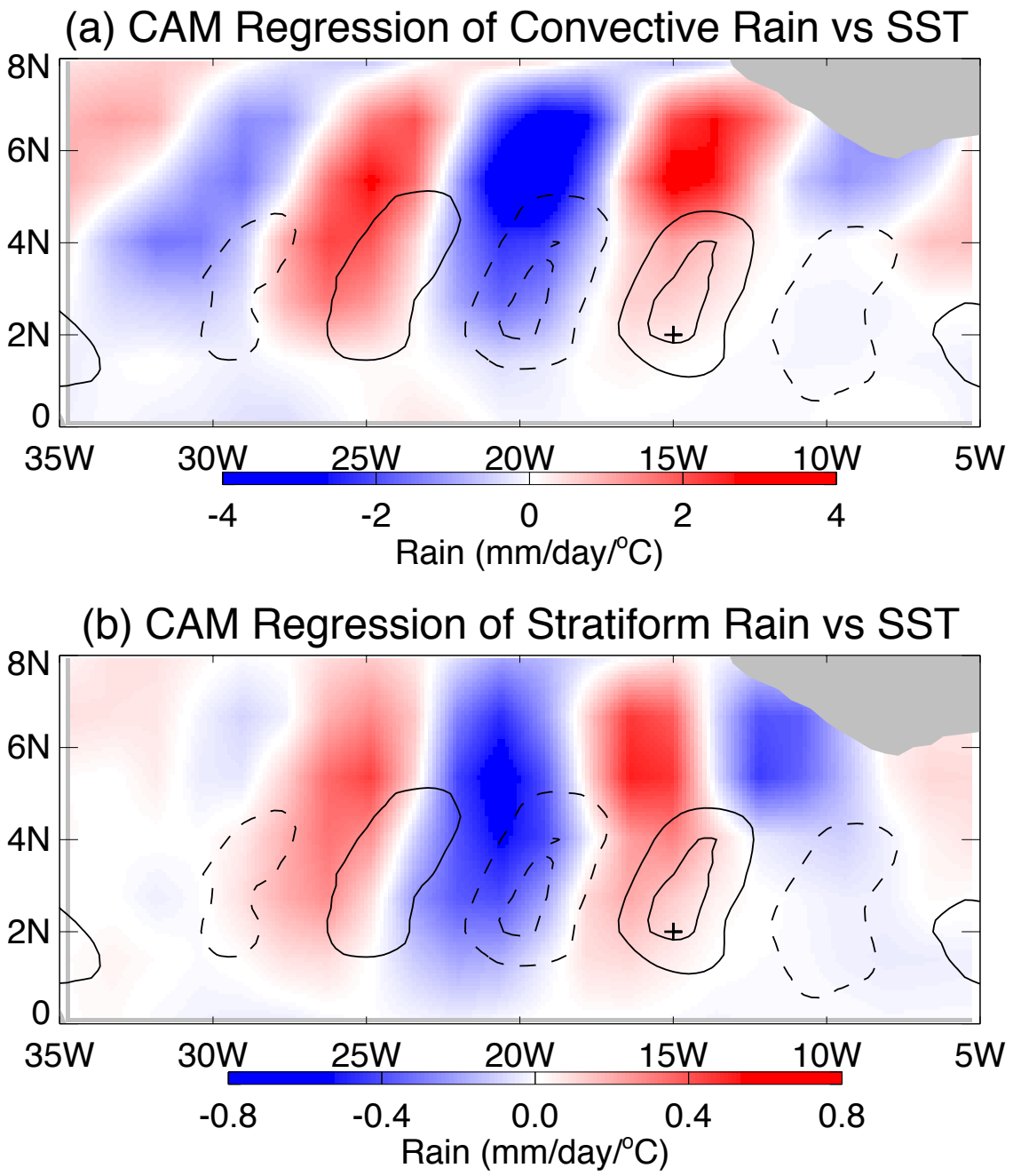

Fig. 44. Regression maps for rain from CAM ensemble models. (a) Convective rain (b) Resolved rain. The plus represents the reference point (15°W, 2°N) for regression. Contour lines are SST regression with intervals of 0.4K.

cold SST anomalies.

E. Vertical Structure

The vertical structures of the atmospheric response to the TIW SST variations at 2°N and variable profiles over warm and cold SST are shown in Figure 48 and Figure 49 in the same manner as for MM5. The warm profile defined as adding the regression profile at a positive SST regression at 2°N (16°W here) to the time-mean profile at 15°W,2°N. The cold profile is defined as adding the regression profile at negative SST regression at 5°N (21°W here) to the time-mean profile at 15°W,2°N.

The vertical structure of regression coefficient of air temperature can be seen in Figure 48 a. The air temperature perturbations correspond to heat transfered from SST underneath. The regression coefficient reverses sign above 850 mb. The air temperature perturbations are limited to below 700 mb.

Figure 48b shows the vertical structure of the regression coefficient of U. Negative surface anomalies of U lies to the east of warm SST and positive anomalies of U lies to the east of cold SST. There is about 90° phase shift between surface anomalies of U and SST anomalies. The regression coefficient of U reverses sign above 900 mb.

Regression coefficients of V are nearly out of phase with SST and air temperature anomalies in the lower layer (Figure 49b). The regression coefficient reverses sign above 900 mb. The V regression profile shows an decrease of southerly wind at the surface and an increase of southerly wind above 900 mb over warm SST.

The regression coefficients of water vapor mixing ratio (Figure 49 (a)) are roughly in phase with SST and air temperature anomalies. The largest mixing ratio anomalies lie between 950 mb and 860 mb.

The convergence and pressure fields shown in Figure 50 set up a thermal circulation

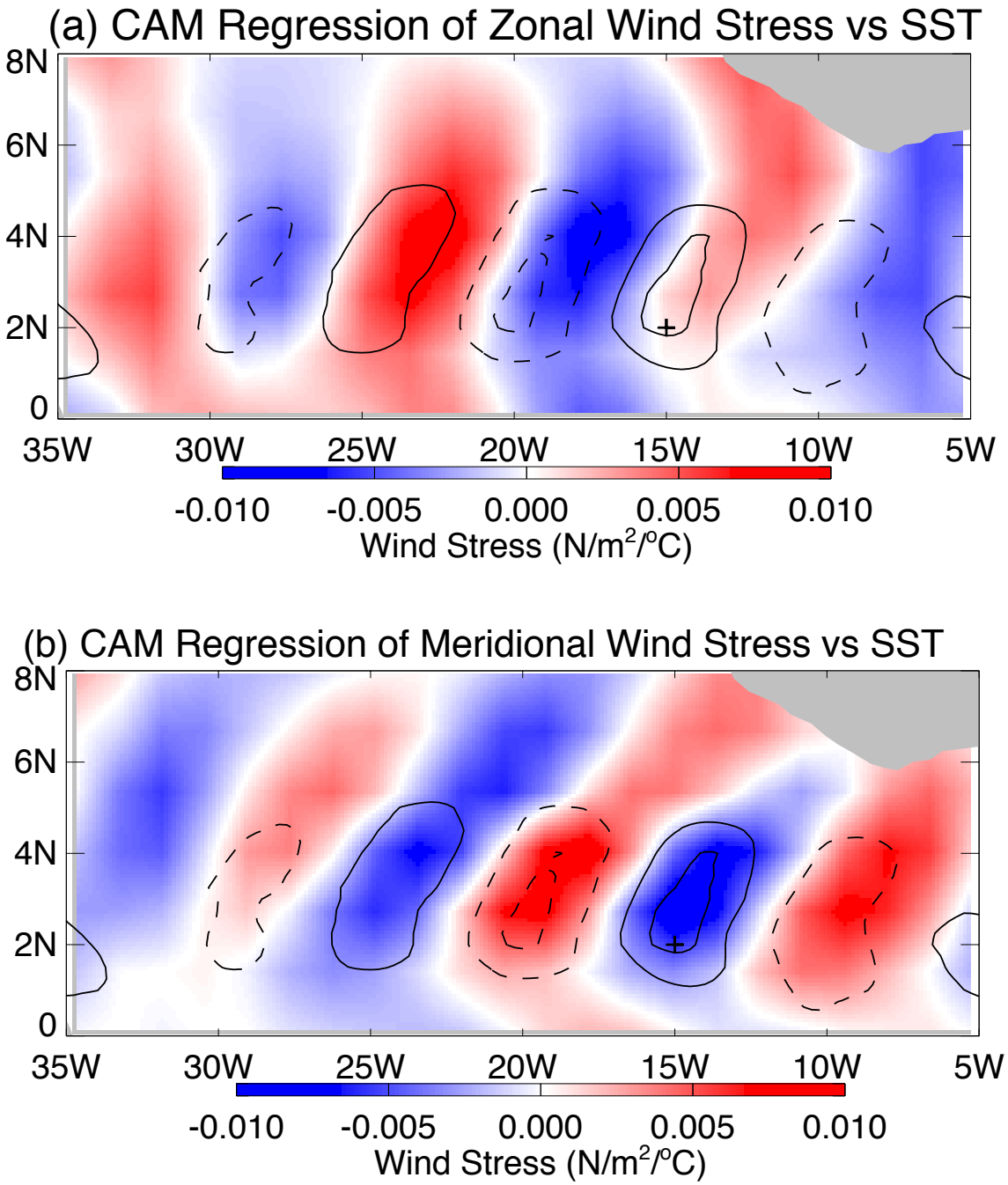

Fig. 45. Regression maps for stress from CAM ensemble models. (a) Zonal wind stress; (b) Meridional wind stress. The plus represents the reference point (15°W, 2°N) for regression. Contour lines are SST regression with intervals of 0.4K.

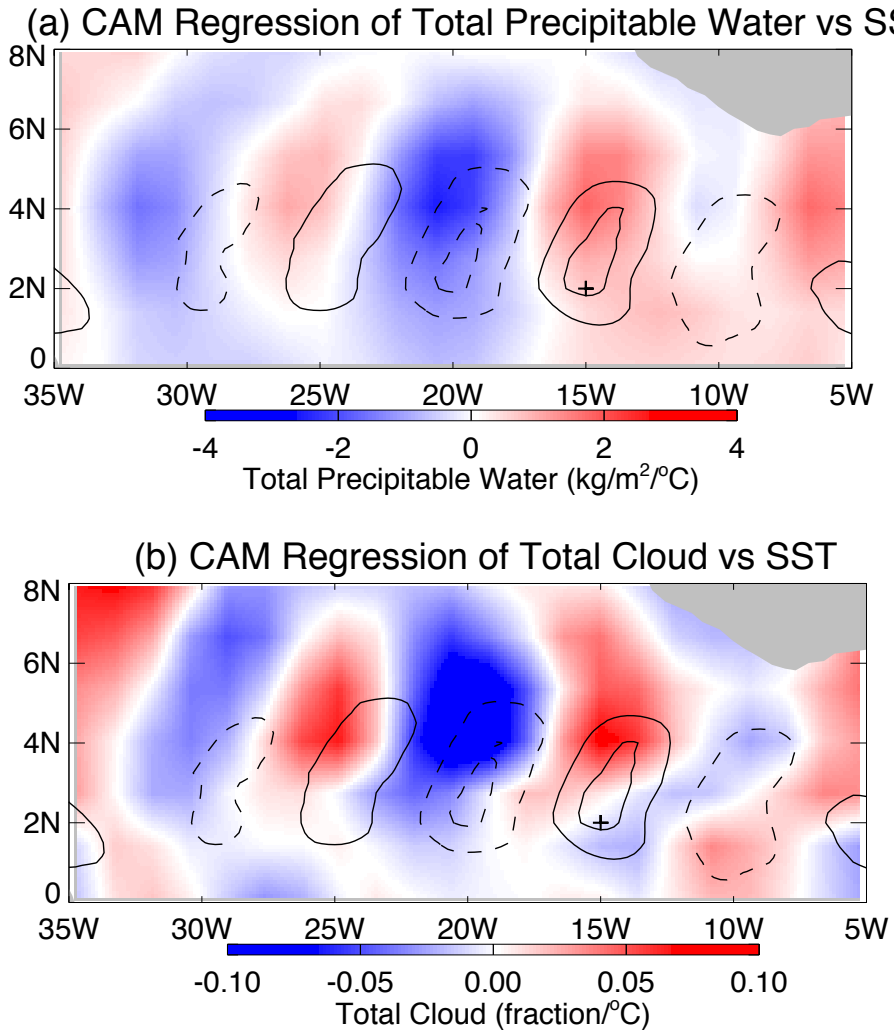

Fig. 46. Regression maps for stress from CAM ensemble models. (a) Total precipitable water; (b) Total cloud. The plus represents the reference point (15°W, 2°N) for regression. Contour lines are SST regression with intervals of 0.4K.

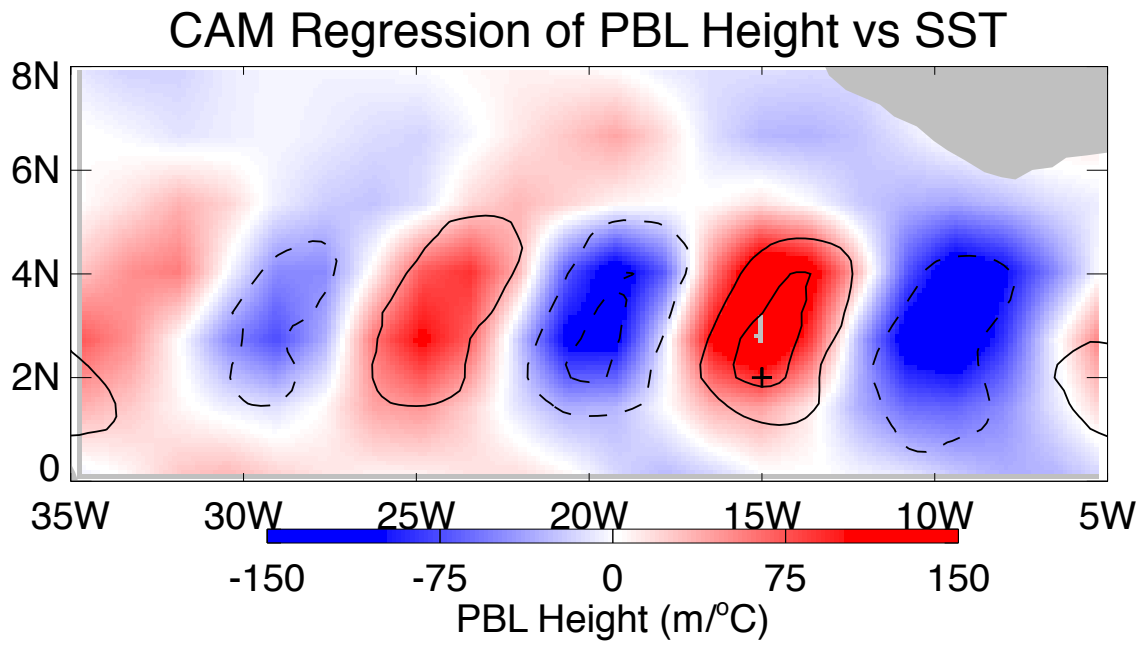

Fig. 47. Regression maps for PBL height from CAM ensemble models. The plus represents the reference point (15°W, 2°N) for regression. Contour lines are SST regression with intervals of 0.4K.

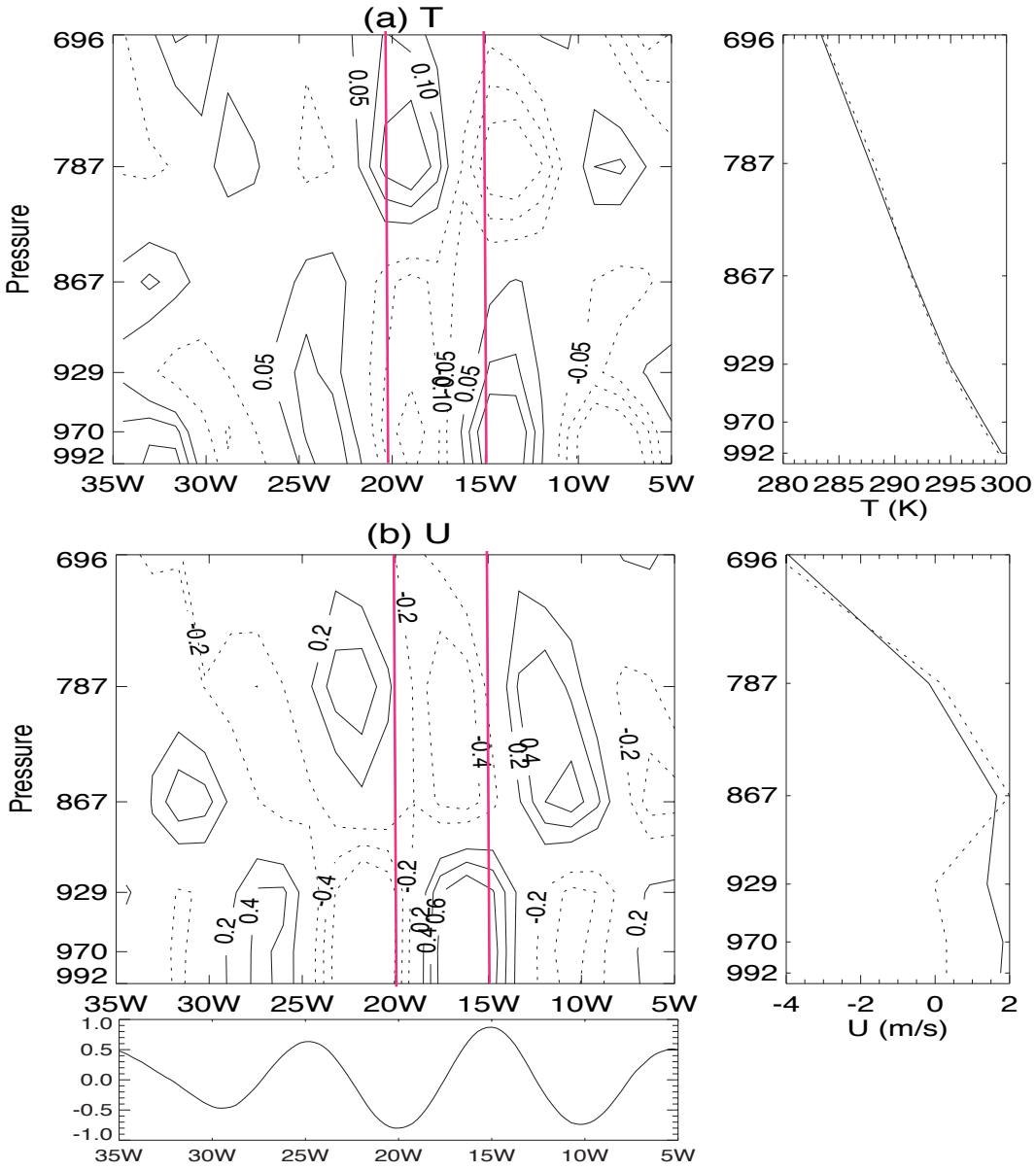

Fig. 48. Regression maps in longitude-vertical plane at 2°N. The vertical coordinate is σ. Accompanying total profiles over warm SST with solid line and over cold SST with dot line. (a) Air temperature (K), (b) U velocity (m/s). The red lines represent the warm and cold anomalies at 15°W and 20°W. The bottom panel shows the SST anomalies at 2°N.

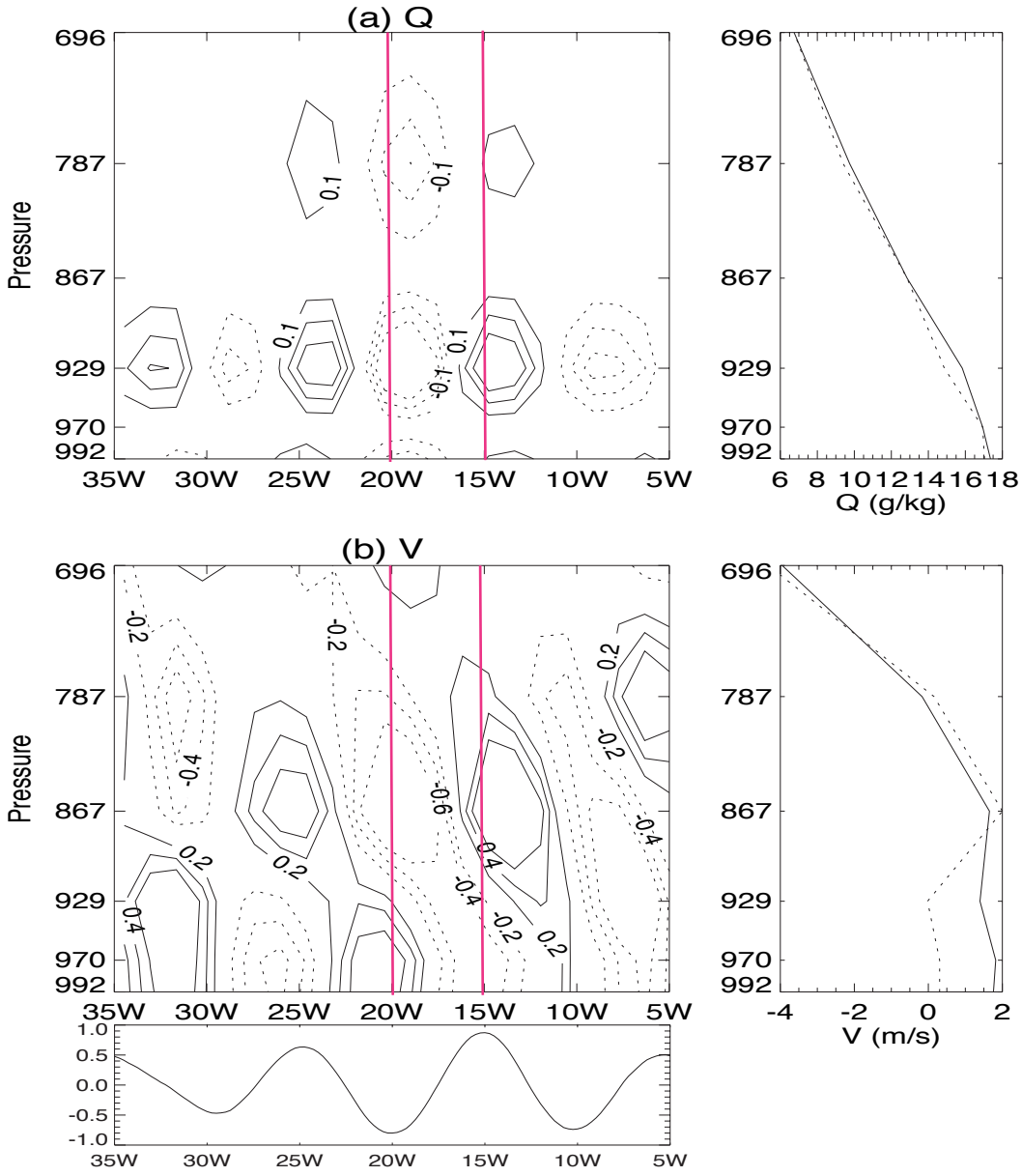

Fig. 49. The same as Figure 48 but for (a) relative humanity (g/kg) and (b) V velocity (m/s).

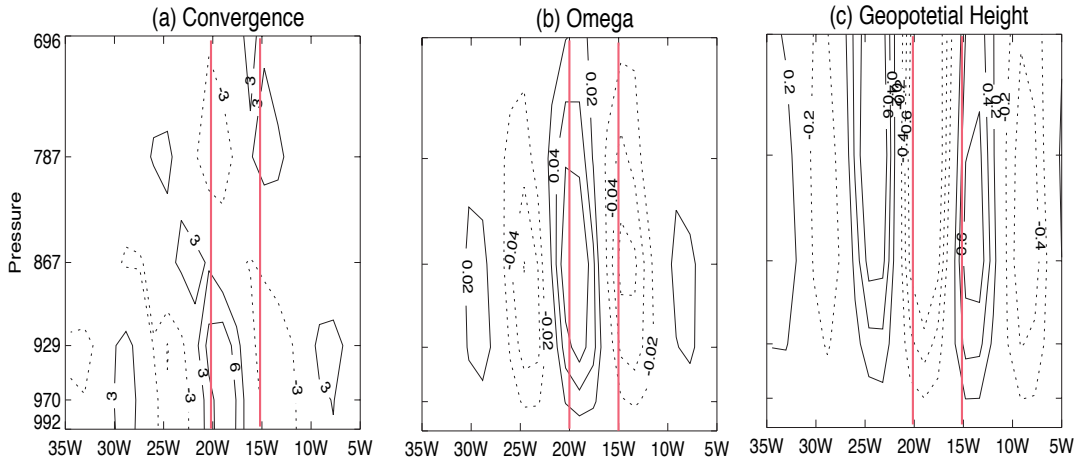

Fig. 50. Regression maps in longitude-vertical plane at 2°N for (a) Convergence ($10^{-6}s^{-1}$); (b) Pressure (mb); (c) Vertical velocity (m/s). The vertical coordinate is σ. The red lines represent the warm and cold anomalies at 15°W and 20°W.

cell. The circulation cells are ascent over convergence coinciding with high mixing ratio anomalies, and descent over divergence coinciding with low mixing ratio.

F. Conclusions to Chapter IX

In this chapter, we investigated the atmospheric PBL response to TIW-induced SST variations using a global climate model with two different horizontal resolution. both CAM T42 and CAM T85 model successfully simulated some atmospheric response features. Four simulations are made for both T42 and T85 resolution. In the T85 resolution, each simulation shows wave signals in the atmospheric fields. The ensemble mean of the four simulations reduces the noise in the atmospheric fields.

The model tested the hypothesis that atmospheric responses are coupled to the TIW SSTs. The model also successfully simulates similar wind velocity, wind convergence, mixing ratio and precipitation perturbations due to TIWs as satellite observation. The re-

mote response in the rainfall is also shown in the model simulation, which is similar to the observation.

The result from CAM model is generally consistent with the result from MM5 model. Comparing to the satellite observation, the model simulation, seems to support the pressure gradient mechanism of how TIW influence the PBL. The different between both CAM and MM5 and the result from Small et al. (2003) in vertical structure is most probably due to difference surface wind response mechanism in the Pacific and Atlantic Ocean.

CHAPTER X

SUMMARY AND CONCLUSIONS

Tropical instability waves are observed very often in the tropical Pacific and Atlantic Oceans. The phenomenon of TIWs is generally attributed to the instability of meridional shears associated with strong equatorial currents (Philander 1978; Cox 1980). TIWs are an important aspect of equatorial ocean dynamics and thermodynamics (Hansen and Paul 1984; Wang and McPhaden 1999). While TIWs have oceanic origin, the SST variations associated with TIWs can induce atmospheric variability (Hayes et al. 1989; Deser et al. 1993; Xie et al. 1998; Hashizume et al. 2001).

Eight-year TRMM SST data are used to study the interannual variations of TIWs in the Pacific and Atlantic Oceans. TIWs have a well-defined seasonal cycle in both the Pacific and Atlantic basins. In the Pacific. TIWs are observed on both sides of the Pacific cold tongue, but the most intense waves are on the northern side between the equator and 6°N. On internannual time scales the wave activity varies with the phase of ENSO. Wave activity is strongest and extends farthest west during ENSO cold phases. Waves are weak when the MEI index is positive, indicating warm ENSO conditions; and the waves appear to have vanished entirely during the strong 1997-1998 El Niño. In the Atlantic Ocean, TIWs develop rapidly due to geographic features of the basin, beginning in June and terminating in August. Unlike the Pacific, TIW activity in the Atlantic does not show a clear relationship with Pacific ENSO indices. TIW activity in the Atlantic is influenced by the Atlantic air-sea coupled mode as measured by the ATL3 index. As in the Pacific, wave activity is strongest during the cold phase of the Atlantic coupled mode, and weak when the ATL3 index is positive, the warm phase of the Atlantic coupled mode. Wave amplitude, wavelength, and phase speed vary from year to year in both basins. Generally, TIWs in the Pacific have a longer wavelength and higher wave speed than those in the Atlantic.

Interannual variations of TIW characteristics are associated with interannual variations of the background oceanographic state.

High-resolution satellite measurements from TRMM, QuikSCAT and SSM/I are used to further study coupled ocean-atmosphere variablity in the equatorial Atlantic. Coherent ocean-atmosphere patterns appear throughout the period from 1998 to 2005. Although TIWs are largely confined to a narrow latitudinal zone just north of the equator, their atmospheric response extends farther north and can influence the ITCZ. The observations show that the southeasterly trades strengthen over warm TIW SST anomalies and weaken over cold SST anomalies. Wind anomalies have an amplitude of $\sim$0.4 to 0.6 ms^{-1} K^{-1} at 2°N. The water vapor variability induced by TIW SST anomalies explains $\sim$5 to 15% of the total variation. Cloud liquid water and rainfall responses to the TIW SST follow similar patterns, appearing to downstream of the SST anomalies. The TIW-induced cloud liquid water anomalies account for $\sim$5 to 10% of the total variation and precipitation anomalies account for $\sim$10 to 20% of the total precipitation variation.

Atmospheric responses to TIW SSTs extend to 8°N, which is north of the principal TIW activity zone, suggesting a remote downstream response to the TIW SST anomalies. The atmospheric responses to these TIWs show interannual variability. In 1999, the rainfall response to TIWs in the latitude between 2°N and 4°N is much larger than in other years, which we attribute to the anomalously warm SSTs at 2°N and the southward movement of Atlantic ITCZ in that year. The atmospheric response in 1999 does not appear to be typical of other years. The comparatively warm temperatures in the TIW region in 1999 apparently increased the precipitation and made the atmosphere more sensitive to TIW variations. When the ITCZ takes a more southerly position, the synoptic variability in precipitation can be larger than its monthly mean. As the Atlantic ITCZ moves south, it is more susceptible to TIW influences.

This dissertation suggests that vertical mixing dominates the relationship between SST

and surface wind, as proposed by Wallace et al. (1989), because the convergence and divergence are out of phase with the SST anomalies. We cannot conclude, that however, both mechanisms are not operating. Using a regional model in the Pacific, Small et al. (2003) found vertical mixing, horizontal advection, and the perturbation pressure gradient are all induced by the SST changes. Horizontal advection leads to the occurrence of the air temperature and moisture extrema downwind of the SST extrema. Previous studies (Hashizume et al. 2001; Liu et al. 2000; Caltabiano et al. 2005) have used the relative phase between atmosphere response and SST to test the relationship between surface wind and SST. But this method may be unreliable because of the thermal and moisture advection by the mean wind as suggested by (Small et al. 2003).

How the atmosphere responds to intraseasonal SST changes is an important aspect of climate variability in the Atlantic Ocean. Current research on large-scale ocean-atmosphere interaction has focused on ENSO phenomena in the tropical Pacific, a process limited to high-SST regions. Most of the ocean in the world is not warm enough to support deep convection. Thus, TIWs provide an opportunity for studying the atmospheric response in cooler SST regimes.

Regional climate model MM5 and global climate model CAM3 are applied to study the mechanism of atmospheric response to the Atlantic TIWs with daily TMI satellite SST forcing. Both models successfully simulated the wind velocity, wind convergence and precipitation as observed. While the satellite observations support the vertical mixing mechanism for the surface wind response to TIWs, both models show the pressure gradient mechanism is dominant in the Atlantic.

Two numerical simulations of the 2000 TIW season with MM5 are made to study the coupling of SST and atmospheric fields. The first run, referred to as the control run, uses monthly SSTs. In the second run, referred to as the TIW run, the model was forced with daily SSTs. We expected little or no TIW signal in the atmosphere fields with monthly

SST forcing. The 20-40 day TIW signals are largely absent in the monthly SST data. In the control run, there is little evidence of wave signals in the atmosphere field, while in the TIW run, air temperature, zonal and meridional winds all show strong westward-moving signals. This demonstrates that atmospheric variations are coupled to TIW variability in the model.

This dissertation also investigated the atmospheric PBL response to TIW-induced SST variations using a global climate model with two different horizontal resolution. Four simulations are made for both T42 and T85 resolution. In the T85 resolution, each simulation shows wave signals in the atmospheric fields. The ensemble mean of the four simulations reduces the noise in the atmospheric fields. Both CAM T42 and CAM T85 model successfully simulated some atmospheric response features. But the amplitude of atmospheric response is smaller in T42 than that in T85, which is most probably due to the lower resolution of the model.

REFERENCES

Baturin, N. G. and P. P. Niiler, 1997: Effects of instability waves in the mixed layer of the equatorial Pacific. *J. Geophys. Res.*, **102**, 27771–27793.

Blackadar, A. K., 1979: High resolution models of the planetary boundary layer. *Adv. Environ. Sci. Eng.*, **1**, 50–85.

Bryden, H. and E. Brady, 1989: Eddy momentum and heat flux and their effects on the circulation of the equatorial Pacific Ocean. *J. Mar. Res.*, **47**, 55–79.

Caltabiano, V., I. S. Robinson, and L. P. Pezzi, 2005: Multi-year satellite observations of instability waves in the Tropical Atlantic Ocean. *Ocean Discussion.*, **2**, 1–35.

Chelton, D. B., S. K. Esbensen, M. G. Schlax, N. Thum, M. H. Freilich, F. J. Wentz, C. L. Gentemann, M. J. McPhaden, and P. S. Schoph, 2000a: Observations of coupling between surface wind stress and sea surface temperature in the eastern tropical Pacific. *J. Climate*, **14**, 1479–1498.

Chelton, D. B., F. J. Wentz, C. L. Gentemann, R. A. de Szoeke, and M. G. Schlax, 2000b: Satellite microwave SST observations of transequatorial tropical instability waves. *Geophys. Res. Lett.*, **27**, 1239–1242.

Chiang, J., Y. Kushnir, and A. Giannini, 2002: Reconstructing Atlantic Intertropical Convergence Zone variability: Influence of the local cross-equatorial sea surface temperature gradient and remote forcing from the eastern equatorial Pacific. *J. Geophys. Res.*, **107**, doi:10.1029/2000JD000307.

Collins, W. D., P. J. Rasch, B. A. Boville, J. J. Hach, J. R. McCaa, D. L. Williamson, J. T. Kiehl, B. Briegleb, C. Bitz, S.-J. Lin, and M. Z. Y. Dai, 2004: Description of the

ncar community atmosphere model (CAM3). Technical Report NCAR/TN- 464+STR, National Center for Atmospheric Research, Boulder, Colorado 80307-3000, 226 pp.

Contreras, R., 2002: Long-term observations of tropical instability waves. *J. Phys. Oceanogr.*, **132**, 2715–2722.

Cox, M. D., 1980: Generation and propagation of 30-day waves in a numerical model of the Pacific. *J. Phys. Oceanogr*, **10**, 1168–1186.

Deser, C., J. J. Bates, and S. Wahl, 1993: The influence of sea-surface temperature-gradient on stratiform cloudiness along the equatorial front in the Pacific Ocean. *J. Climate*, **6**, 1172–1180.

Düing, W., P. Hisard, E. J. Katz, J. Knauss, J. Meincke, L. Miller, K. Moroshkin, S. G. H. Philander, A. Rybnikov, K. Voigt, and R. H. Weisberg, 1975: Meanders and long waves in the equatorial Atlantic. *Nature*, **257**, 280–284.

Gentemann, C. L., F. J. Wentz, C. A. Mears, and D. K. Smith, 2004: In situ validation of tropical rainfall measuring mission microwave sea surface temperatures. *J. Geophys. Res.*, **109**, art. no.CC04 021.

Giannini, A., J. C. H. Chiang, M. A. Cane, Y. Kushnir, and R. Seager, 2001: The ENSO teleconnection to the tropical Atlantic Ocean: Contributions of the remote and local SSTs to rainfall variability in the tropical Americas. *J. Climate*, **14**, 4530–4544.

Grell, G. A., 1993: Prognostic evaluation of assumptions used by cumulus parameterizations. *Mon. Wea. Rev.*, **121**, 764–787.

— 1994: A description of the fifth-generation Penn State/NCAR mesoscale model (MM5). NCAR Tech. Note TN-398+STR, 122pp.

Grodsky, S. A., J. A. Carton, C. Provost, J. Servain, J. A. Lorenzzetti, and M. J. McPhadent, 2005: Tropical instability waves at $0°n$, $23°w$ in the Atlantic: A case study using pilot research moored array in the tropical Atlantic (PIRATA) mooring data. *J. Geophys. Res.*, **110**, doi:10.1029/2004JC002817.

Gu, G. and R. F. Adler, 2006: Interannual rainfall variability in the tropical Atlantic region. *J. Geophys. Res.*, **111**, doi:10.1029/2005JD005944.

Halpern, D., R. A. Knox, and D. S. Luther, 1988: Observations of 20-day period meridional current oscillations in the upper ocean along the Pacific equator. *J. Phys. Oceanogr.*, **18**, 1514–1534.

Hansen, D. V. and C. A. Paul, 1984: Genesis and effects of long waves in the equatorial Pacific. *J. Geophys. Res.*, **89**, 10431–10440.

Hashizume, H., S.-P. Xie, W. T. Liu, and K. Takeuchi, 2001: Local and remote response to tropical instability waves: A global view from space. *J. Geophys. Res.*, **106**, 10173–10185.

Hayes, S. P., M. J. McPhaden, and J. M. Wallace, 1989: The influence of sea surface temperature on surface wind in the eastern equatorial Pacific: Weekly to monthly variability. *J. Climate*, **2**, 1500–1506.

Hill, K. L., I. S. Robinson, and P. Cipollini, 2000: Propagation characteristics of extratropical planetary waves observed in the ATSR global sea surface temperature record. *J. Geophys. Res.*, **105**, 21927–21946.

Hoffman, R. N. and S. M. Leidner, 2005: An introduction to the near real time QuikSCAT data. *Weather and Forecasting*, **20**, 476–493.

Jochum, M., P. Malanotte-Rizzoll, and A. J. Busalacchl, 2004: Tropical instability waves in the Atlantic Ocean. *Ocean Modelling*, **7**, 145–163.

Johnson, E. S. and J. A. Proehl, 2004: Tropical instability wave variability in the Pacific and its relation to large-scale currents. *J. Phys. Oceanogr.*, **34**, 2121–2147.

Legeckis, R., 1977: Long waves in the eastern equatorial Pacific Ocean: A view from a geostationary satellite. *Science*, **197**, 1179–1181.

Lindzen, R. S. and S. Nigam, 1987: On the role of sea surface temperature gradients in forcing low-level winds in the Tropics. *J. Atmos. Sci.*, **44**, 2418–2436.

Liu, W. T., X. Xie, P. S. Polito, S.-P. Xie, and H. Hashizume, 2000: Atmospheric manifestation of tropical instability waves observed by QuikSCAT and Tropical Rain Measuring Mission. *Geophys. Res. Lett.*, **27**, 2545–2548.

Lukas, R., 1987: Horizontal Renolds stress in the central equatorial Pacific. *J. Geophys. Res.*, **92**, 9453–9463.

Luther, D. S. and E. S. Johnson, 1990: Eddy energetics in the upper equatorial Pacific during the Hawaii-to-Tahiti Shuttle Experiment. *J. Phys. Oceanogr.*, **20**, 913–944.

Masina, S. and S. G. H. Philander, 1999: An analysis of tropical instability waves in a numerical model of the Pacific Ocean -1. Spatial variability of the waves. *J. Geophys. Res.*, **104**, 29613–29635.

Masina, S., S. G. H. Philander, and A. B. G. Bush, 1999: An analysis of tropical instability waves in a numerical model of Pacific Ocean -2. Generation and energetics of the waves. *J. Geophys. Res.*, **104**, 29637–29661.

Menkes, C. E., S. C. Kennan, P. Flamant, Y. Dandonneau, S. Masson, B. Blessy, E. Marchal, G. Eldin, J. Grelet, Y. Montel, A. Morliere, A. Lebourges-Dhaussy, C. Moulin,

G. Champalbert, and A. Herbland, 2002: A whirling ecosystem in the equatorial Atlantic. *Geophys. Res. Lett.*, **29**.

Mitchell, T. P. and J. M. Wallace, 1992: On the annual cycle in equatorial convection and sea surface temperature. *J. Climate*, **5**, 1140–1152.

Mlawer, E., S. J. Taubman, P. D. Brown, M. J. Iacono, and S. A. Clough, 1997: Radiative transfer for inhomogeneous atmosphere: RRTM, a validated correlated-k model for longwave. *J. Geophys. Res.*, **102**, 1663–16682.

Pezzi, L. P. and K. J. Richards, 2004: Influence of ocean-atmosphere coupling on the properties of Tropical Instability Waves. *Geophys. Res. Lett.*, **31**.

Philander, S. G. H., 1976: Instabilities of zonal equatorial currents -part 1. *J. Geophys. Res.*, **81**, 3725–3735.

— 1978: Instabilities of zonal equatorial currents -part 2. *J. Geophys. Res.*, **83**, 3679–3682.

Philander, S. G. H. and R. C. Pacanowski, 1986: A model of the seasonal cycle in the tropical Atlantic Ocean. *J. Geophys. Res.*, **91**, 14192–14206.

Proehl, J., 1996: Linear instability of equatorial zonal flows. *J. Phys. Oceanogr.*, **26**, 601–621.

Qiao, L. and R. H. Weisberg, 1995: Tropical instability wave kinematics: Observations from the tropical instability wave experiment. *J. Geophys. Res.*, **100**, 8677–8693.

Reynolds, R. W., 1988: A real-time global sea surface temperature analysis. *J. Climate*, **1**, 75–86.

Reynolds, R. W. and T. W. Smith, 1994: Improved global sea surface temperature analyses using optimum interpolation. *J. Climate*, **7**, 929–948.

Saravanan, R. and P. Chang, 2000: Interaction between tropical Atlantic variability and El Niño-Southern Oscillation. *J. Climate*, **13**, 2177–2194.

Small, R. J., S.-P. Xie, and Y. Wang, 2003: Numerical simulation of atmospheric response to Pacific tropical instability waves. *J. Climate*, **22**, 3723–3741.

Vizy, E. K. and K. H. Cook, 2002 (D3): Development and application of a mesoscale climate model for the Tropics: Influence of sea surface temprature anomalies on the West African monsoon. *J. Geophys. Res.*, **107**, doi:10.1029/2001JD000686, 2002.

Wallace, J. M., T. P. Mitchell, and C. Deser, 1989: The influence of sea surface temperature on surface wind in the eastern equatorial Pacific: Seasonal and interannual variability. *J. Climate*, **2**, 1492–1499.

Wang, W. M. and M. J. McPhaden, 1999: The surface-layer heat balance in the equatorial Pacific Ocean. Part i: Mean seasonal cycle. *J. Phys. Oceanogr.*, **29**, 1812–1831.

Weisberg, R. and T. Weingartner, 1988: Instability waves in the equatorial Atlantic Ocean. *J. Phys. Oceanogr.*, **18**, 1641–1657.

Wentz, F. J., C. Gentemann, D. Smith, and D. Chelton, 2000: Satellite measurements of sea surface temperature through clouds. *Science*, **288**, 847–850.

Xie, S.-P., M. Ishiwatari, H. Hashizume, and K. Takeuchi, 1998: Coupled ocean-atmospheric waves on the equatorial front. *Geophys. Res. Lett.*, **25**, 3863–3866.

Zang, D. L. and R. A. Anthes, 1982: A high resolution model of the planetary boundary layer sensitivity tests and comparisons with SESAME-79 data. *J. Appl. Meteor.*, **21**, 1594–1609.

Zebiak, S. E., 1993: Air-sea interaction in the equatorial Atlantic region. *J. Climate*, **6**, 1567–1586.

Zhang, G. and M. J. McPhaden, 1995: The relationship between sea surface temperature and latent heat flux in the equatorial Pacific. *J. Climate*, **8**, 589–605.

VITA

Qiaoyan Wu graduated from Nanjing University with a Bachelor of Science in Atmospheric Sciences in July 2001. From September 2001 to July 2002 she was a member of Key Laboratory for Mesoscale Severe Weather in Nanjing University. In August 2002 she came to Texas A&M University as a graduate student and received Master's degree in Atmospheric Sciences in August 2004. She also received a PhD in Atmospheric Sciences at Texas A&M University in August 2007. She may be reached at Department of Atmospheric Sciences, Texas A&M University, 77843.